

## Chapter 3

# Hydrodynamic methods and sub-resolution models for cosmological simulations

Milena Valentini<sup>\*,†,△</sup> and Klaus Dolag<sup>§,‡,¶</sup>

*\*Dipartimento di Fisica, Università degli Studi di Trieste  
Via Alfonso Valerio 2, 34127 Trieste, Italy*

*†INAF - Astronomical Observatory of Trieste  
via Tiepolo 11, I-34131 Trieste, Italy*

*§Universitäts-Sternwarte München, LMU  
Scheinerstr. 1 D-81679 München, Germany*

*‡MPI for Astrophysics*

*Karl-Schwarzschild Strasse 1 D-85748 Garching, Germany*

*△milena.valentini@units.it*

*¶dolag@usm.uni-muenchen.de*

Cosmological simulations are powerful tools in the context of structure formation. They allow us to explore the hierarchical assembly of dark matter (DM) halos and their clustering, to validate or reject possible scenarios of structure formation, and to investigate the physical properties of evolving galaxies across cosmic time. Cosmological hydrodynamical simulations are especially key to study how the complex interstellar medium (ISM) of forming galaxies responds to the most energetic processes during galaxy evolution, such as stellar feedback ensuing supernova (SN) explosions and feedback from AGN (active galactic nuclei). Given the huge dynamical range of physical scales spanned by the astrophysical processes involved in cosmic structure formation and evolution, cosmological simulations resort to sub-resolution models to capture processes occurring below their resolution limit. The impact of different sub-grid prescriptions accounting for the same process is striking, though often overlooked. Some among the main aforementioned processes include: hot gas cooling, star formation and stellar feedback, stellar evolution and chemical enrichment, black hole (BH) growth and their ensuing feedback. Producing simulations of cosmic structure formation and galaxy evolution in large computational volumes is key to shed new light on what drives the formation of the first structures in the Universe, and their subsequent evolution. Not only are predictions from simulations crucial to compare with data from

ongoing and upcoming observational instruments, but they can also effectively guide future observational campaigns. Besides, since we have entered the era of high-performance computing, it is of paramount importance to have numerical codes which are not only as complete as possible as for the inclusion of physical processes implemented, but also very efficient from the computational point of view and able to smoothly scale on state-of-the-art exascale infrastructures. In this chapter, we review the main hydrodynamic methods used in cosmological simulations and the most common techniques adopted to include the fundamental astrophysical processes which drive galaxy formation and evolution.

### 3.1. Cosmological hydrodynamical simulations

Being gravity the force that drives structure formation, the building block of the majority of cosmological simulations is an  $N$ -body code (see e.g. [1] for a discussion on alternative approaches). The goal of an  $N$ -body code is to investigate the non-linear dynamical evolution of a self-gravitating, collisionless system (see [2, 3], for reviews).

A collisionless fluid is a system whose constituent elements move under the effect of the collective gravity field generated by the total mass distribution: in a collisionless system, gravitational collisions and interactions between fluid elements are negligible and do not influence the motion and general properties of the constituent elements themselves. In order to establish quantitatively whether a system can be considered collisionless or not, the relaxation timescale has to be contrasted to the timescale over which the system evolves. A system featuring  $N$  elements moving with typical velocity  $v$  across its size  $L$  is characterised by the crossing time  $t_{\text{cross}} = L/v$  [4]. Possible collisions with nearby particles result in a quadratic velocity perturbation  $(\Delta v)^2$  of each particle's velocity, since each encounter contributes with a randomly oriented  $\Delta v$ . The relaxation time is the timescale over which the quadratic velocity perturbation amounts to roughly the squared velocity itself  $t_{\text{relax}} = v^2/(\Delta v)^2 \times t_{\text{cross}}$ . Here,  $v^2/(\Delta v)^2$  quantifies the number of crossings required to have a velocity change of the same order as  $v^2$  and depends on the number  $N$  of particles [4]. Therefore, the relaxation time can be cast as  $t_{\text{relax}} = N/(8 \ln N) \times t_{\text{cross}}$ . A system can be deemed as collisionless if its relaxation time exceeds by far the age of the Universe  $\sim 1/H_0$  ( $H_0$  being the present-day value of the Hubble constant). After the timescale  $t_{\text{relax}}$ , deflections in a particle motion by interactions with other particles are expected, and the system cannot be considered collisionless anymore. DM and stars in galaxies can be represented as a collisionless, non-relativistic fluid made of particles, while gas is a collisional component.

To a first approximation, the formation of cosmic structures can be studied using  $N$ -body simulations, which only follow the evolution of collisionless particles under gravity. Such simulations have been performed with high resolution for individual objects, like galaxies and galaxy clusters, as well as for very large-scale structures. The numerical methods and different possible approaches used to tackle the problem

of integrating the equations of motion of the  $N$  particles in the cumulative gravity field are described in Chapter 2.

However, with the possible exception of gravitational lensing, observations mainly reflect the state of the ordinary (baryonic) matter. Therefore, their interpretation in the framework of cosmic structure evolution requires that we understand the complex, non-gravitational physical processes which determine the evolution of the cosmic baryons. How DM, gas and stars co-evolve – with baryons falling into the potential well of the underlying DM distribution, cooling, and finally condensing to form stars (see Video 1, page xiii) – within the hierarchical formation scenario contributes to the state and composition of the intergalactic and intracluster media (IGM and ICM, respectively), and is responsible for feedback in energy and metals, magnetic fields, and high-energy particles. Depending on their origin, these components will be blown out by jets, winds or ram pressure effects and finally mix with the surrounding IGM/ICM. While some of these effects will be naturally followed within hydrodynamic simulations (like ram pressure effects), others have to be included in simulations via effective models (like star formation and ensuing feedback, and chemical pollution of the ISM, IGM and ICM by SNe).

Thanks to the improved computing power and advancements in numerical methods, the number of resolution elements<sup>1</sup> which can be used in such simulations has increased dramatically over the last decades, as shown in Fig. 3.1. Note that the largest, hydrodynamical simulations up to date (e.g. *Magneticum*<sup>2</sup> *Box0/mr* [5] and *FLAMINGO*<sup>3</sup> *L2p8-m9* [6]) followed a total number of more than  $2 \times 10^{11}$  particles (e.g., DM, gas, stars and BH particles) across the entire evolution of the Universe.

In this chapter, we will review the basic numerical methods which are used to describe the hydrodynamics, and discuss the main approaches adopted to incorporate the fundamental astrophysical processes in the context of cosmological hydrodynamical simulations (see Video 3, page xiii). Further components like magnetic fields and high-energy particles need additional modelling of their injection processes and evolution. Therefore, they must be self-consistently coupled with hydrodynamics and are described in more detail in Chapter 9.

### 3.2. Hydrodynamics and numerical methods

As a result of the high non-linearity of the gravitational clustering in the Universe, numerical simulations are the only method to follow the evolution of the forming structures like galaxies and galaxy clusters in detail. However, a huge dynamic range in space and time has to be captured. For instance, the range of physical

<sup>1</sup>To be consistent among different simulation techniques, we define resolution elements here as the number of DM particles only, instead of the total number of particles or cells, which would be typically larger by at least a factor 2.

<sup>2</sup>[www.magneticum.org](http://www.magneticum.org)

<sup>3</sup><https://flamingo.strw.leidenuniv.nl/>

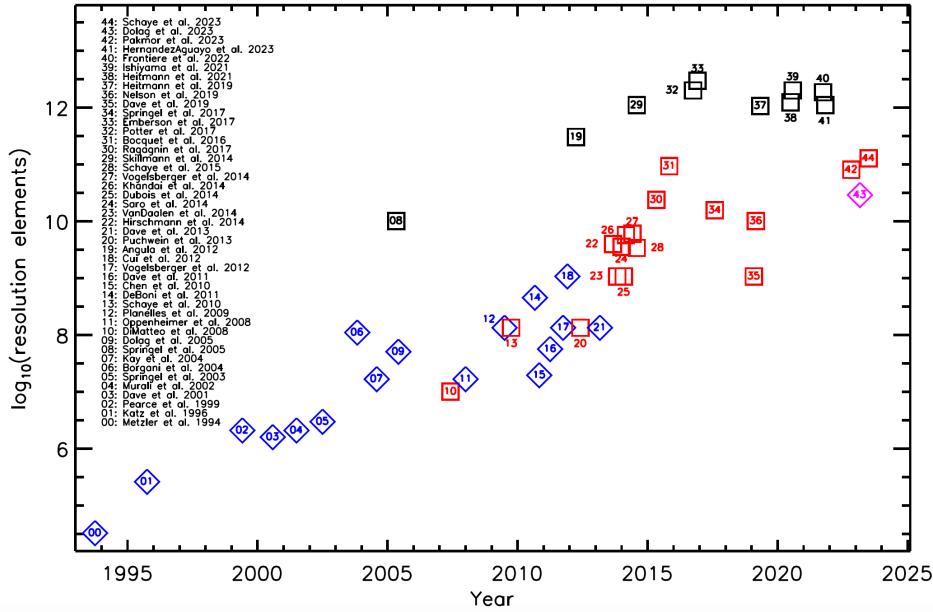


Fig. 3.1. The evolution of the number of resolution elements in simulations. The black line is a fit to the scaling for pure N-body simulations between 1970 and 2005, taken from [7]. The black symbols are recent N-body simulations [8–15]. The colored symbols pinpoint hydrodynamical, cosmological simulations over the last three decades. Blue data points depict simulations including the effect of cooling and star formation [16–31], while red data points show simulations which also feature the effect of AGN feedback [5, 6, 32–45]. The pink symbol marks a simulation which in addition includes the treatment of magnetic field and spectral cosmic ray electrons and protons [46].

scales over which the hierarchical assembly of structures develops spans from sub-kpc scales in galaxies up to several hundreds of megaparsecs, the latter being the largest coherent scale in the Universe. Here, modern cosmological simulation codes based on  $N$ -body and hydrodynamics techniques are best suited to accurately follow the joint dynamics of DM and gas in their full complexity, during the hierarchical build-up of these structures.

### 3.3. Basic equations and techniques

A variety of numerical schemes has been developed in the past decades to solve the coupled system of equations describing the baryonic content of the Universe and the collisionless DM. The majority of the baryons (i.e. gas) can be described as an ideal fluid, whose evolution is ruled by a set of equations, namely, the *Euler equations*. The hydro solvers which integrate the aforementioned equations fall into two main categories, that are summarized in Fig. 3.2: particle methods, which discretize mass (see [47] and references therein), and grid-based methods, which discretize the

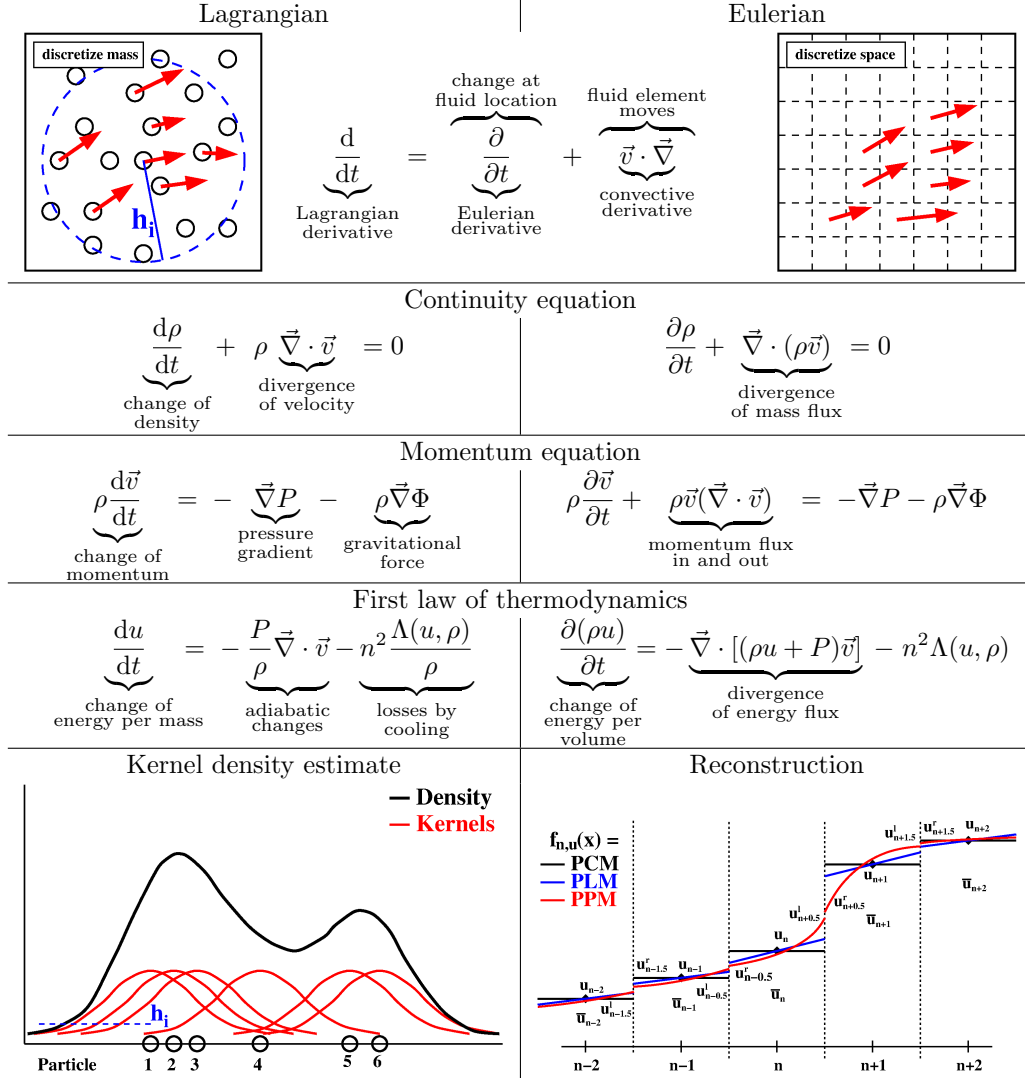


Fig. 3.2. Comparison of the concept of Lagrangian and Eulerian formulation of hydrodynamics and the resulting set of equations.

computational domain (see [48] and references therein). Recently, additional solvers have been developed: they combine characteristics of both methods (see [49] and references therein) and will be discussed in detail in the following sections.

All of them have to be closed by an *equation of state*, relating the gas pressure  $P$  to the internal energy (per unit mass)  $u$  and the density  $\rho$ . Assuming an ideal, monoatomic gas, this will be  $P = (\gamma - 1)\rho u$  with the polytropic index  $\gamma = 5/3$ .

When applying these equations to the problem of cosmological structure formation, there are several features emerging in comparison to purely hydrodynamic

simulations in a non-expanding background. First, the otherwise often neglected self-gravity, emerging as the  $\vec{\nabla}\Phi$  term, has to be accounted for (its contribution can be solved following the methods described in Chapter 2).

Second, radiative losses, quantified through the cooling function  $\Lambda(u, \rho)$ , where  $n^2 \Lambda$  ( $n^2 \Lambda/\rho$ ) represents the cooling rate per unit volume (mass), with  $n$  being the gas number density, play a key role in influencing the evolution of the baryonic component (see also Section 3.11). Cooling is especially key to describe the history of star formation of the Universe, as outlined in Section 3.14.

Additionally, the equations have to be adapted to the cosmological background (to take into account the expansion history of the Universe). In almost all cases, the latter step is achieved by switching to the so called comoving coordinates and through a transformation of the time variable. This change does not typically alter the general structure of the equations above, except for additional, cosmological, time dependent pre-factors which appear in the equations (we refer the reader to chapter 5 in [50] for a rigorous derivation).

### 3.4. Eulerian (*grid*) methods

Grid-based methods solve the *Euler equations* (see Fig. 3.2) based on structured or unstructured grids, representing the fluid. While *primitive variables* encode the thermodynamic properties of the fluid (e.g.,  $\rho$ ,  $\vec{v}$ , or  $P$ ), *conservative variables* define the conservation laws (e.g.,  $\rho$ ,  $\rho\vec{v}$ , or  $\rho u$ ). Early attempts were made using a central difference scheme, where fluid is only represented by the centered cell values and derivatives are obtained by the finite-difference representation (see, for example, [51]). These methods use artificial viscosity to handle shocks (similar to the smoothed particle hydrodynamics method described in Section 3.6), as they would otherwise break down in regimes where discontinuities appear. Also, by construction, they are only first-order accurate.

Classical approaches use instead reconstruction schemes which, depending on their order, take several neighboring cells (so-called *stencils*) into account to reconstruct the field of any hydrodynamical variable ( $u_n$ ), with increasing order of accuracy at the interfaces of the cells ( $u_{\pm 0.5}^{l/r}$ ). Typical schemes are the *piecewise constant method* (PCM), the *piecewise linear method* (PLM; e.g., [52]), and the *piecewise parabolic method* (PPM; [53]), as illustrated in the lower right part of Fig. 3.2. The shape of the reconstruction function is then used to calculate the total integral of a quantity over the grid cell, divided by the volume of each cell (e.g., *cell average*,  $\bar{u}_n$ ), rather than pointwise approximations at the grid centers (e.g., *central variables*,  $u_n$ ).

Modern, high-order schemes usually have *stencils* based on at least five grid points and implement *essentially nonoscillatory* (ENO; [54]) or the so-called *weighted essentially nonoscillatory* (WENO; [55]) schemes for reconstruction, which maintain high-order accuracy (see e.g., [56] for a recent review).

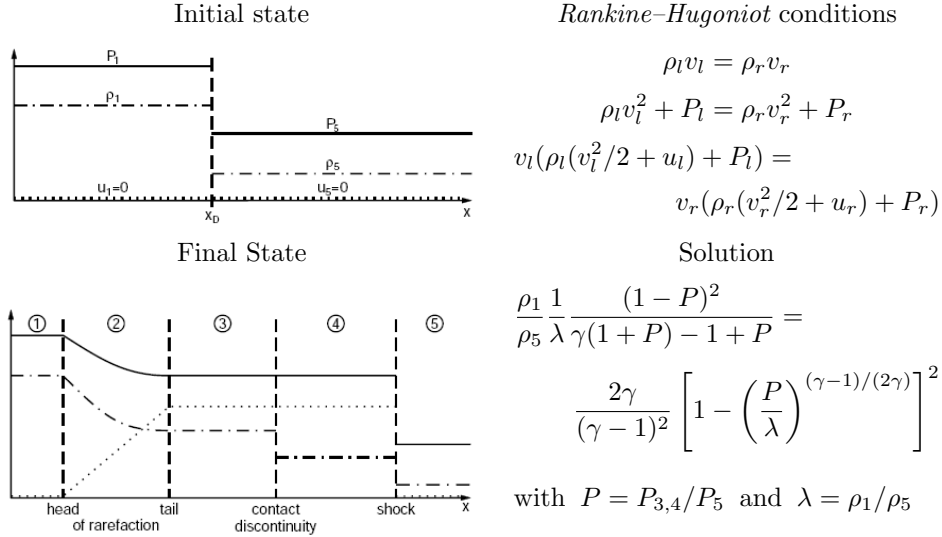


Fig. 3.3. The initial (upper left panel) and final (lower left panel) state of the so-called *Riemann* problem, for the case of no relative motion between the two sides ( $u_1 = u_5 = 0$ ). The solid lines mark the pressure  $P$ , the dashed-dotted lines the density  $\rho$ , and the dotted line the velocity  $v$ . Kindly provided by Ewald Müller. Right side lists the *Rankine-Hugoniot* conditions and the solution to this simplified *Riemann* problem.

The reconstructed quantities are used to calculate the left- and right-hand side values at the cell boundaries. These values are then exploited as initial conditions to solve the so-called *Riemann* problem (see right panel of Fig. 3.3), whose solution provides the fluxes of various quantities (e.g., mass, energy, etc.) across the cell borders. Additional constraints are included to avoid oscillations (e.g., the development of new extrema) in these reconstructions, such as the so-called slope limiters, which estimate the maximum slope allowed for the reconstruction. One way is to demand that the total variation among the interfaces does not increase with time. These so-called *total variation diminishing* schemes (*TVD*; [57]) nowadays provide various different slope limiters, as suggested by different authors.

How to solve the general *Riemann* problem, i.e. the evolution of a discontinuity initially separating two states, can be found in textbooks (e.g., [58]). Here, we only want to give a brief description of the solution of a shock tube as an example. This corresponds to a system where both sides are initially at rest. The left part of Fig. 3.3 shows in the initial (upper panel) and the evolved (lower panel) system. The latter can be divided into five regions. The values for regions 1 and 5 are identical to the initial configuration. Region 2 is a rarefaction wave which is determined by the states in regions 1 and 3. The solution can be obtained by invoking the general *Rankine-Hugoniot* conditions, describing the jump conditions at a discontinuity. They are listed in the right upper part, where we have assumed a coordinate system which moves with the shock velocity  $v_s$ . By combining such conditions and defining

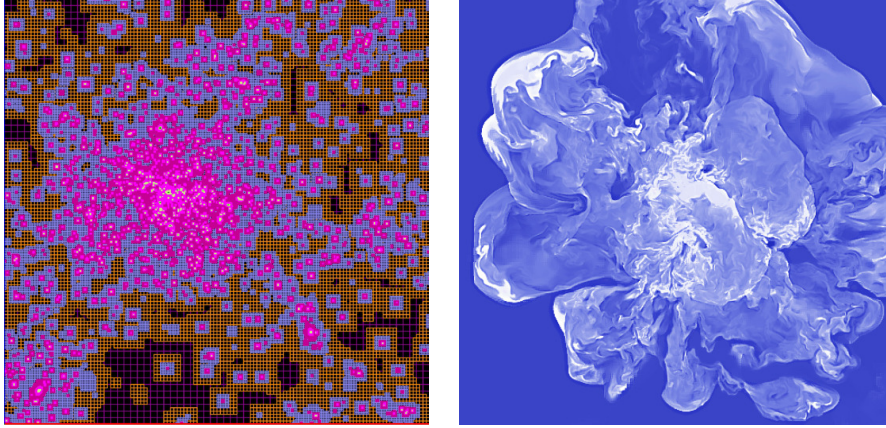


Fig. 3.4. Left panel: Mesh refinement levels of *RAMSES* for a typical, cosmological simulation. Kindly provided by Romain Teyssier. Right panel: Slice in gas temperature through a cluster simulation, with refinement based on velocity jumps. This refinement criterion ensures high resolution around shocks even in the outer parts of the cluster. Figure taken from [75].

the initial density ratio  $\lambda = \rho_1/\rho_5$ , it is possible to get the nonlinear, algebraic equation for the pressure ratio  $P = P_{3,4}/P_5$ , as displayed in the lower right part of Fig. 3.3. Once  $P_{3,4}$  is known by solving this equation, the remaining unknowns can be inferred step by step from the four conditions.

Solving the full *Riemann* problem in a hydrodynamics code can be expensive and it can severely affect the code performance. Therefore, there are various approximate methods to solve the *Riemann* problem, including the so-called *ROE method* (e.g., [59]), the *HLL/HLLE* method (e.g., see [60–62]), and *HLLC* (e.g., see [63]). A description of all these methods is outside the scope of this review, so we refer the reader to the references given or to textbooks (e.g., [64]).

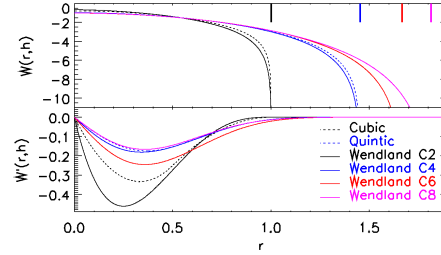
A wide variety of grid codes are used for cosmological applications, including *TVD*-based codes (e.g., [65] and *CosmoMHD* [66]) and *PLM*-based codes (like *ART* [67, 68] and *RAMSES* [69]). *PPM*-based codes include *Zeus* [70], *ENZO* [71], *COSMOS* [72], and *FLASH* [73]. It is worth mentioning the *WENO*-based code by [74].

### 3.5. Adaptive mesh refinement

To widen the dynamical range of the numerical schemes, mesh refinement strategies have been applied in several grid codes (e.g., *ART*, *RAMSES*, *ENZO*, and *FLASH*). In most of the cases, a simple density (e.g., mass per cell) criterion is used. If the mass within one cell exceeds a certain threshold,  $m \equiv \rho \Delta x^3 > m_{\min}$ , the cell is divided in multiple (e.g., eight) sub-cells and the internal properties are interpolated from the original cell onto the new sub-cells. This ensures that the gravitational mass (e.g., the source of gravity) is homogeneously distributed within the computational domain. In this way, the underlying grid evolves in a quasi-Lagrangian fashion

## Kernel density estimate

$$\begin{aligned}\langle X(\vec{x}) \rangle &= \int W(\vec{x} - \vec{x}', h) X(\vec{x}') d\vec{x}' \\ \int W(\vec{x}, h) d\vec{x} &= 1 \text{ and } W(\vec{x}, h) \xrightarrow{h \rightarrow 0} \delta(\vec{x}) \\ \langle X_i \rangle &= \langle X(\vec{x}_i) \rangle = \sum_j \frac{m_j}{\rho_j} X_j W(\vec{r}_{ij}, h) \\ \nabla_i \langle X(\vec{x}_i) \rangle &= \sum_j \frac{m_j}{\rho_j} X_j \nabla_i W(\vec{r}_{ij}, h)\end{aligned}$$



Pairwise symmetric formulation

individual smoothing length

$$W(\vec{r}_{ij}, h_i, h_j) = \begin{cases} \langle W(\vec{r}_{ij}, h_i), W(\vec{r}_{ij}, h_j) \rangle \\ W(\vec{r}_{ij}, \langle h_i, h_j \rangle) \end{cases}$$

$$\frac{4\pi}{3} h_i^3 \rho_i = N m_i$$

$$(\rho \vec{\nabla}) \cdot X = \vec{\nabla}(\rho \cdot X) - \rho \cdot (\vec{\nabla} X)$$

$$\vec{\nabla}_i W(\vec{r}_{ij}, h_i, h_j) = W'_{ij} \frac{\partial h_i}{\partial \rho_i} = W'_{ij} f_i$$

$$\frac{\vec{\nabla} \cdot X}{\rho} = \vec{\nabla} \frac{X}{\rho} + \frac{X}{\rho^2} \vec{\nabla} \cdot \rho$$

$$f_i \equiv \left( 1 + \frac{h_i}{3\rho_i} \frac{\partial \rho_i}{\partial h_i} \right)^{-1}$$

Estimating higher order gradients from expanding  $\vec{v}_j^\beta$  around  $i$ 

$$\sum_j m_j (\vec{v}_j - \vec{v}_i)^\beta \vec{\nabla}_i^\alpha W_{ij} = \partial_\gamma \vec{v}_i^\beta \sum_j m_j (\vec{x}_j - \vec{x}_i)^\gamma \vec{\nabla}_i^\alpha W_{ij}$$

Improved estimate of  $\partial_\gamma \vec{v}_i^\beta \equiv \mathbf{X}_{\gamma\beta}$ matrix inversion  $\mathbf{X} = \mathbf{M}^{-1} \mathbf{Y}$ 

$$\mathbf{M}_{\alpha\gamma} \equiv \sum_j m_j (\vec{x}_j - \vec{x}_i)^\gamma \vec{\nabla}_i^\alpha W_{ij}$$

$$\mathbf{Y}_{\alpha\beta} = \sum_j m_j (\vec{v}_j - \vec{v}_i)^\beta \vec{\nabla}_i^\alpha W_{ij}$$

$$\Rightarrow \vec{\nabla} \cdot \vec{v} = \partial_\alpha \vec{v}^\alpha$$

$$\Rightarrow (\vec{\nabla} \times \vec{v}) = \epsilon_{\alpha\beta\gamma} \partial_\alpha \vec{v}^\beta$$

Fig. 3.5. Upper left part shows the basic formulation of a kernel density estimate ( $\langle X(\vec{x}) \rangle$ , upper left part), including the properties of the kernel  $W(\vec{x}, h)$  (see also upper right panel) and the discretization of the derivatives. The middle part lists various ways for a symmetric formulations (left part) and the changes in modern SPH to account for individual smoothing length  $h_i$  (right part). The lower row shows how higher order gradients are estimated using a Taylor expansion and matrix inversion in very modern SPH formulations.

following the mass flow, as illustrated in the left panel of Fig. 3.4, which shows the typical structure of the refinement grid in a cosmological simulation.

Other refinement strategies based on velocity criteria are often used [75, 76] to study shocks and turbulence in galaxy clusters. By extending the aforementioned criteria to additionally refining on velocity jumps, the formation of turbulence and shocks can be followed with unprecedented high spatial resolution throughout the cosmic structures, as shown in the right part of Fig. 3.4. In order to follow the turbulent cascade with high precision and accuracy, sub-scale turbulence models can additionally be used to initialize the velocities on the refined cells: this prevents the turbulent cascade from being suppressed [77].

### 3.6. Lagrangian methods and Smoothed Particle Hydrodynamics

The classical Lagrangian method is the so-called Smoothed Particle Hydrodynamics method (SPH; [78, 79]), which solves the Lagrangian form of the Euler equations (see Fig. 3.2) and can achieve good spatial resolution in high-density regions.

The basic idea of SPH is to discretize the fluid by mass elements (i.e. particles), rather than by volume elements as in Eulerian methods (see Fig. 3.2). It is evident that the mean interparticle distance in collapsed objects is smaller than in underdense regions. The scheme will thus be adaptive in spatial resolution by keeping the mass resolution fixed. For a comprehensive review with rigorous derivations of the SPH formalism, see [47].

Fig. 3.5 summarizes the main characteristics of SPH. The general definition of a kernel smoothing method is the first step to build continuous fluid quantities for an arbitrary variable  $X$ . Here, the kernel depends on the distance modulus only, and is in addition required to be monotonic and differentiable (see upper part of Fig. 3.5). In the discretized version, we replace the volume element of the integration,  $d\vec{x} = d^3x$ , with the ratio of the mass and density  $m_j/\rho_j$  of the particles. Although this equation holds for any position  $\vec{x}$  in space, we are only interested here in the fluid representation at the original particle positions  $\vec{x}_i$ , which are the only locations where we will need the fluid representation later on. It is important to note that for kernels with compact support (i.e.,  $W(\vec{x}, h) = 0$  for  $|\vec{x}| > h$ ), the summation does not have to be done over all the particles but only over the particles within the sphere of radius  $h$  (see Fig. 3.2), namely, the neighbors around the particle  $i$  under consideration. Originally, the most frequently used kernel is the  $B_2$ -Spline, but modern schemes invoke an entire new family of kernels like the HOCT kernels [80] or the so-called Wendland kernels [81] which show better stability and higher accuracy (see upper right panel of Fig. 3.5 and also recent review by [82] and references therein).

Derivatives can be calculated using the analytically known derivatives of the kernel. Conservation laws are numerically better achieved when pairwise symmetric formulations are used: this can be obtained by exploiting some identities when using derivatives of  $\rho X$  or  $X/\rho$  (see left middle part of Fig. 3.5). To profit from the adaptive nature of the SPH method, the smoothing length  $h_i$  is typically allowed to vary for each individual particle  $i$  and is determined by encompassing either a fixed number of neighbours or a fixed mass within the kernel. However, two complications often stem from the abovementioned individual smoothing lengths: first, a pairwise symmetric formulation needs to define an averaged kernel for each particle pair, and historically various ways to build averages have been discussed. The other is that the derivatives of the kernel – being the smoothing length spatial dependent – come with correction terms ( $\partial h_i/\partial \rho_i$ ), which originally have been always ignored because they can't be computed directly. Starting from an entropy formulation, [83] derived for the first time an SPH formulation including the proper correction terms

for the varying smoothing length from a Lagrangian formalism, which are listed in the middle right part of Fig. 3.5. Note that this formalism then also specifies the way in which the averaged kernel for a particle pair has to be constructed.

This can be further generalized, as shown in [84]. There, such a generalized formulation was obtained starting from an  $x$ -weighted volume average

$$\bar{y} = y_i = \sum_j x_j W_{ij}(h_i), \quad (3.1)$$

the ( $x$ -weighted) volume element  $\Delta\nu_i \equiv x_i/y_i$  and the generalized relation

$$P_i = (\gamma - 1)u_i \frac{m_i}{\Delta\nu_i} = A_i \left( \frac{m_i}{\Delta\nu_i} \right)^\gamma \quad (3.2)$$

between the pressure  $P_i$ , the internal energy per unit mass  $u_i$  and the entropic function  $A_i$ . This leads to the set of generalized SPH equations

$$m_i \frac{d\vec{v}_i}{dt} = - \sum_j x_i x_j \left( f_{ij} \frac{P_j}{y_j^2} \vec{\nabla}_i W_{ij}(h_i) + f_{ji} \frac{P_i}{y_i^2} \vec{\nabla}_i W_{ij}(h_j) \right), \quad (3.3)$$

and

$$f_{ij} \equiv 1 - \frac{\tilde{x}_i}{x_j} \left( \frac{h_i}{3\tilde{y}_i} \frac{\partial y_i}{\partial h_i} \right) \left[ 1 + \frac{h_i}{3\tilde{y}_i} \frac{\partial \tilde{y}_i}{\partial h_i} \right]^{-1}. \quad (3.4)$$

For the choice of  $x_i = \tilde{x}_i = m_i$ , which implies  $y_i = \tilde{y}_i = \bar{\rho}_i$  and  $\Delta\nu_i = m_i/\rho_i$ , and following the entropy  $A_i$  (e.g.,  $P_i = A_i \bar{\rho}_i^\gamma$ ), this set of equations will result in the entropy-conserving formulation of SPH as presented in [83]. For the choice of  $x_i = \tilde{x}_i = (\gamma - 1)m_i u_i$ , implying  $y_i = \bar{P}_i$  and  $\Delta\nu_i = (\gamma - 1)m_i u_i/P_i$ , this results in a pressure–energy formulation of SPH, as presented in [85]. As now pressure is a kernel weighted quantity, contact discontinuities are properly treated. A third possibility is to choose  $x_i = m_i A_i^{1/\gamma}$  which leads to a pressure–entropy formulation. For more details, see [84].

The SPH method, however, is not performing as well in low-density regions as in the higher density ones. It also suffers from degraded resolution in shocked regions due to the introduction of a sizeable artificial viscosity. In its classical implementation, discretization errors introduce spurious pressure forces on particles in regions with steep density gradients in particular near contact discontinuities. This results in a boundary gap of the size of an SPH smoothing kernel radius over which interactions are severely damped. The standard implementation typically does not involve an explicit mixing term, which can compensate this effect. Therefore, the classical implementation does not resolve and treat dynamical instabilities in the interaction of multi-phase fluids, such as *Kelvin–Helmholtz* or *Rayleigh–Taylor* instabilities. Both these shortcomings can be overcome by a modern implementation as described at the end of this section. In addition, in the cosmological context, the adaptive nature of the SPH method, its simple way to couple to gravity and the

possibility to have individual time steps often compensate for such shortcomings, thus making SPH still one of the most commonly used methods in numerical hydrodynamical cosmology.

As mentioned before, we also need to add a so-called *artificial viscosity*,  $\Pi_{ij}$ , so that the final equations for the entropy-conserving formulation of SPH are reading

$$\frac{d\vec{v}_i}{dt} = - \sum_j m_j \left( f_j \frac{P_j}{\rho_j^2} \vec{\nabla}_i W_{ij}(h_j) + f_i \frac{P_i}{\rho_i^2} \vec{\nabla}_i W_{ij}(h_i) + \Pi_{ij} \vec{\nabla}_i \bar{W}_{ij} \right), \quad (3.5)$$

and

$$\frac{dA_i}{dt} = \frac{1}{2} \frac{\gamma - 1}{\rho_i^{\gamma-1}} \sum_j m_j \Pi_{ij} (\vec{v}_j - \vec{v}_i) \cdot \vec{\nabla}_i \bar{W}_{ij}. \quad (3.6)$$

This term describing an *artificial viscosity* is usually needed to capture shocks and its construction is similar to other hydrodynamical schemes. Popular formulations are those proposed by Monaghan and Gingold [86] and Balsara [87], which includes a bulk viscosity and a *von Neumann–Richtmeyer* viscosity term, supplemented by a limiter reducing angular momentum transport in the presence of shear flows at low particle numbers [88]. Modern schemes implement a form of the artificial viscosity as proposed by [89], based on an analogy with *Riemann* solutions of compressible gas dynamics. To reduce this artificial viscosity, at least in those parts of the flows where there are no shocks, a possibility is to follow the idea proposed by Morris and Monaghan [90]: every particle carries its own artificial viscosity, which eventually decays outside the regions which undergo shocks. A detailed study of the implications on the ICM of such an implementation can be found in [91]. There are various further improvements on the implementation a higher order artificial dissipation term [92, 93]. Modern SPH formulations also make use of higher order calculation schemes for velocity gradients, see lower part of Fig. 3.5 as well as related discussion in [94, 95]. Even better suppression of the artificial viscosity can be reached by following [92] in combination with such higher order calculation schemes for velocity gradients, as shown in [96].

Considerable effort has been made in the last decade to combine the advantages of Lagrangian and Eulerian methods. On one hand, significant progress has been achieved in involving Godunov methods into the SPH formalism, see [97–100], which recently led to the so called meshless methods. On the other hand, large effort has been made to extend Eulerian methods to moving mesh methods. Both these new methods are briefly described in the next two sub-sections.

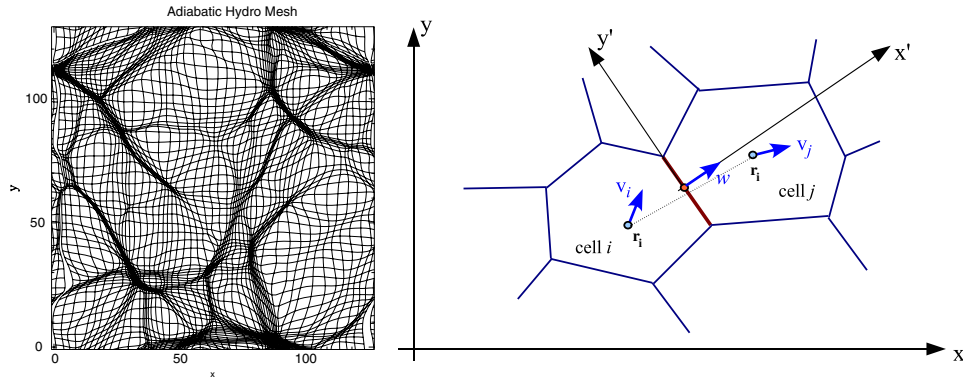


Fig. 3.6. Left panel: A layer through a cosmological,  $128^3$  moving mesh simulation. Figure taken from [101]. Right panel: Illustrating the concept of flux computation on a Voronoi mesh. Figure taken (and slightly adapted) from [103].

### 3.7. Moving mesh methods

Substantial effort has gone into reformulating Eulerian methods as described in Section 3.4 into Lagrangian mesh approaches. More details on the idea of hydrodynamics on moving mesh for cosmological application can be found in the pioneering work by [101] and references therein. This early approach started from a regular mesh which then, by following the flow of the fluid, was deformed. The Euler equations were evolved by calculating the fluxes across the cell borders. An example of the resulting mesh for a cosmological simulation can be seen in the left part of Fig. 3.6. One disadvantage (or challenge) of this technique in practical applications is that individual cells can be extensively deformed and stretched. Modern schemes circumvent this problem by constructing an unstructured mesh based on a Voronoi or Delaunay tessellation (see [102] and references therein). The relevant geometry of the cells, based on the mesh generating points  $\vec{r}_i$  and  $\vec{r}_j$  is illustrated in the right part of Fig. 3.6. The fluxes then have to be calculated at the centroid of the interface (note that this is not necessarily on the straight line between the two mesh generating points, as indicated by the dotted line)

$$\mathbf{Q}_i^{(n+1)} = \mathbf{Q}_i^{(n)} - \Delta t \sum_j A_{ij} \hat{\mathbf{F}}_{ij}^{(n+1/2)}. \quad (3.7)$$

The motion  $\vec{w}$  of this interface is uniquely defined by the velocities  $\vec{w}_i$  and  $\vec{w}_j$ , and the fluxes have to be calculated with the Riemann solver in the rotated frame  $(x', y')$ . A detailed description of this technique along with its performance in test problems can be found in [102].

### 3.8. Meshless methods

A new class of Lagrangian methods, the so-called meshless formulations, have been recently developed for astrophysical problems. More details can be found in [102, 104, 105], which follow earlier, pioneering work by [106–108]. In short, the derivation starts from the integral form

$$\int [u(\vec{x}, t)\dot{\phi}(\vec{x}, t) + \vec{F}(u, \vec{x}, t) \cdot \nabla\phi(\vec{x}, t) + S(\vec{x}, t)\phi(\vec{x}, t)] d\vec{x} dt = 0 \quad (3.8)$$

of a scalar conservation law

$$\frac{\partial u}{\partial t} + \nabla \cdot (\vec{F} + \vec{a}u) = S. \quad (3.9)$$

Here,  $u(\vec{x}, t)$  is a scalar field,  $S(\vec{x}, t)$  is its source,  $\vec{F}(u, \vec{x}, t)$  is its flux in a frame moving with velocity  $\vec{a}(\vec{x}, t)$ , and  $\phi(\vec{x}, t)$  is an arbitrary differentiable function in space and time leading to the advective derivative  $\dot{\phi}(\vec{x}, t) = \partial\phi(\vec{x}, t)/\partial t + \vec{a}(\vec{x}, t) \cdot \nabla\phi(\vec{x}, t)$ .

Using a discretization through a set of particles  $i$  with a smoothing length  $h(\vec{x})$  and a kernel function  $W(\vec{x}, h)$ , akin to what is done in SPH, the partitioning of the particles can be written as

$$\psi_i(\vec{x}) = w(\vec{x})W(\vec{x} - \vec{x}_i, h(\vec{x})), \quad (3.10)$$

where the number density of particles is  $w(\vec{x})^{-1} = \sum_j W(\vec{x} - \vec{x}_j, h(\vec{x}))$ . The discretization of an arbitrary function  $f(\vec{x})$  can be written as

$$\int f(\vec{x}) d\vec{x} \approx \sum_i f_i \int \psi_i(\vec{x}) d\vec{x} \equiv \sum_i f_i V_i, \quad (3.11)$$

where  $V_i = \int \psi_i(\vec{x}) d\vec{x}$  is the effective volume of a particle  $i$ . Therefore, the discrete form of the integral equation (3.28) can be written as

$$\sum_i \int [V_i u_i \dot{\phi}_i + V_i F_i^\alpha (D^\alpha \phi)_i + V_i S_i \phi_i] = 0. \quad (3.12)$$

Although in principle an SPH estimate for  $(D^\alpha \phi)_i$  could be used, it is convenient to use a more accurate meshless gradient estimate, as suggested by [107]. This, along with the integration of the first term by parts, makes it possible (as shown in [102]) to split  $\phi(\vec{x}, t)$  and to obtain:

$$\frac{d}{dt}(V_i u_i) + \sum_j [V_i F_i^\alpha \psi_j^\alpha(\vec{x}_i) - V_j F_j^\alpha \psi_i^\alpha(\vec{x}_j)] = V_i S_i. \quad (3.13)$$

This equation (and its extension to a general vector field  $\vec{u}$ ) is very similar to the finite volume equation for the moving mesh method<sup>4</sup> but also somewhat similar

<sup>4</sup>Note that, however, Eq. (3.7) is in the integral form.

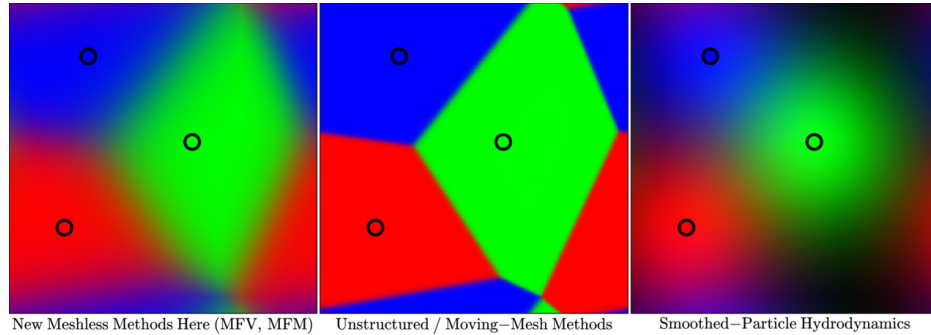


Fig. 3.7. Illustrating the conceptual differences in partitioning the volumes between meshless methods, unstructured grid and classical kernel weighted formalism, as used in SPH methods. Figure taken from [104].

to the SPH equations, except that the interactions between different particles is described in the source and flux terms, which can be obtained as the solution of an approximate Riemann problem between particles  $i$  and  $j$ . A closer inspection also reveals that only the projection on the direction between the particles is needed, e.g., the solution of the Riemann problem at the midpoint<sup>5</sup>. This also means that the primitive variables have to be extrapolated to the midpoint, e.g., using linear extrapolation, and generally a flux limiter has to be applied (see discussion in [102, 104, 105]). Figure 3.7 illustrates the differences in partitioning the volumes between mesh-less methods, unstructured (moving) grid and classical kernel weighted formalism (SPH).

### 3.9. Code comparison in galaxy and cluster simulations

The Eulerian and Lagrangian approaches described in the previous sections are theoretically supposed to provide the same results when applied to the same problem. To verify that codes succeed at correctly integrating the set of hydrodynamical equations, they are usually tested against problems whose solution is known analytically. In practice, these test problems are shock tubes or spherical collapse problems.

However, idealized hydrodynamical tests like the interaction of multi-phase fluids [109] often reveal fundamental differences among results obtained with different methods. Such differences can be driven by the formulation of the underlying fundamental equations (like no mixing in classical SPH), by the discretization (like the volume bias in SPH formulations) or they can be due to the influence of numerical errors (like the departure of translation invariance in grid codes due to errors in the reconstruction).

<sup>5</sup>More accurate would be the quadrature point at an equal fraction of the kernel length  $h_i$  and  $h_j$ , see discussion in [104] and references therein.

In cosmology, problems with known analytical solutions are impractical: as a consequence, a meaningful test is represented by comparing the results provided by different codes when they simulate the formation of cosmic structures in a standard set-up. As an example, [110] compares the thermodynamical properties of the IGM predicted by the *GADGET* (SPH-based) and *ENZO* (grid-based) codes. Another example of a comparison between grid-based and SPH-based codes can be found in [111].

A detailed comparison of hydrodynamical codes which simulate the formation and evolution of a galaxy or of a galaxy cluster is therefore an extremely important test. A pioneering comparison was performed within the so-called Santa Barbara Cluster Comparison Project [112]. Here, 12 different groups, each using a code either based on the SPH technique (seven groups) or on the grid technique (five groups), performed a non-radiative simulation of a galaxy cluster from the same initial conditions.

A more recent comparison project, the so-called nIFTy galaxy cluster simulations [113], also involved modern SPH implementations as well as the moving mesh code *AREPO*. A similar agreement over large ranges was obtained for many of the gas properties in both studies, like the density, temperature and entropy profiles, as shown in Fig. 3.8. Both studies found significantly larger differences between mesh-based codes and classical particle-based codes to be present for the inner part of the profiles. However, as shown in [113], particle-based codes which include an explicit treatment of mixing produce results very similar to grid-based codes.

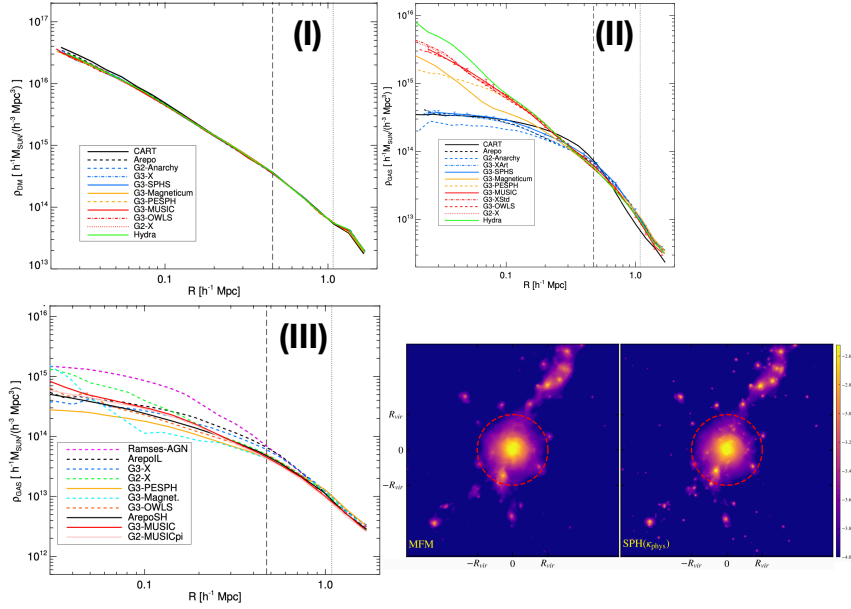
A few code comparison campaigns have targeted galaxies as well (see e.g., [114, 115], Fig. 3.8, and Section 3.14).

It is worth mentioning that as soon as additional physics like star formation and AGN feedback is included, the discrepancies in the results obtained by the various numerical methods are no longer driven by differences which can be ascribed to the hydrodynamical solvers: they are rather due to the details of the numerical prescriptions adopted to model these additional processes [116].

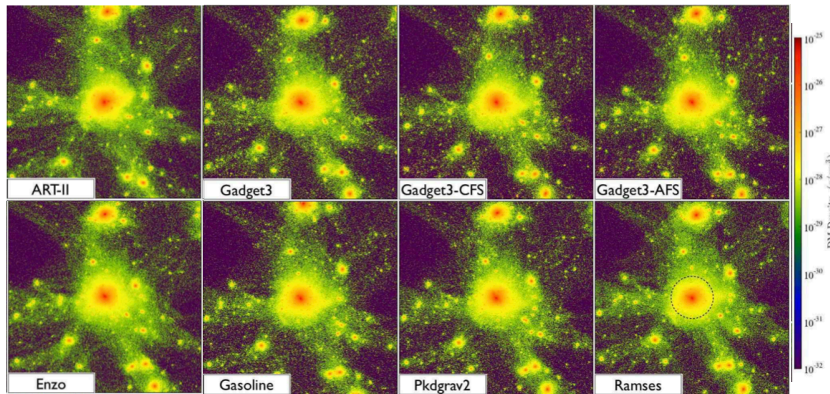
### 3.10. Sub-resolution modelling of astrophysical processes

The astrophysical processes involved in the formation and evolution of galaxies in cosmological hydrodynamical simulations span a huge dynamical range of scales. They indeed vary from the  $\sim$ Mpc scales where gravitational instabilities drive the evolution of the DM component and the hierarchical assembly of haloes, down to the  $\sim$ parsec and  $\sim$ sub-parsec scales, where processes like BH accretion and star formation take place, going through the  $\sim$ kpc scales, where e.g. galactic winds distribute the stellar feedback energy to the ambient medium. The call for sub-grid physics is thus essential: sub-resolution models account for processes that occur below the resolution limit of cosmological hydrodynamical simulations, but that affect the evolution of the simulated structure on scales that are explicitly resolved.

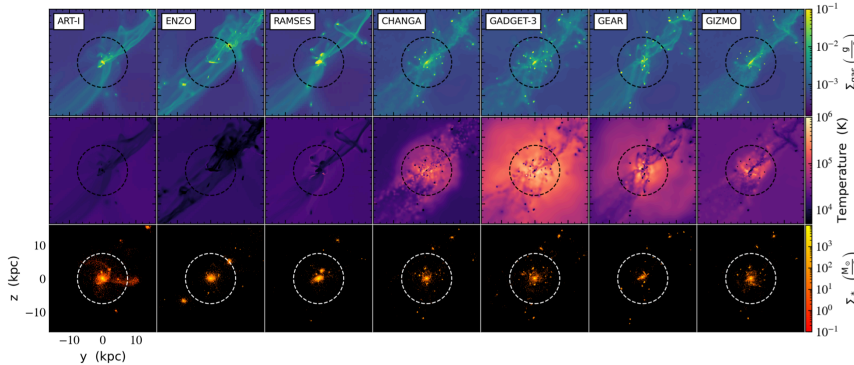
Hydrodynamic methods and sub-resolution models for cosmological simulations



a) - nIFTY cluster: DM only (I), non radiative (II), and radiative+full physics (III) simulations; same nIFTY cluster simulated with different hydrodynamic solvers.



b) - DM-only cosmological simulations of a Milky Way halo, at z=0.



c) - Cosmological hydrodynamic simulations including cooling and star formation of a disc galaxy at z=4.

Fig. 3.8. Selection of figures from code comparison campaigns that aimed at quantifying the impact of using different codes on final results. *Panel a*: Impact of different codes on the density radial profiles of a galaxy cluster, when different simulation setups are considered. We show DM-only simulations (*i*), non-radiative runs (*ii*), and radiative plus full physics simulations (*iii*) (Figures 2 and 6 from [113], and Figure 8 from [116]). The fourth composite panel shows the same nIFTY cluster simulated with two different hydro solvers (namely, MFM on the left and SPH on the right) by [105]. *Panel b*: DM-only cosmological simulations of a Milky Way halo, at z=0 (adapted from Figure 3 in [117]). *Panel c*: Cosmological hydrodynamical simulations featuring cooling and star formation, and targeting a Milky-Way like galaxy, at z=4 (Figure 11 from [115]).

Sub-resolution prescriptions usually resort to rather simple analytical or theoretical models, and/or to the phenomenological description of rather complex processes, through a suitable choice of parameters that are calibrated to reproduce observations (see also sub-section 3.16).

A common criticism that has been often raised to numerical astrophysics deals with the number of parameters that are employed when modelling physical processes, in particular when referring to the parameters that enter sub-resolution models. However, observed or expected results cannot be reproduced by just fine-tuning parameters. Results are rather determined by proper parametrizations of processes. For instance: when modelling star formation (see sub-section 3.12), results are mainly driven by the way in which the star formation rate (SFR) relates to the actual fuel (e.g. the mass of molecular or cold gas available), rather than to the exact value of the proportionality constant between the two aforementioned quantities. Parameter space exploration is thus not meant to provide the best fit to observations that simulations want to compare with. It rather aims at enabling a better understanding of the dependence of a model on different unknowns and at making predictions for loosely constrained physical quantities.

In the next sub-sections, we will review the most important astrophysical processes that significantly affect galaxy formation and evolution. They are all self-consistently included in state-of-the-art cosmological hydrodynamical simulations.

### 3.11. Gas cooling

Hot gas cooling enters the right-hand side of equation 3.3, as well as the equations describing mass and energy flows among different gas phases which may be present in sub-resolution models.

In cosmological simulations, the focus is usually on structures whose virial temperature exceeds  $\sim 10^4$  K. Common assumptions in standard implementations of the cooling function  $\Lambda(u, \rho)$  is that the gas is optically thin and in ionization equilibrium. It is also usually assumed that three-body cooling processes are unimportant so as to restrict the treatment to two-body processes. For a plasma with primordial composition of H and He, these processes are: collisional excitation of  $\text{H}^0$  and  $\text{He}^+$ , collisional ionization of  $\text{H}^0$ ,  $\text{He}^0$ , and  $\text{He}^+$ , standard recombination of  $\text{H}^+$ ,  $\text{He}^+$ , and  $\text{He}^{++}$ , dielectric recombination of  $\text{He}^+$ , and free-free emission (bremsstrahlung). The collisional ionization and recombination rates depend only on temperature. Therefore, should an ionizing background radiation be absent, the resulting rate equations can be solved analytically. This leads to a cooling function  $\Lambda(u)/\rho^2$  as illustrated in the left panel of Fig. 3.9. On the other hand, in the presence of ionizing background radiation, the rate equations can be solved iteratively. Note that for a typical cosmological radiation background (e.g., UV background from star-forming

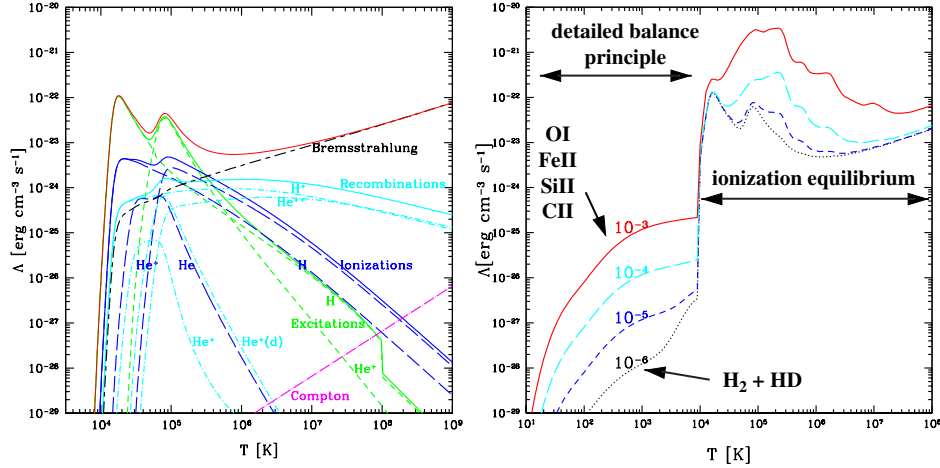


Fig. 3.9. Left panel: The total cooling curve (solid line) and its composition from different processes for a primordial mixture of H and He. Figure taken from [17]. Right panel: The total cooling curve as a function of different metallicity. The part below  $10^4$  K also takes into account cooling by molecules (e.g., HD and H<sub>2</sub>) and metal lines. Figure taken from [122].

galaxies and quasars, see [118–121]), the shape of the cooling function can be significantly altered, especially at low densities. For a more detailed discussion, see, for example, Chapter 6 and [17].

Additionally, the presence of metals will drastically increase the number of possible processes by which gas can cool. As it becomes computationally very demanding to calculate the cooling function in this case, cosmological simulations usually rely on a pre-computed, tabulated cooling function. As an example, the right panel of Fig. 3.9 shows the tabulated cooling function from [123], for temperatures above  $10^5$  K, for different metallicities of the gas, keeping the ratios of different metal species fixed to solar values. A refinement that is nowadays often exploited in simulations consists in using the `Cloudy` code ([124]), which allows users to tabulate the cooling and heating rates, individually for a grid of UV intensities and for various different chemical elements. In this way, cooling rates are self-consistently calculated for arbitrary chemical compositions. Note that almost all the implementations solve the above rate equations (and therefore the cooling of the gas) as a “subtime step” problem, decoupled from the hydrodynamical treatment. This translates in assuming that the density is fixed across the time step. Furthermore, the time step of the underlying hydrodynamical simulation is in general, for practical reasons, not controlled by nor related to the cooling time scale. The resulting uncertainties introduced by these approximations have not yet been deeply explored and clearly leave room for future investigations.

For the formation of the first objects in halos with virial temperatures below  $10^4$  K, the assumption of ionization equilibrium no longer holds. In this case, the non-equilibrium reactions have to be considered, by solving the balance equations

for the individual levels of each species during the cosmological evolution. In the absence of metals, the main coolants are  $\text{H}_2$  and  $\text{H}_2^+$  molecules (see [125]). HD molecules can also play a significant role. When metals are present, many more reactions are available and some of these can contribute significantly to the cooling function below  $10^4$  K. This effect is clearly visible in the right panel of Fig. 3.9 for  $T < 10^4$  K. For more details, see Chapter 6, Refs. [122, 126], and references therein.

### 3.12. Star formation

Star formation is a key astrophysical process which involves a hierarchy of physical processes: the accretion of gas from the large ( $\sim\text{Mpc}$ ) scale, gas cooling to produce neutral (HI) and molecular ( $\text{H}_2$ ) hydrogen ( $\sim\text{kpc}$  scale), the formation of giant molecular clouds (GMCs;  $\sim 10\div 100$  pc),  $\text{H}_2$  fragmentation and accretion to clumps ( $\sim 1$  pc) and cores ( $\sim 0.1$  pc), and the subsequent contraction of cores to form stars ( $\sim 10^{-8}$  pc). These complex processes, along with the description of the properties of the multi-phase star-forming ISM and the different regimes for star formation are thoroughly reviewed in a number of works, e.g. [127–130].

Star formation is the outcome of the gravitational collapse of clouds of dense and cold gas. Being the sub-pc scale where star formation actually occurs not captured in state-of-the-art cosmological hydrodynamical simulations, this is a sub-resolution process. From an order-of-magnitude estimate of masses and scales involved in cosmological simulation, gas elements have usually masses in the range of  $10^4 \div 10^7 M_\odot$  (they do not resolve GMCs), and have associated softenings comparable with or larger than a few hundreds pc (depending on resolution). Star particles have mass and force resolution comparable to gas elements, and are treated as SSPs. In summary, star formation in cosmological simulations aims at effectively capturing the drop out of cold gas which underwent radiative cooling into collisionless stellar particles.

A gas particle or cell is eligible to form stars if a number of criteria are met: the flow has to be locally convergent ( $\nabla \cdot \mathbf{v} < 0$ ) and Jeans unstable (i.e. the sound-crossing time exceeds the dynamical time); gas overdensity is larger than a critical overdensity (to prevent star formation in low-overdensity gas at very-high redshift); and the local number density of hydrogen atoms exceeds a threshold number density (see below). Details about the aforementioned conditions are provided in Chapter 6 (see also [17]).

A seminal work which advanced the description of the star-forming ISM in cosmological simulations and the numerical modelling of star formation is [131]. They introduced a model for the multiphase ISM, that accounts for star formation and stellar feedback. It considers that hot and cold gas components coexist in pressure equilibrium within dense gas particles, that are the so-called multiphase particles. Properties of the cold and hot phases are assumed to represent averages over small volumes of the ISM, since molecular clouds cannot be resolved. The cold phase

within the multiphase particle provides the reservoir for star formation, while being replenished by hot gas cooling. A fraction of the cold gas fuelling star formation is assumed to be instantaneously used to heat up the hot phase and to evaporate a share of the cold phase, mimicking the explosion of short-lived massive stars as SNe. Equations describing the evolution of the energy of the hot and cold gas phases are integrated, so that the star formation rate can be computed. Parameters of the model are calibrated to reproduce the Schmidt-Kennicutt relation [132, 133]. This model assumes a constant temperature ( $\sim 10^3$  K) for the cold gas component. Also, it is characterised by a quiescent, self-regulated star formation, as the fuelling of the cold phase owing to cooling is counterbalanced by its evaporation due to SN heating. Within this model, the ISM can be described by an effective equation of state: the effective pressure of the two-phase gas particles has a functional form that is constrained by the properties of the hot and cold phases, and is expected to be constant in time due to the self-regulated star formation.

Several sub-resolution models widely adopted in state-of-the-art cosmological simulations are inspired or loosely based on the aforementioned model. An interesting variation of this model considers that the density threshold for gas particles to become eligible to form stars depends on metallicity, based on the assumption that the higher the metallicity of the gas, the lower the density for warm and neutral gas to become cold and molecular [41, 134].

A relevant feature of the Springel and Hernquist model is the use of the effective equation of state for star-forming gas. It stems from the idea that the small-scale effects (e.g. thermal instabilities, turbulence, thermal conduction) which regulate the ISM are responsible for setting a self-regulated, equilibrium state of the ISM over short timescales. Within a similar regime, the average ISM temperature or energy can be approximated as a function of the warm/cold gas density only (see [135, 136] and [137] for examples of simulations not relying on the equation of state or on the presence of multiphase resolution elements, respectively).

As discussed above, the majority of numerical simulations of structure formation in a cosmological context are still far from resolving the structure of GMCs and from modelling star formation from first principles. They rather rely on various sub-resolution prescriptions that connect the SFR with the available gas eligible to form stars. This often translates in considering cold and dense gas ( $T \lesssim \text{a few} \times 10^4$  K;  $n \gtrsim 0.1\text{-}10 \text{ cm}^{-3}$ ), and in the assumption that the local SFR is proportional to its density over a timescale (close to the dynamical time of the cold gas). The aforementioned density and temperature thresholds to select star-forming gas actually reflect the physical properties of HI in the ISM. The latter proportionality is loosely inspired by the Schmidt-Kennicutt law [132, 133].

Examples of state-of-the-art cosmological simulations that adopt this approach feature Illustris [40], Magneticum [138], NIHAO [137], Illustris-TNG [139], the Massive-Black [39] and Fable [140] simulations, the Horizon-AGN suite [141, 142], the DIANOGA simulations [143, 144], the SLOW simulations [145].

Among the cosmological simulations which retrieve the SFR from the availability of molecular gas, estimated through the theoretical model by [146], it is worth mentioning the MUFASA and SIMBA simulations [44, 147], the FIRE suite [148, 149] and FIREBOX [150].

Other examples of cosmological simulations with a sub-resolution treatment of  $\text{H}_2$  include e.g., [122, 151–160]. Targeting the aforementioned simulations single haloes or smaller volumes, they manage to achieve a more refined modelling of the star-forming, molecular gas.

In what follows, we provide a short overview of the different prescriptions adopted by state-of-the-art cosmological simulations to select star-forming gas and to model star formation. The below-listed conditions usually come in addition to the ones mentioned at the beginning of this sub-section. The Illustris, Magneticum, Illustris-TNG and SLOW simulations all select the star-forming gas based on a density threshold ( $n_* \simeq 0.1 \text{ cm}^{-3}$ ), and assume a constant depletion timescale to convert cold gas into stars and estimate the SFR (based on [131]). The NIHAO simulations and the ERIS and GIGA-ERIS simulations [161, 162] adopt both a density and a temperature threshold to select star-forming gas.

Density and temperature thresholds are adopted also by simulations which rely on the MUPPI sub-resolution model (e.g. [135, 155, 160, 163–166]) to select multi-phase gas: star formation then proceeds from the fraction of cold gas which is molecular, as estimated via either the [167] or the [168] prescription; finally, the depletion timescale is the dynamical time of the cold gas. A more advanced modeling within MUPPI profits from the treatment of dust formation and evolution [165, 166] to predict the evolution of  $\text{H}_2$  [169], which in turn is used to estimate the local SFR.

In a similar fashion, the MUFASA and SIMBA simulations adopt an  $\text{H}_2$ -based prescription for the star formation following the [146] formula (considering that gas whose density exceeds a threshold is star forming), and assume that the depletion timescale is the local dynamical time. Similar assumptions to estimate the molecular gas out of the cold phase are made in the FIRE simulations.

The EAGLE and FLAMINGO simulation suites [6, 41] assume a metallicity-dependent star formation threshold [134] along with a temperature threshold: aiming at tying star formation to the molecular gas, they exploit the Cloudy radiative transfer code [124] to determine the transition from the warm, atomic to the cold, neutral gas phase. In these simulations, the SFR depends on pressure rather than on density. Interestingly, the HORIZON simulation suite (e.g., [142]) – which selects star-forming gas from gas cells above a given density threshold – features a locally-varying star formation efficiency (at variance with almost all the aforementioned simulations, where the fraction of cold/molecular gas which is converted into stellar particles is assumed to be constant).

[170, 171] address how different criteria adopted to select star-forming gas have a strong impact on simulated galaxies.

Star formation is often implemented according to a stochastic model: the process is not described for each star, rather stochastically with expectation values in agreement with the actual SFR. If, e.g., the probability  $p = m_{\text{gas}}/m_{\star}(1 - \exp(-m_{\star}/m_{\text{gas}}))$  exceeds a random number, then a new star particle is spawned [131]. As a refinement, a number of stellar generations can be assumed [172], so that newly spawned stellar particles have a given share of the mass of the gas element they come from as their initial mass.

### 3.13. Stellar evolution and chemical enrichment

Chemical evolution is a natural outcome of galaxy evolution in cosmological hydrodynamical simulations. Models of chemical evolution have been included in cosmological simulations of cosmic structure formation to properly address the study of the chemical enrichment process: the distribution of metals in the ISM and in the circum-galactic medium (CGM) encodes valuable information of the past history of star formation and feedback, and is a crucial feature of hydrodynamical simulations (e.g. [173, 174]). At variance with observations that explicitly resolve individual stars, cosmological simulations provide a coarse sampling of stellar populations by means of star particles. The majority of state-of-the-art cosmological hydrodynamical simulations of both large cosmological volumes and individual galaxies have star particles whose mass typically ranges between  $10^8$  and  $10^3 M_{\odot}$  according to resolution (e.g. [6, 36, 39–41, 135, 139, 155, 175–181]). In these simulations, star particles are resolution elements: each of them represents a simple stellar population (SSP), i.e. an ensemble of coeval stars that share the same initial metallicity. Every stellar particle initially shares the chemical composition of the gas element from which it has been originated, and is characterized by an initial mass function (IMF).

The IMF  $\phi(m)$  determines the number of stars per unit mass interval:

$$\phi(m) = \beta m^{-\alpha} , \quad (3.14)$$

within a given mass range  $[M_{\text{inf}}, M_{\text{sup}}]$ . The coefficient  $\alpha$  sets the slope of the power law over the mass range or in the different mass intervals within the mass range. For each mass interval, a normalization constant  $\beta$  is computed by imposing that  $\int m \phi(m) dm = 1$  over the global mass range and continuity at the edges of subsequent mass intervals.

Commonly assumed IMFs consist of single- [182, 183] or multiple-slope [184–186] power law, but more sophisticated shapes have been proposed (e.g. [187]). We refer the reader to [164, 188–193] for details about different IMFs and to appreciate how adopting different IMFs can have an impact on metal distribution on cosmological simulations.

The IMF directly regulates the relative ratio between stars of different initial mass, thus affecting the relative abundance of elements contributed by different types of stars. Stellar evolution predicts that all stars with masses larger than  $M_{\text{up}} =$

$8 M_{\odot}$  end their life as core collapse or type-II supernovae (SNe II) (see [194] and references therein). Under this assumption, the total amount of energy (typically  $10^{51}$  erg per SN) that each star particle can release in the surrounding gas can be calculated. Within the approximation that the typical lifetime of massive stars which explode as SNII does not exceed the typical time step of the simulation, feedback energy and metals are injected by the dying star in the so-called “instantaneous recycling approximation”, i.e. in the same time step. On the other hand, type-Ia SNe (SNe Ia) are believed to arise from the thermonuclear explosion of white dwarfs (see [195] and references therein). They lead to an explosion which is significantly delayed with respect to the time of creation of the star particle, as the white dwarf in a binary system has to accrete matter from the companion and reach the mass threshold for the onset of thermonuclear burning. Stars in the asymptotic giant branch (AGB) experience significant stellar mass loss and contribute significantly to the nucleosynthesis of heavy elements (see [196] and references therein).

Cosmological hydrodynamical simulations which feature an accurate model for stellar evolution and chemical enrichment can evaluate the number of stars aging and eventually exploding as SNe, as well as the amount of metals polluting the surrounding ISM. Besides assuming an IMF, commonly adopted models (e.g. [172]) include stellar lifetimes, delay functions and table of stellar yields to calculate the chemo-energetic imprint mainly left by SNe Ia, SNe II, and AGB stars.

Chemical evolution models account for the evolutionary timescales of stars with different masses by adopting mass-dependent lifetime functions (i.e. functions that describe the age at which a star of mass  $m$  dies, e.g. [197–199]). Stars with an initial mass larger than  $M_{\text{up}}$  and lower than  $M_{\text{sup,SNII}} = 40 M_{\odot}$  are assumed to end their life exploding as core-collapse SNe, while stars that are more massive than  $M_{\text{sup,SNII}}$  are assumed to implode in BHs directly, and thus do not contribute to further chemical enrichment or stellar feedback energy.

A fraction (usually constant) of stars relative to the whole mass range is assumed to be located in binary systems that are progenitors of SNe Ia. Assuming a stellar evolution scenario for SNe Ia (e.g. according to the model by [200]) and adopting lifetime functions and delay time distribution functions, the rate of SN Ia explosions can be computed.

The production of different heavy metals by stars that evolve and eventually explode is followed by adopting stellar yields. They represent the ejected mass of different metal species  $i$  produced by a star of mass  $m$  and initial metallicity  $Z$ , i.e.  $p_{Z_i}(m, Z)$ . In general, predictions for at least three main processes are needed: the continuous mass loss of AGB stars, SNe II and SNe Ia. Tables of mass- and metallicity-dependent stellar yields are incorporated in the chemical evolution models of state-of-the-art cosmological hydrodynamical simulations. Predictions for

stellar yield are still affected by uncertainties, mainly due to the poorly understood process of mass loss through stellar winds in stellar evolution models. Commonly adopted sets of stellar yields include: [201] for SNe Ia, mass- and metallicity-dependent yields by [202–204] for AGB stars, mass- and metallicity-dependent yields by [205–208] for SNe II. We refer the reader to (e.g. [209, 210]) for a comprehensive review of the analytic formalism.

As a final caveat, we note that comparisons of results from simulations to observations of single stars are usually performed under the assumption that e.g., the metal content of a star particle in simulations statistically reproduces the mean metallicity of the SSP that the star particle samples. More accurate techniques are introduced in [211, 212].

### 3.14. Stellar feedback

Stellar feedback is a key component of cosmological simulations of structure formation. Among its many crucial roles, it prevents overcooling at high redshift, distributes energy in the ISM, drives metals out of the star formation sites, and triggers galactic outflows, which guarantee a continuous interaction between the forming galaxy and its surrounding CGM. Since the understanding of the pc-scale physics responsible for launching and driving winds is still partial and however far from being implemented directly in cosmological simulations, these simulations have to resort to phenomenological prescriptions to capture the effects of galactic outflows. As for the sources of energy that power outflows and govern their kinematic, there are two commonly pursued approaches: winds can be either energy-driven or momentum-driven. For details about these two possible scenarios, we refer the reader to Chapter 6, which provides complementary information on the specific topic of this sub-section. This outline is far from being complete: deeper insight can be gained e.g. from [155, 213–215].

A variety of stellar feedback schemes has been proposed in cosmological simulations: the numerical description of the energy injection from SN explosions in the ISM has indeed a strong impact on final results. How reliable different sub-resolution models are in capturing an effective description of feedback energy injection is still debated.

SN energy can be distributed by star-forming gas elements to the surroundings in the form of thermal or kinetic energy. Injecting feedback energy as thermal, as in the pioneer model of [17], may have the limitation that the feedback usually does not result effective in driving energy far from regions where it is released. Gas elements surrounding those that provide energy have a typical temperature of  $\sim 10^5$  K and density high enough to radiate energy almost immediately, their cooling time being short. As a result, feedback is not effective in counterbalancing cooling and in preventing excessive star formation. To overcome this weakness, a stochastic thermal feedback model has been proposed [216], where gas receiving

thermal feedback energy is heated up to a temperature high enough to guarantee the effectiveness of feedback. Specifically, the aforementioned model assumes that thermal energy released by SN explosions is injected in the surrounding medium using a selection criterion: the gas particles that experience feedback have to be heated up to a threshold temperature, which is a parameter of the model (whose value is usually close to  $10^7$  K). Such a temperature increase ensures that the cooling time of a heated particle is longer than its sound-crossing time, so that heated gas can effectively leave the star formation site before it radiates all the energy away. It is worth noting that stellar feedback is actually implemented as a thermal channel in this model: however, the effective outcome is a galactic wind, because thermal energy is converted into momentum and hence outflows originate. This model for stellar feedback is for instance adopted by the EAGLE and FLAMINGO simulations [6, 41].

Otherwise, stellar feedback energy is provided in the form of kinetic energy and used to boost the velocity of surrounding gas elements (e.g. [131, 217]), which are kicked from their original position. They can eventually thermalise and radiate energy away, but later than in the thermal scenario by construction. To enforce the effectiveness of kinetic feedback schemes, particles that receive energy and sample galactic outflows (usually referred to as *wind particles*) are often decoupled from hydrodynamic interactions: in this way, they are prevented from being halted and from thermalising energy soon after they have been provided with.

An alternative stellar feedback model is represented by the so-called blast-wave feedback [218, 219]. Within this scheme, eligible particles are provided with thermal feedback energy, but are then prevented from cooling for a short period of time (typically few tens of Myr). The physical motivation behind this prescription stems from the evolution of a SN remnant in the ISM [220]. As soon as an exploding SN drives a blast wave, this undergoes a first phase of free expansion, followed by an adiabatic stage (the Sedov-Taylor phase) where radiative losses are negligible, before entering the radiative phase. Temporarily disabling cooling mimics the unresolved adiabatic phase, whose duration is estimated to be of order 30 Myr; afterwards, gas is allowed to cool again. Alternatively, the switch off of cooling can be explained by assuming that the energy released by SN explosions generates turbulence at unresolved scales and is partially dissipated over few tens of Myr, thus hindering gas cooling [221, 222]. When implemented in cosmological simulations, this feedback prescription results effective in avoiding excessive star formation and also succeeds at producing a two-phase ISM, whose gas components are not in pressure equilibrium locally.

Feedback processes through which massive stars can affect the reservoir of gas of a galaxy stem not only from the energy deposition and momentum injection following SN explosions, but also from the ionizing effect that massive stars have before exploding (usually referred to as early stellar feedback; e.g. [179]) and from stellar winds (e.g. [223, 224]). Specifically, the early stellar feedback by [179] represents a

UV ionization source, that increases the surrounding gas temperature and supplies heating and pressure support. This feedback channel pre-processes the star-forming ISM and facilitates the effectiveness of SNe at regulating star formation. In their simulations, [179] show how early stellar feedback helps in suppressing SF at high  $z$  (see also the NIHAO simulations to appreciate how early stellar feedback operates [137, 225]).

In addition, the energy released by SNe II is not expected to be constant across cosmic time nor in all the star-forming regions, and theoretical models predict that SNe exploding in almost pristine or weakly enriched environments provide the ISM with a larger amount of stellar feedback energy. The idea of differentiating the outcome of stellar feedback according to the physical properties of the star-forming ISM has been already pursued in cosmological simulations, and a few effective prescriptions have been proposed. The basic idea consists in adopting a non-constant value of the stellar feedback efficiency (i.e. the fraction of energy provided by each SN that is actually coupled to the surrounding gas as feedback energy).

A metallicity- and density-dependent stellar feedback efficiency has been introduced in the EAGLE simulations [41, 226]. There, the aforementioned efficiency decreases with gas metallicity while increasing with gas density. The adoption of a similar parametrization has a twofold reason: *i*) radiative losses are expected to increase with increasing metallicity; *ii*) energy losses in high-density, star-forming regions can make the stellar feedback too inefficient, and have to be counterbalanced. Being the gas metallicity lower at higher redshifts, when also higher densities are usually reached in the star-forming ISM, such a prescription yields a redshift-dependent stellar feedback efficiency. The latter ranges between asymptotic values, which are parameters of the model tuned to reproduce low-redshift observables, e.g. the galaxy stellar mass function.

A similar parametrization is adopted in the Illustris-TNG simulation [139], too. They assume that the wind energy available to a star-forming resolution element is metallicity-dependent. SNe II release indeed a feedback energy which spans the range  $(0.9 - 3.6) \times 10^{51}$  erg, according to the metallicity of the star-forming gas cell in which they are expected to explode – the lower the metallicity, the larger the energy budget. [139] demonstrate how the metallicity-dependent stellar feedback energy modulation has an impact both on the stellar-to-halo mass relation and on the galaxy stellar mass function, final results strongly depending on the tuning of the parameters. They show that the stellar mass of a  $\sim 10^{12} M_{\odot}$  halo at  $z = 0$  can vary by up to a factor of  $\sim 2$ .

At a higher level of complexity, though in simulations targeting smaller volumes, [227] first modelled the simultaneous evolution of different stellar populations in cosmological simulations. Their runs feature stellar feedback dependent on the underlying gas metallicity and stellar population, where the injected energy and the assumed stellar yields depend on Population III versus Population II regimes,

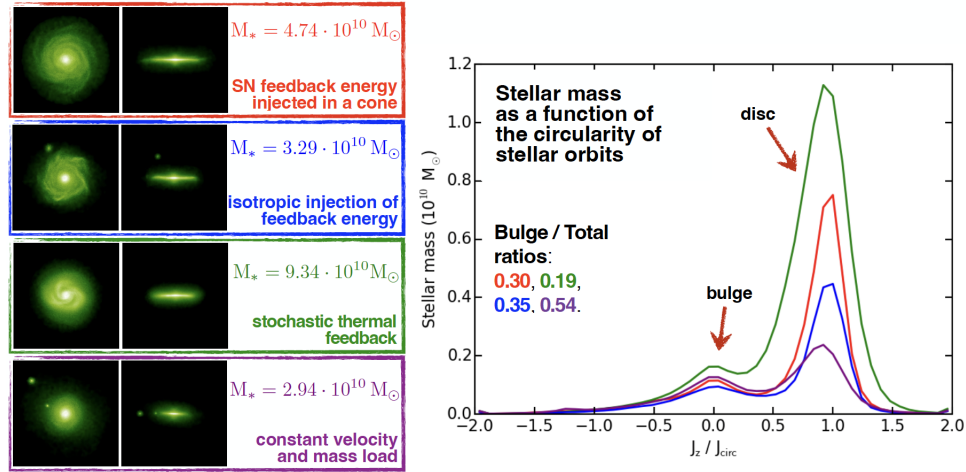


Fig. 3.10. Sensitivity of the final properties of simulated galaxies to the numerical prescriptions adopted to generate stellar feedback. Figures on the left show projected stellar density maps (face-on and edge-on) at redshift  $z = 0$ . Four models of galactic outflows are implemented within the same code (Gadget3) and used to simulate the formation of a Milky Way-like galaxy: stellar feedback energy injected either within a cone (red) or isotropically (blue), a stochastic thermal feedback scheme (green), and a model where galactic outflows have constant velocity and mass loading factor (purple). The galaxy stellar masses listed for each model are computed within one tenth of the galaxy virial radius. On the right, the same finding is quantified by analysing the stellar mass in the disc and in the bulge components of the simulated galaxies: a kinematic decomposition based on the circularity of the stellar orbits – through the ratio of specific angular momenta considered in the x-axis – is employed. Simulations from [135].

i.e. pair-instability SNe versus SNe. Interestingly, [228] included the effect of self-consistently coupled radiative transfer, concluding that radiative feedback from massive Population III stars could be a viable justification for powerful feedback in pristine environments.

Motivated by the aforementioned findings and by theoretical studies (e.g., [229, 230] for reviews) that suggest that hypernovae and SNe II of Population III stars can release energy higher than in the present-day Universe by more than a factor of  $\sim 10$ , [160] introduced an effective low-metallicity feedback. In this implementation of metallicity-dependent stellar feedback, they accounted for the effect of the explosion of hypernovae and SNe II in weakly-enriched environments, by boosting the energy released by SNe exploding in an almost pristine ambient medium (i.e. in an ISM with average metallicity below a threshold).

The impact of different sub-grid prescriptions accounting for the same physical process (stellar feedback and SN-triggered galactic outflows in this specific case) on final results is striking, though often overlooked. [135] investigate the impact of stellar feedback modelling on the formation and evolution of a disc galaxy, by performing a suite of cosmological zoom-in simulations of a Milky Way-size halo. They show how sensitive the general properties of the simulated galaxy are to the way in which

stellar feedback triggered outflows are implemented, comparing results obtained by adopting different state-of-the-art stellar feedback models (see Fig. 3.10). We refer the reader to [114, 115] for more extended comparison campaigns, i.e. the Aquila and the Agora comparison projects (see also Fig. 3.8). Interestingly, [215] also show how making different assumptions as for the stellar feedback efficiencies in the EAGLE and Illustris-TNG simulations reflects on the predicted galaxy stellar mass functions (see also [139, 226]).

### 3.15. Supermassive black holes in cosmological simulations

Observations suggest that almost every galaxy hosts a supermassive ( $10^8 \div 10^{10} M_{\odot}$ ) black hole (SMBH) in its innermost regions (e.g., [231–239]). A fraction of these BHs exhibits ongoing activity and is called AGN (active galactic nuclei). Evidence of past and ongoing activity is observed for instance in the X-ray images of elliptical galaxies and galaxy groups and clusters, where AGN imprints often appear as depressions and ripples. Among many, a well-known example is represented by the composite (X-ray, radio, and visual) image of the MS 0735+7421 galaxy cluster (e.g. [240]): giant X-ray cavities are filled with radio emission, and surrounded by a cocoon shock clearly visible in the Chandra image as an elliptical edge.

Before discussing AGN feedback (see Section 3.16), we are now recalling the main features of BHs in cosmological simulations, focusing on BH seeding and repositioning, BH-BH mergers, and AGN feeding.

The majority of cosmological simulations of galaxy and galaxy cluster formation that also include BHs and the associated AGN feedback are based on the seminal BH model by [241, 242], or follow its spirit. Therefore, this model offers the base to discuss a few key aspects of the treatment of BHs in cosmological simulations, and to highlight recent improvements.

In cosmological simulations, BHs are usually described as sink particles: these are collisionless particles that can absorb neighbour elements (originally implemented to allow the removal of surrounding particles in dense regions, e.g. [243]) and that have fundamental properties like the accretion rate which can be linked directly to observables.

BH particles are introduced in massive haloes at relatively high-redshift in cosmological simulations, and they are then allowed to grow and increase their initial or *seed* mass. The aforementioned, commonly quoted mass  $M_{\bullet}$  is the theoretical mass of the BH, modelled at the sub-resolution level, as opposite to its dynamical mass, i.e. the actual gravitational mass of the BH particle. As we are still lacking a solid understanding of the formation of first SMBHs (see e.g., [244–248] for possible pathways) and the resolution needed to take the physics of any seed formation scenario into account, BHs are first inserted according to seeding prescriptions (see also [249]).

Seeding prescriptions usually assume that new BHs (massive seeds of  $\sim 10^4 \div 10^6 M_{\odot}$ ) are introduced in haloes which meet some criteria and do not have already BHs. New BHs are seeded if: (i) the halo mass – commonly estimated by means of a FOF (Friend-Of-Friend, [250]) algorithm – is larger than a threshold (e.g., [6, 40, 41, 139]); (ii) the stellar mass exceeds a given value (e.g., [44]); (iii) the stellar mass and gas to stellar mass fraction are larger than given thresholds; (iv) based on gas properties, i.e. gas density, velocity dispersion and/or metallicity (e.g., [142, 251–253]). BH mass at seeding can be either constant (e.g., [6, 40, 41, 44, 139]) or scaled according to e.g., the  $M_{\text{BH}}/\sigma$  or  $M_{\text{BH}}/M_{*}$  scaling relations (e.g., [138]). Additional details involve the type of particles on which the FOF algorithm is performed, which can be for instance DM particles only (e.g., [254]) or stellar particles only (e.g., [138]). Besides, BH can be seeded at the position of the densest gas particle in the halo (e.g., [254]), of the star particle with the largest binding energy (e.g., [138]), or of the star particle closest to the centre of mass of the structure (e.g., [44]).

In cosmological simulations, each BH undergoes a specific evolution as an individual particle, at variance with the coarse-grained representation of collisionless fluids through particles in N-body simulations. As a result, the dynamics of BHs fails to be accurately captured and numerical artefacts can affect BH motion (see e.g., [255]). Spurious displacements of BHs, which often occur due to scattering between particles in high-density environments and numerical heating, have dramatic consequences, such as e.g., artificial presence of wandering BHs, incorrect description of BH-BH mergers, BHs producing feedback off-centre with respect to their galaxy hosts. To avoid these artefacts, BH dynamics is commonly controlled through different approaches: re-positioning via pinning on e.g. minimum potential (e.g., [40, 41, 44, 139]), boosted dynamical mass (e.g., [144]), boosted dynamical mass and dynamical friction (e.g., [138, 145]). We refer the reader to [35, 143, 249, 254, 256–260] for details and recent improvements.

BHs grow because of gas accretion and mergers with other BHs. As for the latter channel, BHs are expected to merge when their host galaxies and their haloes merge to form a single structure. The commonly pursued approach [241, 242] in cosmological simulations assumes that two BH particles merge quickly if their distance approaches the spatial resolution of the simulation (or a small multiple of it). The force resolution set by the gravitational softening determines indeed the minimum scale above which gravitational interactions can be properly followed. Additional conditions involving e.g. the merging BH relative speed have been implemented [254]. The two BHs are eventually merged into a single BH particle, with their masses combined.

As for AGN feeding, gas accretion onto a BH of mass  $M_{\bullet}$  is calculated according to the Bondi formula [261–263], multiplied by a so-called boost factor  $\alpha$ :

$$\dot{M}_{\text{B}} = \frac{4\pi \alpha G^2 M_{\bullet}^2 \langle \rho \rangle}{(\langle c_s \rangle^2 + \langle v \rangle^2)^{3/2}}. \quad (3.15)$$

Here,  $G$  is the gravitational constant,  $\langle \rho \rangle$ ,  $\langle v \rangle$ , and  $\langle c_s \rangle$  are mean values at the scale resolved by the hydrodynamical simulation: for example, they are computed using kernel weighted estimates in the case of SPH. The BH accretion rate  $\dot{M}_B$  is commonly capped to the Eddington accretion rate  $\dot{M}_{\text{Edd}}$ <sup>6</sup> (but see [44, 264] for examples of  $\dot{M}_\bullet$  which breaches the Eddington limit).

The boost factor  $\alpha$  has been originally introduced [241] to account for the limited resolution in simulations, which leads to smaller densities and larger temperatures near the BH (and thus to an underestimate of  $\dot{M}_B$ ). A typical value is  $\alpha = 100$ . Several studies adapt the BH model by using a boost factor which depends on resolution [265, 266], density [267], or pressure [268]. Other simulations instead limit the BH accretion rate by taking into account the angular momentum of accreting gas [269, 270]. High-resolution simulations of BH accretion on sub-kpc scales [271] found that a boost factor of order of 100 is suitable when including cooling and turbulence, while pure adiabatic accretion suggests boost factors smaller by an order of magnitude. Hence, advanced models distinguish between hot and cold gas accretion and use different boost factors for the two components [272], or can even get rid of fudge factors (e.g., [139, 270]).

By exploiting the BH accretion rate  $\dot{M}_\bullet$ , the bolometric luminosity  $L_{\text{bol}}$  can be associated to each BH in the simulation. A common assumption consists in following [273] to distinguish between high and low BH accretion state in terms of the Eddington ratio  $f_{\text{Edd}} = \dot{M}_\bullet / \dot{M}_{\text{Edd}}$  (i.e. the ratio between the BH and the Eddington accretion rates) and compute:

$$L_{\text{bol}} = \begin{cases} 10 (\epsilon_r c)^2 \dot{M}_\bullet & f_{\text{Edd}} > 0.1 \\ (10 \epsilon_r c)^2 f_{\text{Edd}} \dot{M}_\bullet & f_{\text{Edd}} \leq 0.1 \end{cases} \quad (3.16)$$

(see [274, 275]). In contrast to the original model [241, 242], modern implementations often correct the accretion rate  $\dot{M}_\bullet$  of the BH by a factor  $(1 - \epsilon_r)$ . As a consequence,  $L_{\text{bol}} = \epsilon_r / (1 - \epsilon_r) \dot{M}_\bullet c^2$ , and the energy radiated away during the accretion process is taken into account. Different prescriptions for the accretion rate, in combination with the change of the ISM/IGM properties produced by the combined action of all the sub-grid processes, typically leads to significant variations in the predicted evolution of the AGN luminosity function among the various state-of-the-art simulations. This is summarized in Fig. 3.11, where we can appreciate how predictions from simulations can strongly deviate from the observed AGN luminosity function across cosmic time (see also discussion in [275]).

<sup>6</sup> $\dot{M}_{\text{Edd}} = (4\pi G m_p M_\bullet) / (\sigma_T c \epsilon_r)$ , with  $m_p$  the proton mass,  $\sigma_T$  the Thompson cross section,  $c$  the speed of light and  $\epsilon_r$  the radiative efficiency, typically assumed to be  $\approx 0.1$ .

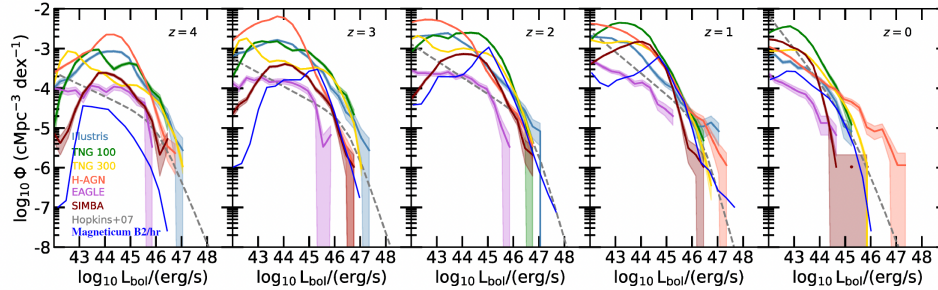


Fig. 3.11. Comparison of the evolution of the observed AGN luminosity function with the predicted one from different simulations incorporating various AGN models (as described in Section 3.16). Predictions from simulations are very sensitive to the details of the sub-grid models. Adapted from [275], and extended by including results from Magneticum, as shown in [35, 274].

### 3.16. AGN feedback in state-of-the-art cosmological simulations

Observations allow us to appreciate how AGN feedback develops with different mechanisms (for instance inflating bubbles or launching outflows), with different appearances, in a variety of systems. Besides, it is a recurrent process, with each AGN burst leaving a clear signature in the system. Additional evidence which adds complexity to the comprehension and modelling of AGN feedback is the presence of multiphase gas in and around galaxies. Multiwavelength observations reveal the presence of gas spanning a wide range of densities, temperatures, and ionisation states in galaxies. Multiphase gas is present not only in spiral galaxies, which are systems rich in cold gas, but also in ellipticals and in the innermost regions of galaxy groups and clusters, which are environments known to be dominated by X-ray emitting, hot gas.

Observations ([276, 277] among other works) also provide evidence for different regimes of BH accretion and feedback. In a simplified context, the AGN activity operates through (at least) two distinct phases: radiative or quasar mode, and kinetic or radio mode ([278] for a review). The radio-mode is characterized by large radio jets generating hot X-ray cavities, whereas in the quasar-mode the emission is dominated by the accretion disc, and feedback energy is mainly radiated away. This distinction has been theoretically modelled [273] by describing AGN feedback with two components: radiation and mechanical outflows ([279] considered three different regimes for BH accretion in their model). In these models, the amount of energy associated with each component depends on the Eddington ratio  $f_{\text{Edd}}$  (see Section 3.15). Not only are simple theoretical models like the two aforementioned ones supported by observations, but they are also corroborated by other independent analytical models ([280] and references therein), which showed how it is possible to associate different BH accretion rates to changes in the radiative efficiency and to transitions to different types of accretion discs. In addition, observations [281, 282]

suggest that the radiative efficiency does not only correlates with the BH accretion rate, but also with the BH mass (see also [272]).

However, a two-mode AGN feedback is only an approximation to the smooth transition which is observed (e.g., [276, 283]) and also theoretically expected (e.g., [280, 284–286]). Reality is in fact more complex than the aforementioned simplified frameworks, and AGN feedback operates through a variety of modes, which often occur simultaneously. Among the main AGN feedback mechanisms, there is the preventive (or preventative) mode, where feedback prevents the gas from being accreted or from effectively cooling; the ejective mode, in which gas is removed from the innermost regions of forming structures where SF occurs; AGN feedback can suppress the SF efficiency, mainly via turbulence and ISM heating; it can operate via radiation pressure on dust, which clears out gas from the BH vicinity; or AGN can act in the maintenance mode, by keeping quiescent an already quenched system. Besides all the aforementioned modes in which BH feedback is negative, i.e. it produces an overall suppression of the SFR, AGN feedback can also be positive and locally enhance the SF efficiency for a given period of time, mainly via ISM overpressurization. Different regimes have to be accounted for to address the overall AGN feedback problem, always considering that AGN and their host galaxies are embedded in a DM halo.

Another key characteristic of AGN is that it develops across a large dynamical range of scales, and that it impacts on the evolution of gas with a range of densities and temperatures. This can occur from nuclear scales to galaxy cluster scales, moving through the ISM, the CGM, the intra-group medium and the ICM. This large range in spatial scales corresponds to an equivalently wide range in temporal scales (e.g., [287]).

State-of-the-art cosmological simulations are still far from fully capturing the complexity. Starting from the seminal works by [241, 242], a number of prescriptions for modelling AGN feedback have been conceived to account for SMBH feedback in cosmological simulations. Following the two aforementioned papers, many simulations assume that the AGN feedback energy that a SMBH accreting at a rate  $\dot{M}_\bullet$  releases per unit time can be cast as:

$$\dot{E} = \epsilon_f \epsilon_r \dot{M}_\bullet c^2, \quad (3.17)$$

where  $\epsilon_r$  and  $\epsilon_f$  are the radiative and the feedback efficiencies, respectively.

A constant value for the radiative efficiency  $\epsilon_r$  is often used. It is often set to 0.1 [141, 241], which corresponds to the mean value for the radiatively efficient accretion onto a non-spinning, Schwarzschild BH [288–290]. Recent works (e.g., [142, 291]) included a BH spin-dependent  $\epsilon_r$ .

The feedback efficiency  $\epsilon_f$  quantifies the fraction of energy radiated from the BH which is actually coupled to the. Values commonly assumed in cosmological simulations span the range  $\sim 10^{-4} - 0.2$  (e.g., [35, 139, 292–296]). This efficiency is often tuned in order to match the normalisation of the BH to stellar mass relation

[231, 238]. The value of  $\epsilon_f$  can be either constant (e.g., [41, 241]), or dependent on the AGN mode. Motivated by the observational evidence of more powerful outflows associated with SMBHs accreting at lower rate [273, 279, 297], [298] introduced a steep transition of the feedback efficiency between quasar-mode and radio-mode, (see also [35, 44, 141, 268, 299, 300]). Even within the same (radio) mode,  $\epsilon_f$  can change according to the ISM density [139, 301].

AGN feedback energy can be deposited by means of different numerical prescriptions: either purely in the form of thermal or kinetic energy, or it can be used to inject bubbles, or according to different channels depending on e.g., the BH accretion rate. Among the several possible AGN feedback models, it is worth highlighting a number of schemes that modern cosmological simulations adopt.

Following the original idea of [241, 242], the AGN feedback energy can be simply dumped thermally: in this way, the BH distributes the AGN feedback energy (eq. 3.17) to nearby resolution elements, possibly in a kernel-weighted fashion. The thermal energy received is used to increase the internal energy of particles or cells surrounding the BH, which increase their temperature as a consequence. While being overall effective, this simple prescription often turns out to be inefficient and does not succeed at reproducing the variety of observations currently available at different redshift. Nonetheless, this prescription is still widely used in cosmological simulations, that often adopt it to describe the quasar-mode feedback only, along with a complementary model for lower BH accretion rates. As an example, [35, 139, 141, 142, 145, 268] rely on this model to describe the quasar-mode feedback in their simulations.

Indeed, in the *Magneticum* and in the *SLOW* simulation suites, they assume a two-mode AGN feedback: for high BH accretion rates, i.e.  $f_{\text{Edd}} > 0.01$ , SMBHs experience a quasar phase and release thermal energy in the surrounding. On the other hand, they model the radio-mode feedback ( $f_{\text{Edd}} < 0.01$ ) through energy deposition by hot bubbles (following [299, 302]). In these simulations, radiative and feedback efficiencies are free parameters. Specifically,  $\epsilon_f$  is increased by a factor of 4 during the radio-mode feedback with respect to the quasar phase. Interestingly, in a subset of the *Magneticum* simulations [272], they explore a different scenario for a two-mode AGN feedback, where hot bubbles are replaced by outflows. However, due to the limited resolution, the latter mechanical channel is numerically implemented as thermal feedback.

While the *Illustris* simulation [40, 268] implements AGN feedback in a similar way to *Magneticum* (i.e. thermal feedback for  $f_{\text{Edd}} > 0.05$  and bubble-like feedback below), the *Illustris-TNG* simulation substantially improves the modelling of the mechanical component of the BH feedback [139, 301]. Indeed, besides adding a BH mass dependence to the BH accretion rate threshold which distinguishes between quasar and radio mode, they explicitly model kinetic winds in the radio mode, by adding momentum with random injection directions to selected gas cells (see [301] for details). Interestingly, both *Illustris* and *Illustris-TNG* include a radiative

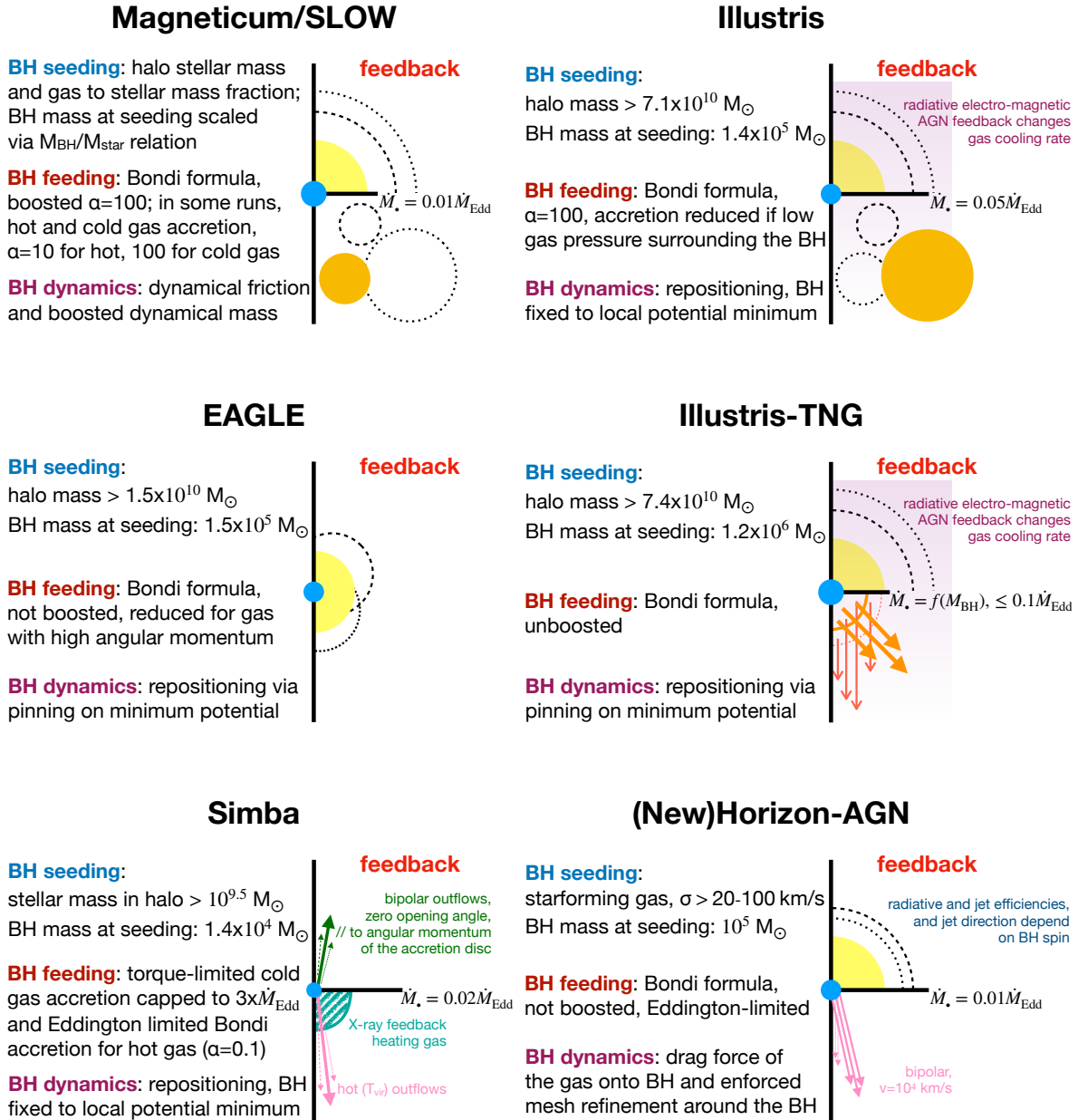


Fig. 3.12. The six cartoons summarise the main properties of BH seeding and accretion, and sketch the implementation of AGN feedback in six among the most common state-of-the-art cosmological simulations. In the right part of each panel, we highlight the BH accretion rate threshold above (top) or below (bottom) which different AGN feedback prescriptions are used, should a two-mode feedback be present in that simulation suite.

(electro-magnetic) AGN feedback via a phenomenological model. This latter feedback channel modifies the net cooling rates of halo gas. Even though it operates whatever the  $\dot{M}_\bullet$ , it proved effective only for BH accretion rates close to Eddington.

The EAGLE simulations [41] adopt a stochastic thermal feedback scheme, where accumulated AGN feedback is injected only when enough to heat the surrounding ISM up to a sufficiently-high temperature ( $T \sim 10^{8.5} \div 10^9$  K), similarly as for the case of stellar feedback (see Secton 3.14). This choice is also the fiducial option in the reference runs of the FLAMINGO suite [6], although they foresee the possibility to adopt instead a jet-mode, kinetic AGN feedback. In the latter case, should jets be on, they are launched according to the BH spin direction. AGN feedback in these two simulation suites [6, 41] is always one-mode.

Simba simulation [44, 303, 304] includes a two-mode AGN feedback: a radiative and a jet mode. BHs in the radio mode ( $f_{\text{Edd}} > 0.02$ ) promote AGN winds, with velocity proportional to the BH mass, that do not alter the temperature of the outflowing gas. During the jet-mode (for low  $f_{\text{Edd}}$  and if  $M_\bullet > 10^{7.5} M_\odot$ ), the temperature of the gas involved in outflows is instead raised to the virial temperature of the halo. Both types of winds are produced via momentum input. When the jet-mode is active, there is an additional heating channel, namely the X-ray feedback: it releases energy into the BH surrounding gas, which is supposed to originate from X-rays of the accretion disk.

In the (New)Horizon-AGN [141, 142, 300, 305] AGN feedback features two modes, depending on the BH accretion rate. During the radio mode, the BH powers jets, continuously releasing mass, momentum, and total energy into the gas. On the other hand, only thermal energy is supplied to the gas cells within a sphere centred on the BH when it is in quasar mode. As for the jet mode, BH jets are bipolar, launched with a constant velocity, and they deposit mass, momentum and energy within a cylinder. In the New Horizon-AGN simulation, radiative and feedback efficiencies are BH spin-dependent (both in quasar and radio mode).

Fig. 3.12 summarises the numerical prescriptions that some modern cosmological simulations adopt to model BH growth, AGN feeding and feedback. The six sketches in the aforementioned figure aim at providing a simplified yet immediate understanding and comparison among the various models.

The compilation of prescriptions for AGN feedback listed above is far from being complete. Other works which is worth mentioning include e.g., [140, 306–309].

A few remarks on AGN feedback modelling in simulations follow, about: (i) model parameter calibration; (ii) the simplification underlying many of the state-of-the-art models; and (iii) comparison among different models.

Subgrid physics and in particular free parameters of the models, are usually tuned to reproduce observables. This is especially true for AGN feedback efficiencies (i.e.  $\epsilon_f$  and  $\epsilon_r$ ). The majority of cosmological simulations calibrate free parameters (possibly within ranges suggested by theory or phenomenology or data) by attempting to reproduce a number of observables. The most popular examples are the BH

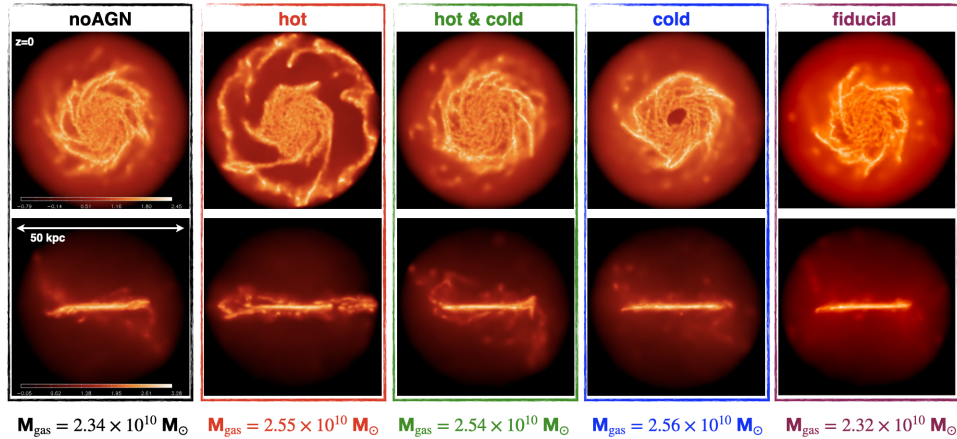


Fig. 3.13. Impact of different ways of distributing AGN feedback energy on the final morphology of simulated disc galaxies. Besides the reference run where no BHs are included (first column), we show the final morphology of a suite of Milky-Way like galaxies which have been simulated assuming that AGN feedback energy (*i*) is entirely distributed to the hot phase of the multiphase ISM (second column), (*ii*) is evenly provided to hot and cold gas (third column), (*iii*) is coupled to the cold phase only (fourth column), or (*iv*) is supplied to hot and cold gas according to their physical properties (i.e., depending on the covering factor of the cold clouds, fifth column). Figure panels show projected gas density maps (top panels: face-on, bottom panels: edge-on) of five simulated galaxies, at redshift  $z = 0$ . The size of each box is 50 kpc a side. Colour bars encode the logarithm of projected densities ( $M_{\odot}/\text{pc}^2$ ); panels in each row share the same colour bar. Shown are also the mass of gas within 0.1 of the galaxy virial radius. Adapted from [270].

to stellar mass relation [231, 238] and the galaxy stellar mass function (GSMF, e.g. [310]), usually at redshift  $z = 0$ . Other calibration targets include: the galaxy mass-size relation, baryon or gas mass fractions, metallicity-mass and luminosity-mass relations. We refer the reader to [226] for a more extended discussion. Common strategies to model calibration consist in performing a fit to selected data sets (e.g. EAGLE), to exploit trends in comparison to some observations (e.g. Magneticum, Illustris), to profit from machine learning (e.g. FLAMINGO) or from comparison to previous/scaled-down versions of similar simulations.

There are as well different approaches when resolution changes. Weak convergence (as opposite to strong convergence, see [41]) is usually preferred, and for different numerical resolutions it is common practice to adapt at least a few values of the model parameters.

However, the choice of the observational data sets adopted for calibration does not impact parameter tuning only. Rather, it allows to understand the performance of different simulation predictions against various observations. For instance, the Magneticum simulation succeeds at reproducing the physical properties of the ICM and of the intra-group medium better than other simulations (see [311] for an example), while simulations like Illustris-TNG, Simba and EAGLE usually outperform the competition as for predicting final properties of the galaxy population. This

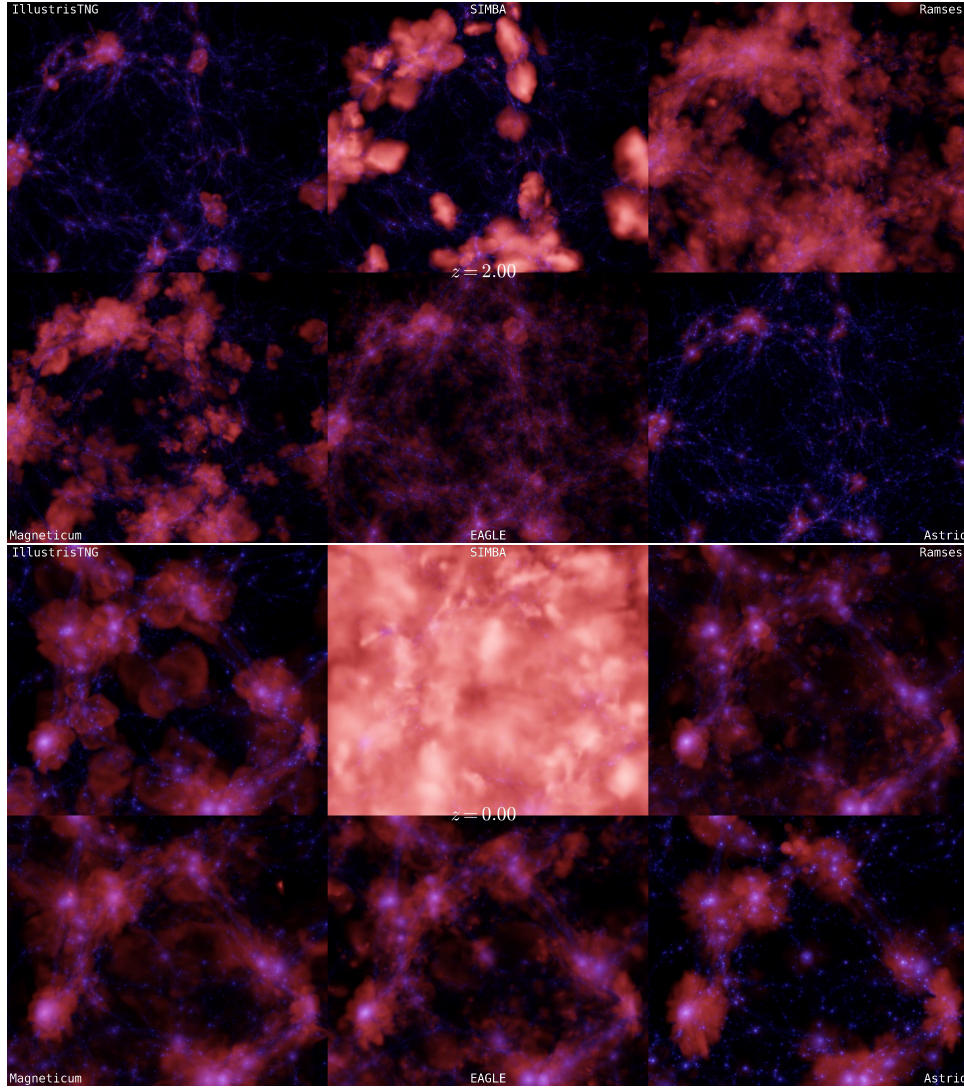


Fig. 3.14. Comparison of the evolution of the ISM (the displayed density maps are color coded by temperature) within a small, cosmological volume evolved within the CAMELS project. Six different sub-grid models which have been used in recent simulation campaigns are compared (see labels). The upper 6 panels show the simulations at  $z = 2$ , while the lower panels show the simulations at  $z = 0$ , so as to also emphasize the different time evolution inherited in the different implementations. Credits: F. Villaescusa-Navarro.

mainly stems from the calibration targets, i.e. ICM and stellar metallicity content, plus X-ray luminosity-mass relation for the Magneticum simulation versus GSMF and galaxy mass-size in the others.

Among the many assumptions underlying any sub-grid model, one simplification consists in accepting that little is known about how AGN feedback energy couples with different phases of the ISM. [270] investigate how relevant it is to distribute AGN feedback energy to the individual phases of the ISM. Within the MUPPI sub-resolution model [135, 155], they show the impact of supplying feedback energy to hot or cold gas only, of evenly providing the two phases with BH feedback energy, and of coupling AGN feedback energy to the hot and cold gas according to their physical properties (i.e. the covering factor of cold clouds). They find that the numerical prescriptions adopted to couple AGN feedback energy to the ISM phases affect final BH and host galaxy properties (see Fig. 3.13). Interestingly, they assume that AGN feedback energy is used either to increase the hot gas temperature, or to evaporate molecular gas, instead of e.g. producing a deviation from the equilibrium solution of multiphase particles [241].

Finally, assessing the differences among different models for AGN feeding and feedback is not straightforward. We refer the interested reader to [312] for a reference comparative study where the impact of various prescriptions for BH seeding, AGN feeding and feedback has been addressed. Different implementations are tested with the same cosmological simulation also in the CAMELS project [313]. Here, Fig. 3.14 (along with the associated movie) provides evidence of how various sub-grid models adopted in some state-of-the-art cosmological simulations predict differences as for the energy distribution and the evolution of the IGM/CGM.

### 3.17. Current state and perspectives

Even nowadays, the cosmological simulations used as theoretical counterparts for very large surveys (like EUCLID, DESI, LSST), for which extremely large volumes need to be sampled, are based on pure gravitational physics (e.g., [10, 14]). These simulations are usually complemented by running semianalytic models (SAMs) of galaxy formation (e.g., [314]). While SAMs provide a realistic description of the properties of galaxy populations, they bring at best indirect information on the properties of the ISM/IGM. In fact, they do not include a self-consistent treatment of gas dynamics and loosely capture the effects of baryons on structure formation, which is highly relevant for the study of environmental effects.

In the last decades, a growing number of different, large-scale, cosmological, hydro-dynamical simulations have been performed with varying resolutions and volumes covered (see initial Fig. 3.1 in section 3.1). One limitation of state-of-the-art cosmological simulations is that different sub-grid models often predict very similar results in direct observable properties, and the main differences among their outcome are often hidden in properties which are not directly or easily accessible (like the IGM/CGM of galaxies), and/or in the different evolution of them (see Fig. 3.14). This weakens the predictive power of individual simulations, and undermines the possibility to ascribe discrepancies among simulations to different

numerical prescriptions adopted or to physical processes included. Comparing predictions from simulations with observations can help to constrain the theoretical modelling: however, evaluating differences fairly is not trivial. In fact, the comparison process often involves sophisticated techniques to create meaningfully mock observations (e.g., [211, 315]), and also has to cover multi-wavelength regimes and different components (e.g., stars, gas, dust, ...) simultaneously.

Several lines of refinement have been under development during the last years. They include, for instance, hyper-refinement in the innermost regions of simulated structures [316–318], to increase the resolution in those regions which are crucial to better resolve to capture additional physics. Not only is higher resolution needed in the densest regions or around SMBHs, but it is fundamental also increase the spatial refinement within the virial radius, to capture CGM physics and evolution more accurately (e.g., [319]). Also, a number of works have included a detailed modelling of sub-resolution accretion discs and BH spin modelling [291, 305, 320–322], and have progressed in linking the accretion process onto SMBHs with the launch of AGN-triggered jets [323]. Furthermore, the modelling of SMBH outflows and jets has been enhanced [301, 324], and interests experiments involve the inclusion of spin-driven (Blandford-Znajek) AGN jets [325, 326]. So far, these improvements have been validated mainly with dedicated and somehow ad-hoc setups, or included in cosmological simulations of smaller haloes or volumes. As the numerical advancement of the aforementioned improvements has been included in state-of-the-art codes, we expect that these new modules will be featured by upcoming large-volume simulations, and improve the accuracy of the numerical prediction in the near future.

While the predictive power of modern cosmological simulations is beyond discussion, still there are several caveats that cannot be overlooked. The majority of state-of-the-art cosmological simulations, for instance, assume that all haloes above a mass threshold host BHs, and adopt massive BH seeds to promote their early growth. Also, they commonly rely on Bondi accretion – though with modifications – to facilitate the initial growth of BHs and to make them easily reach the Eddington limit.

In addition, the implementation of feedback processes is still far from reaching an adequate degree of complexity, and it is often driven by numerical effectiveness. Besides, several feedback processes (e.g., early feedback, radiation from stars, stellar and AGN winds, radiation pressure on dust) which could hamper BH growth and reduce the SFR are often neglected. A number of relevant physics modules are still not included in the reference runs of the majority of cosmological simulations of large volumes, as their integration in the existing framework is not straightforward. As an example, it is worth mentioning: radiative transport, cosmic rays, magnetic fields, scenarios for DM alternative to the standard  $\Lambda$ CDM, chemical diffusion, just to name a few. The need for higher spatial resolution makes it difficult to consistently account for all the relevant physics.

Finally, it is worth recalling that we have now entered the era of high-performance computing, with always growing computational power available from current and future HPC facilities. It is therefore of paramount importance to have numerical codes which are not only as complete as possible as for the inclusion of physical processes implemented, but also very efficient from the computational point of view. Codes are indeed supposed to be able to smoothly scale on state-of-the-art exascale infrastructures, and to efficiently exploit CPUs (Central Processing Units) and GPUs (Graphics Processing Units).

The aforementioned efforts, together with the improvements in numerical methods, will allow us to study the formation process of cosmological structures with unprecedented detail, and to better link the small-scale physical processes of galaxy formation to the evolution of the large-scale structure and of the cosmic web.

## References

- [1] K. Yoshikawa, N. Yoshida, and M. Umemura, Direct Integration of the Collisionless Boltzmann Equation in Six-dimensional Phase Space: Self-gravitating Systems, *ApJ*. **762**, 116, (2013).
- [2] K. Dolag, S. Borgani, S. Schindler, A. Diaferio, and A. M. Bykov, Simulation Techniques for Cosmological Simulations, *Space Sci. Rev.* **134**, 229–268 (Feb., 2008). doi: 10.1007/s11214-008-9316-5.
- [3] V. Springel, High Performance Computing and Numerical Modelling, *Star Formation in Galaxy Evolution: Connecting Numerical Models to Reality, Saas-Fee Advanced Course, Volume 43. ISBN 978-3-662-47889-9. Springer-Verlag Berlin Heidelberg, 2016, p. 251.* **43**, 251, (2016).
- [4] J. Binney and S. Tremaine, *Galactic Dynamics: Second Edition*. (Princeton University Press, 2008).
- [5] S. Bocquet, A. Saro, K. Dolag, and J. J. Mohr, Halo mass function: baryon impact, fitting formulae, and implications for cluster cosmology, *MNRAS*. **456**, 2361–2373 (Mar., 2016). doi: 10.1093/mnras/stv2657.
- [6] J. Schaye, R. Kugel, M. Schaller, J. C. Helly, J. Braspennig, W. Elbers, I. G. McCarthy, M. P. van Daalen, B. Vandenbroucke, C. S. Frenk, J. Kwan, J. Salcido, Y. M. Bahé, J. Borrow, E. Chaikin, O. Hahn, F. Huško, A. Jenkins, C. G. Lacey, and F. S. J. Nobels, The FLAMINGO project: cosmological hydrodynamical simulations for large-scale structure and galaxy cluster surveys, *MNRAS*. **526**(4), 4978–5020 (Dec., 2023). doi: 10.1093/mnras/stad2419.
- [7] V. Springel, S. D. M. White, A. Jenkins, C. S. Frenk, N. Yoshida, L. Gao, J. Navarro, R. Thacker, D. Croton, J. Helly, J. A. Peacock, S. Cole, P. Thomas, H. Couchman, A. Evrard, J. Colberg, and F. Pearce, Simulations of the formation, evolution and clustering of galaxies and quasars, *Nature*. **435**(7042), 629–636 (June, 2005). doi: 10.1038/nature03597.
- [8] R. E. Angulo, V. Springel, S. D. M. White, A. Jenkins, C. M. Baugh, and C. S. Frenk, Scaling relations for galaxy clusters in the Millennium-XXL simulation, *MNRAS*. **426**(3), 2046–2062 (Nov., 2012). doi: 10.1111/j.1365-2966.2012.21830.x.
- [9] S. W. Skillman, M. S. Warren, M. J. Turk, R. H. Wechsler, D. E. Holz, and P. M. Sutter, Dark Sky Simulations: Early Data Release, *arXiv e-prints*. art. arXiv:1407.2600 (July, 2014). doi: 10.48550/arXiv.1407.2600.

- [10] D. Potter, J. Stadel, and R. Teyssier, PKDGRAV3: beyond trillion particle cosmological simulations for the next era of galaxy surveys, *Computational Astrophysics and Cosmology*. 4(1):2 (May, 2017). doi: 10.1186/s40668-017-0021-1.
- [11] J. D. Emberson, H.-R. Yu, D. Inman, T.-J. Zhang, U.-L. Pen, J. Harnois-Déraps, S. Yuan, H.-Y. Teng, H.-M. Zhu, X. Chen, and Z.-Z. Xing, Cosmological neutrino simulations at extreme scale, *Research in Astronomy and Astrophysics*. 17(8):085 (Aug., 2017). doi: 10.1088/1674-4527/17/8/85.
- [12] K. Heitmann, H. Finkel, A. Pope, V. Morozov, N. Frontiere, S. Habib, E. Rangel, T. Uram, D. Korytov, H. Child, S. Flender, J. Insley, and S. Rizzi, The Outer Rim Simulation: A Path to Many-core Supercomputers, *ApJS*. 245(1):16 (Nov., 2019). doi: 10.3847/1538-4365/ab4da1.
- [13] K. Heitmann, N. Frontiere, E. Rangel, P. Larsen, A. Pope, I. Sultan, T. Uram, S. Habib, H. Finkel, D. Korytov, E. Kovacs, S. Rizzi, J. Insley, and J. Y. K. Knowles, The Last Journey. I. An Extreme-scale Simulation on the Mira Supercomputer, *ApJS*. 252(2):19 (Feb., 2021). doi: 10.3847/1538-4365/abcc67.
- [14] T. Ishiyama, F. Prada, A. A. Klypin, M. Sinha, R. B. Metcalf, E. Jullo, B. Altieri, S. A. Cora, D. Croton, S. de la Torre, D. E. Millán-Calero, T. Oogi, J. Ruedas, and C. A. Vega-Martínez, The Uchuu simulations: Data Release 1 and dark matter halo concentrations, *MNRAS*. **506**(3), 4210–4231 (Sept., 2021). doi: 10.1093/mnras/stab1755.
- [15] N. Frontiere, K. Heitmann, E. Rangel, P. Larsen, A. Pope, I. Sultan, T. Uram, S. Habib, S. Rizzi, J. Insley, and HACC Collaboration, Farpoint: A High-resolution Cosmology Simulation at the Gigaparsec Scale, *ApJS*. 259(1):15 (Mar., 2022). doi: 10.3847/1538-4365/ac43b9.
- [16] C. A. Metzler and A. E. Evrard, A simulation of the intracluster medium with feedback from cluster galaxies, *ApJ*. **437**, 564–583 (Dec., 1994). doi: 10.1086/175022.
- [17] N. Katz, D. H. Weinberg, and L. Hernquist, Cosmological Simulations with TreeSPH, *ApJS*. **105**, 19–+ (July, 1996). doi: 10.1086/192305.
- [18] F. R. Pearce, A. Jenkins, C. S. Frenk, J. M. Colberg, S. D. M. White, P. A. Thomas, H. M. P. Couchman, J. A. Peacock, G. Efstathiou, and . V. Consortium), A Simulation of Galaxy Formation and Clustering, *ApJ*. **521**, L99–L102 (Aug., 1999). doi: 10.1086/312196.
- [19] R. Davé et al., Baryons in the Warm-Hot Intergalactic Medium, *ApJ*. **552**, 473–483 (May, 2001).
- [20] C. Murali, N. Katz, L. Hernquist, D. H. Weinberg, and R. Davé, The Growth of Galaxies in Cosmological Simulations of Structure Formation, *ApJ*. **571**, 1–14 (May, 2002). doi: 10.1086/339876.
- [21] V. Springel and L. Hernquist, The history of star formation in a  $\Lambda$  cold dark matter universe, *MNRAS*. **339**, 312–334 (Feb., 2003). doi: 10.1046/j.1365-8711.2003.06207.x.
- [22] S. Borgani et al., X-ray properties of galaxy clusters and groups from a cosmological hydrodynamical simulation, *MNRAS*. **348**, 1078–1096 (Mar., 2004). doi: 10.1111/j.1365-2966.2004.07431.x.
- [23] S. T. Kay, P. A. Thomas, A. Jenkins, and F. R. Pearce, Cosmological simulations of the intracluster medium, *MNRAS*. **355**, 1091–1104 (Dec., 2004). doi: 10.1111/j.1365-2966.2004.08383.x.
- [24] K. Dolag, F. K. Hansen, M. Roncarelli, and L. Moscardini, The imprints of local superclusters on the Sunyaev-Zel'dovich signals and their detectability with Planck, *MNRAS*. **363**, 29–39 (Oct., 2005). doi: 10.1111/j.1365-2966.2005.09452.x.

- [25] B. D. Oppenheimer and R. Davé, Mass, metal, and energy feedback in cosmological simulations, *MNRAS*. **387**, 577–600 (June, 2008). doi: 10.1111/j.1365-2966.2008.13280.x.
- [26] S. Planelles and V. Quilis, Galaxy cluster mergers, *MNRAS*. **399**, 410–424 (Oct., 2009). doi: 10.1111/j.1365-2966.2009.15290.x.
- [27] C. De Boni, K. Dolag, S. Ettori, L. Moscardini, V. Pettorino, and C. Baccigalupi, Hydrodynamical simulations of galaxy clusters in dark energy cosmologies - I. General properties, *MNRAS*. **415**, 2758–2772 (Aug., 2011). doi: 10.1111/j.1365-2966.2011.18894.x.
- [28] R. Davé, B. D. Oppenheimer, and K. Finlator, Galaxy evolution in cosmological simulations with outflows - I. Stellar masses and star formation rates, *MNRAS*. **415**, 11–31 (July, 2011). doi: 10.1111/j.1365-2966.2011.18680.x.
- [29] M. Vogelsberger, D. Sijacki, D. Kereš, V. Springel, and L. Hernquist, Moving mesh cosmology: numerical techniques and global statistics, *MNRAS*. **425**, 3024–3057 (Oct., 2012). doi: 10.1111/j.1365-2966.2012.21590.x.
- [30] W. Cui, S. Borgani, K. Dolag, G. Murante, and L. Tornatore, The effects of baryons on the halo mass function, *MNRAS*. **423**, 2279–2287 (July, 2012). doi: 10.1111/j.1365-2966.2012.21037.x.
- [31] R. Davé, N. Katz, B. D. Oppenheimer, J. A. Kollmeier, and D. H. Weinberg, The neutral hydrogen content of galaxies in cosmological hydrodynamic simulations, *MNRAS*. **434**, 2645–2663 (Sept., 2013). doi: 10.1093/mnras/stt1274.
- [32] T. Di Matteo, J. Colberg, V. Springel, L. Hernquist, and D. Sijacki, Direct Cosmological Simulations of the Growth of Black Holes and Galaxies, *ApJ*. 676:33-53 (Mar., 2008). doi: 10.1086/524921.
- [33] J. Schaye, C. Dalla Vecchia, C. M. Booth, R. P. C. Wiersma, T. Theuns, M. R. Haas, S. Bertone, A. R. Duffy, I. G. McCarthy, and F. van de Voort, The physics driving the cosmic star formation history, *MNRAS*. **402**, 1536–1560 (Mar., 2010). doi: 10.1111/j.1365-2966.2009.16029.x.
- [34] E. Puchwein and V. Springel, Shaping the galaxy stellar mass function with supernova- and AGN-driven winds, *MNRAS*. **428**, 2966–2979 (Feb., 2013). doi: 10.1093/mnras/sts243.
- [35] M. Hirschmann, K. Dolag, A. Saro, L. Bachmann, S. Borgani, and A. Burkert, Cosmological simulations of black hole growth: AGN luminosities and downsizing, *MNRAS*. **442**, 2304–2324 (Aug., 2014). doi: 10.1093/mnras/stu1023.
- [36] Y. Dubois, C. Pichon, C. Welker, D. Le Borgne, J. Devriendt, C. Laigle, S. Codis, D. Pogosyan, S. Arnouts, K. Benabed, E. Bertin, J. Blaizot, F. Bouchet, J.-F. Cardoso, S. Colombi, V. de Lapparent, V. Desjacques, R. Gavazzi, S. Kassin, T. Kimm, H. McCracken, B. Milliard, S. Peirani, S. Prunet, S. Rouberol, J. Silk, A. Slyz, T. Sousbie, R. Teyssier, L. Tresse, M. Treyer, D. Vibert, and M. Volonteri, Dancing in the dark: galactic properties trace spin swings along the cosmic web, *MNRAS*. **444**, 1453–1468, (2014).
- [37] M. P. van Daalen, J. Schaye, I. G. McCarthy, C. M. Booth, and C. Dalla Vecchia, The impact of baryonic processes on the two-point correlation functions of galaxies, subhaloes and matter, *MNRAS*. **440**, 2997–3010 (June, 2014). doi: 10.1093/mnras/stu482.
- [38] A. Saro, J. Liu, J. J. Mohr, K. A. Aird, M. L. N. Ashby, M. Bayliss, B. A. Benson, L. E. Bleem, S. Bocquet, M. Brodwin, J. E. Carlstrom, C. L. Chang, I. Chiu, H. M. Cho, A. Clocchiatti, T. M. Crawford, A. T. Crites, T. de Haan, S. Desai, J. P. Dietrich, M. A. Dobbs, K. Dolag, J. P. Dudley, R. J. Foley, D. Gangkofner, E. M.

- George, M. D. Gladders, A. H. Gonzalez, N. W. Halverson, C. Hennig, J. Hlavacek-Larrondo, W. L. Holzapfel, J. D. Hrubes, C. Jones, R. Keisler, A. T. Lee, E. M. Leitch, M. Lueker, D. Luong-Van, A. Mantz, D. P. Marrone, M. McDonald, J. J. McMahon, J. Mehl, S. S. Meyer, L. Mocanu, T. E. Montroy, S. S. Murray, D. Nurgaliev, S. Padin, A. Patej, C. Pryke, C. L. Reichardt, A. Rest, J. Ruel, J. E. Ruhl, B. R. Saliwanchik, J. T. Sayre, K. K. Schaffer, E. Shirokoff, H. G. Spieler, B. Stalder, Z. Staniszewski, A. A. Stark, K. Story, A. van Engelen, K. Vanderlinde, J. D. Vieira, A. Vikhlinin, R. Williamson, O. Zahn, and A. Zenteno, Constraints on the CMB temperature evolution using multiband measurements of the Sunyaev-Zel'dovich effect with the South Pole Telescope, *MNRAS*. **440**, 2610–2615 (May, 2014). doi: 10.1093/mnras/stu575.
- [39] N. Khandai, T. Di Matteo, R. Croft, S. Wilkins, Y. Feng, E. Tucker, C. DeGraf, and M.-S. Liu, The MassiveBlack-II simulation: the evolution of haloes and galaxies to  $z=0$ , *MNRAS*. **450**, 1349–1374 (June, 2015). doi: 10.1093/mnras/stv627.
- [40] M. Vogelsberger, S. Genel, V. Springel, P. Torrey, D. Sijacki, D. Xu, G. Snyder, D. Nelson, and L. Hernquist, Introducing the Illustris Project: simulating the coevolution of dark and visible matter in the Universe, *MNRAS*. **444**, 1518–1547 (Oct., 2014). doi: 10.1093/mnras/stu1536.
- [41] J. Schaye, R. A. Crain, R. G. Bower, M. Furlong, M. Schaller, T. Theuns, C. Dalla Vecchia, C. S. Frenk, I. G. McCarthy, J. C. Helly, A. Jenkins, Y. M. Rosas-Guevara, S. D. M. White, M. Baes, C. M. Booth, P. Camps, J. F. Navarro, Y. Qu, A. Rahmati, T. Sawala, P. A. Thomas, and J. Trayford, The EAGLE project: simulating the evolution and assembly of galaxies and their environments, *MNRAS*. **446**(1), 521–554 (Jan., 2015). doi: 10.1093/mnras/stu2058.
- [42] A. Ragagnin, K. Dolag, V. Biffi, M. Cadolle Bel, N. J. Hammer, A. Krukau, M. Petkova, and D. Steinborn, An online theoretical virtual observatory for hydrodynamical, cosmological simulations, *ArXiv e-prints* (Dec. 2016).
- [43] D. Nelson, A. Pillepich, V. Springel, R. Pakmor, R. Weinberger, S. Genel, P. Torrey, M. Vogelsberger, F. Marinacci, and L. Hernquist, First results from the TNG50 simulation: galactic outflows driven by supernovae and black hole feedback, *MNRAS*. **490**(3), 3234–3261 (Dec., 2019). doi: 10.1093/mnras/stz2306.
- [44] R. Davé, D. Anglés-Alcázar, D. Narayanan, Q. Li, M. H. Rafieferantsoa, and S. Appleby, SIMBA: Cosmological simulations with black hole growth and feedback, *MNRAS*. **486**, 2827–2849 (June, 2019). doi: 10.1093/mnras/stz937.
- [45] R. Pakmor, V. Springel, J. P. Coles, T. Guillet, C. Pfrommer, S. Bose, M. Barrera, A. M. Delgado, F. Ferlito, C. Frenk, B. Hadzhiyska, C. Hernández-Aguayo, L. Hernquist, R. Kannan, and S. D. M. White, The MillenniumTNG Project: the hydrodynamical full physics simulation and a first look at its galaxy clusters, *MNRAS*. **524**(2), 2539–2555 (Sept., 2023). doi: 10.1093/mnras/stac3620.
- [46] K. Dolag, J. G. Sorce, S. Pilipenko, E. Hernández-Martínez, M. Valentini, S. Gottlöber, N. Aghanim, and I. Khabibullin, Simulating the Local Web (SLOW): I. Anomalies in the local density field, *arXiv e-prints*. art. arXiv:2302.10960 (Feb., 2023). doi: 10.48550/arXiv.2302.10960.
- [47] D. J. Price, Smoothed particle hydrodynamics and magnetohydrodynamics, *Journal of Computational Physics*. **231**, 759–794 (Feb., 2012). doi: 10.1016/j.jcp.2010.12.011.
- [48] R. Teyssier, Grid-Based Hydrodynamics in Astrophysical Fluid Flows, *ARA&A*. **53**, 325–364 (Aug., 2015). doi: 10.1146/annurev-astro-082214-122309.
- [49] V. Springel, High performance computing and numerical modelling, *ArXiv e-prints* (Dec. 2014).

- [50] P. J. E. Peebles, *Principles of Physical Cosmology*. (Princeton University Press, 9 2020). ISBN 978-0-691-20981-4.
- [51] R. Cen, A hydrodynamic approach to cosmology - Methodology, *ApJS*. **78**, 341–364 (Feb., 1992). doi: 10.1086/191630.
- [52] P. Colella and H. M. Glaz, Efficient solution algorithms for the Riemann problem for real gases, *Journal of Computational Physics*. **59**, 264–289 (June, 1985).
- [53] P. Colella and P. R. Woodward, The Piecewise Parabolic Method (PPM) for Gas-Dynamical Simulations, *Journal of Computational Physics*. **54**, 174–201 (Sept., 1984).
- [54] A. Harten, B. Engquist, S. Osher, and S. R. Chakravarthy, Uniformly High Order Accurate Essentially Non-oscillatory Schemes III, *Journal of Computational Physics*. **71**, 231–303 (Aug., 1987).
- [55] D. Levy, G. Puppo, and G. Russo, Compact Central WENO Schemes for Multidimensional Conservation Laws, *ArXiv Mathematics e-prints* (Nov. 1999).
- [56] C.-W. Shu. Essentially Non-Oscillatory and Weighted Essentially Non-Oscillatory Schemes for Hyperbolic Conservation Laws. In *Advanced Numerical Approximate of Nonlinear Hyperbolic Equations. Lecture notes in Mathematics 1697, 1997 C.I.M.E. course in Cetraro, Italy, June 1997 (A. Quarteroni ed.)*, p. 285. Springer Verlag, (1998).
- [57] A. Harten, High Resolution Schemes for Hyperbolic Conservation Laws, *Journal of Computational Physics*. **49**, 357–393 (Mar., 1983).
- [58] R. Courant and K. O. Friedrichs, *Supersonic flow and shock waves*. (Pure and Applied Mathematics, New York: Interscience, 1948, 1948).
- [59] K. G. Powell, P. L. Roe, T. J. Linde, T. I. Gombosi, and D. L. de Zeeuw, A Solution-Adaptive Upwind Scheme for Ideal Magnetohydrodynamics, *Journal of Computational Physics*. **154**, 284–309 (Sept., 1999).
- [60] A. Harten, P. D. Lax, and B. van Leer, On upstream differencing and Godunov-type schemes for hyperbolic conservation laws. **25**(1), 35–61 (Jan., 1983). ISSN 0036-1445 (print), 1095-7200 (electronic).
- [61] B. Einfeldt, On Godunov-type methods for gas dynamics. **25**(2), 294–318 (Apr., 1988). ISSN 0036-1429 (print), 1095-7170 (electronic).
- [62] B. Einfeldt, P. L. Roe, C. D. Munz, and B. Sjogreen, On Godunov-type methods near low densities, *Journal of Computational Physics*. **92**, 273–295 (Feb., 1991).
- [63] S. Li, An HLLC Riemann solver for magneto-hydrodynamics, *Journal of Computational Physics*. **203**, 344–357 (Feb., 2005). doi: 10.1016/j.jcp.2004.08.020.
- [64] R. LeVeque, *Finite volume methods for hyperbolic problems*. Cambridge Texts in applied mathematics, (Cambridge University Press, 2002).
- [65] D. Ryu, J. P. Ostriker, H. Kang, and R. Cen, A cosmological hydrodynamic code based on the total variation diminishing scheme, *ApJ*. **414**, 1–19 (Sept., 1993). doi: 10.1086/173051.
- [66] S. Li, H. Li, and R. Cen, CosmoMHD: A Cosmological Magnetohydrodynamics Code, *ArXiv Astrophysics e-prints* (Nov. 2006).
- [67] A. V. Kravtsov, A. A. Klypin, and A. M. Khokhlov, Adaptive Refinement Tree: A New High-Resolution N-Body Code for Cosmological Simulations, *ApJS*. **111**, 73–+ (July, 1997). doi: 10.1086/313015.
- [68] A. Kravtsov, Adaptive Mesh Refinement Simulations of Cluster Formation, *APS Meeting Abstracts* (Apr. 2002).
- [69] R. Teyssier, Cosmological hydrodynamics with adaptive mesh refinement. A new high resolution code called RAMSES, *A&A*. **385**, 337–364 (Apr., 2002). doi: 10.1051/0004-6361:20011817.

- [70] J. M. Stone and M. L. Norman, ZEUS-2D: A radiation magnetohydrodynamics code for astrophysical flows in two space dimensions. I - The hydrodynamic algorithms and tests., *ApJS*. **80**, 753–790 (June, 1992). doi: 10.1086/191680.
- [71] G. L. Bryan, M. L. Norman, J. M. Stone, R. Cen, and J. P. Ostriker, A piecewise parabolic method for cosmological hydrodynamics., *Computer Physics Communications*. **89**, 149–168 (Aug., 1995).
- [72] P. M. Ricker, S. Dodelson, and D. Q. Lamb, COSMOS: A Hybrid N-Body/Hydrodynamics Code for Cosmological Problems, *ApJ*. **536**, 122–143 (June, 2000). doi: 10.1086/308908.
- [73] B. Fryxell, K. Olson, P. Ricker, F. X. Timmes, M. Zingale, D. Q. Lamb, P. MacNeice, R. Rosner, J. W. Truran, and H. Tufo, FLASH: An Adaptive Mesh Hydrodynamics Code for Modeling Astrophysical Thermonuclear Flashes, *ApJS*. **131**, 273–334 (Nov., 2000). doi: 10.1086/317361.
- [74] L.-L. Feng, C.-W. Shu, and M. Zhang, A Hybrid Cosmological Hydrodynamic/N-Body Code Based on a Weighted Essentially Nonoscillatory Scheme, *ApJ*. **612**, 1–13 (Sept., 2004). doi: 10.1086/422513.
- [75] F. Vazza, G. Brunetti, C. Gheller, and R. Brunino, Massive and refined: A sample of large galaxy clusters simulated at high resolution. I: Thermal gas and properties of shock waves, *New A*. **15**, 695–711 (Nov., 2010). doi: 10.1016/j.newast.2010.05.003.
- [76] S. Paul, L. Iapichino, F. Miniati, J. Bagchi, and K. Mannheim, Evolution of Shocks and Turbulence in Major Cluster Mergers, *ApJ*. **726**:17 (Jan., 2011). doi: 10.1088/0004-637X/726/1/17.
- [77] L. Iapichino, W. Schmidt, J. C. Niemeyer, and J. Merklein, Turbulence production and turbulent pressure support in the intergalactic medium, *MNRAS*. **414**, 2297–2308 (July, 2011). doi: 10.1111/j.1365-2966.2011.18550.x.
- [78] R. A. Gingold and J. J. Monaghan, Smoothed particle hydrodynamics - Theory and application to non-spherical stars, *MNRAS*. **181**, 375–389 (Nov., 1977).
- [79] L. B. Lucy, A numerical approach to the testing of the fission hypothesis, *AJ*. **82**, 1013–1024 (Dec., 1977).
- [80] J. I. Read, T. Hayfield, and O. Agertz, Resolving mixing in smoothed particle hydrodynamics, *MNRAS*. **405**, 1513–1530 (July, 2010). doi: 10.1111/j.1365-2966.2010.16577.x.
- [81] W. Dehnen and H. Aly, Improving convergence in smoothed particle hydrodynamics simulations without pairing instability, *MNRAS*. **425**, 1068–1082 (Sept., 2012). doi: 10.1111/j.1365-2966.2012.21439.x.
- [82] S. Rosswog, SPH Methods in the Modelling of Compact Objects, *Living Reviews in Computational Astrophysics*. **1**:1 (Dec., 2015). doi: 10.1007/lrca-2015-1.
- [83] V. Springel and L. Hernquist, Cosmological smoothed particle hydrodynamics simulations: the entropy equation, *MNRAS*. **333**, 649–664 (July, 2002).
- [84] P. F. Hopkins, A general class of Lagrangian smoothed particle hydrodynamics methods and implications for fluid mixing problems, *MNRAS*. **428**, 2840–2856 (Feb., 2013). doi: 10.1093/mnras/sts210.
- [85] T. R. Saitoh and J. Makino, A Density-independent Formulation of Smoothed Particle Hydrodynamics, *ApJ*. **768**:44 (May, 2013). doi: 10.1088/0004-637X/768/1/44.
- [86] J. J. Monaghan and R. A. Gingold, Shock simulation by the particle method SPH, *Journal of Computational Physics*. **52**, 374–389 (Nov., 1983).
- [87] D. S. Balsara, von Neumann stability analysis of smooth particle hydrodynamics—suggestions for optimal algorithms, *Journal of Computational Physics*. **121**, 357–372, (1995).

- [88] M. Steinmetz, Mergers and Formation of Disk Galaxies in Hierarchically Clustering Universes. In *IAU Symp. 171: New Light on Galaxy Evolution*, p. 259, (1996).
- [89] J. J. Monaghan, SPH and Riemann Solvers, *Journal of Computational Physics*. **136**, 298–307 (Sept., 1997).
- [90] J. P. Morris and J. J. Monaghan, A Switch to Reduce SPHnext term Viscosity, *Journal of Computational Physics*. **136**, 41–50 (Sept., 1997).
- [91] K. Dolag, F. Vazza, G. Brunetti, and G. Tormen, Turbulent gas motions in galaxy cluster simulations: the role of smoothed particle hydrodynamics viscosity, *MNRAS*. **364**, 753–772 (Dec., 2005). doi: 10.1111/j.1365-2966.2005.09630.x.
- [92] L. Cullen and W. Dehnen, Inviscid smoothed particle hydrodynamics, *MNRAS*. **408**, 669–683 (Oct., 2010). doi: 10.1111/j.1365-2966.2010.17158.x.
- [93] J. I. Read and T. Hayfield, SPHS: smoothed particle hydrodynamics with a higher order dissipation switch, *MNRAS*. **422**, 3037–3055 (June, 2012). doi: 10.1111/j.1365-2966.2012.20819.x.
- [94] D. J. Price, Resolving high Reynolds numbers in smoothed particle hydrodynamics simulations of subsonic turbulence, *MNRAS*. **420**, L33–L37 (Feb., 2012). doi: 10.1111/j.1745-3933.2011.01187.x.
- [95] C.-Y. Hu, T. Naab, S. Walch, B. P. Moster, and L. Oser, SPHGal: smoothed particle hydrodynamics with improved accuracy for galaxy simulations, *MNRAS*. **443**(2), 1173–1191 (Sept., 2014). doi: 10.1093/mnras/stu1187.
- [96] A. M. Beck, G. Murante, A. Arth, R.-S. Remus, A. F. Teklu, J. M. F. Donnert, S. Planelles, M. C. Beck, P. Förster, M. Imgrund, K. Dolag, and S. Borgani, An improved SPH scheme for cosmological simulations, *MNRAS*. **455**, 2110–2130 (Jan., 2016). doi: 10.1093/mnras/stv2443.
- [97] S.-I. Inutsuka, Reformulation of Smoothed Particle Hydrodynamics with Riemann Solver, *Journal of Computational Physics*. **179**, 238–267 (June, 2002). doi: 10.1006/jcph.2002.7053.
- [98] S.-H. Cha and A. P. Whitworth, Implementations and tests of Godunov-type particle hydrodynamics, *MNRAS*. **340**, 73–90 (Mar., 2003). doi: 10.1046/j.1365-8711.2003.06266.x.
- [99] S.-H. Cha, S.-I. Inutsuka, and S. Nayakshin, Kelvin-Helmholtz instabilities with Godunov smoothed particle hydrodynamics, *MNRAS*. **403**, 1165–1174 (Apr., 2010). doi: 10.1111/j.1365-2966.2010.16200.x.
- [100] G. Murante, S. Borgani, R. Brunino, and S.-H. Cha, Hydrodynamic simulations with the Godunov smoothed particle hydrodynamics, *MNRAS*. **417**, 136–153 (Oct., 2011). doi: 10.1111/j.1365-2966.2011.19021.x.
- [101] U.-L. Pen, A High-Resolution Adaptive Moving Mesh Hydrodynamic Algorithm, *ApJS*. **115**, 19–+ (Mar., 1998). doi: 10.1086/313074.
- [102] E. Gaburov and K. Nitadori, Astrophysical weighted particle magnetohydrodynamics, *MNRAS*. **414**, 129–154 (June, 2011). doi: 10.1111/j.1365-2966.2011.18313.x.
- [103] V. Springel, E pur si muove: Galilean-invariant cosmological hydrodynamical simulations on a moving mesh, *MNRAS*. **401**, 791–851 (Jan., 2010). doi: 10.1111/j.1365-2966.2009.15715.x.
- [104] P. F. Hopkins, A new class of accurate, mesh-free hydrodynamic simulation methods, *MNRAS*. **450**, 53–110 (June, 2015). doi: 10.1093/mnras/stv195.
- [105] F. Groth, U. P. Steinwandel, M. Valentini, and K. Dolag, The cosmological simulation code OPENGADGET3 - implementation of meshless finite mass, *MNRAS*. **526** (1), 616–644 (Nov., 2023). doi: 10.1093/mnras/stad2717.
- [106] J.-P. Vila, *Mathematical Models and Methods in Applied Science*. **9**, 161–, (1999).
- [107] N. Lanson and J.-P. Vila, *SIAM J. Numer. Anal.* **46**, 1912–, (2008).

- [108] N. Lanson and J.-P. Vila, *SIAM J. Numer. Anal.* **46**, 1935–, (2008).
- [109] O. Agertz, B. Moore, J. Stadel, D. Potter, F. Miniati, J. Read, L. Mayer, A. Gawryszczak, A. Kravtsov, Å. Nordlund, F. Pearce, V. Quilis, D. Rudd, V. Springel, J. Stone, E. Tasker, R. Teyssier, J. Wadsley, and R. Walder, Fundamental differences between SPH and grid methods, *MNRAS*. **380**, 963–978 (Sept., 2007). doi: 10.1111/j.1365-2966.2007.12183.x.
- [110] B. W. O’Shea, K. Nagamine, V. Springel, L. Hernquist, and M. L. Norman, Comparing AMR and SPH Cosmological Simulations. I. Dark Matter and Adiabatic Simulations, *ApJS*. **160**, 1–27 (Sept., 2005). doi: 10.1086/432645.
- [111] H. Kang, J. P. Ostriker, R. Cen, D. Ryu, L. Hernquist, A. E. Evrard, G. L. Bryan, and M. L. Norman, A comparison of cosmological hydrodynamic codes, *ApJ*. **430**, 83–100 (July, 1994). doi: 10.1086/174384.
- [112] C. S. Frenk, S. D. M. White, P. Bode, J. R. Bond, G. L. Bryan, R. Cen, H. M. P. Couchman, A. E. Evrard, N. Gnedin, A. Jenkins, A. M. Khokhlov, A. Klypin, J. F. Navarro, M. L. Norman, J. P. Ostriker, J. M. Owen, F. R. Pearce, U.-L. Pen, M. Steinmetz, P. A. Thomas, J. V. Villumsen, J. W. Wadsley, M. S. Warren, G. Xu, and G. Yepes, The Santa Barbara Cluster Comparison Project: A Comparison of Cosmological Hydrodynamics Solutions, *ApJ*. **525**, 554–582 (Nov., 1999). doi: 10.1086/307908.
- [113] F. Sembolini, G. Yepes, F. R. Pearce, A. Knebe, S. T. Kay, C. Power, W. Cui, A. M. Beck, S. Borgani, C. Dalla Vecchia, R. Davé, P. J. Elahi, S. February, S. Huang, A. Hobbs, N. Katz, E. Lau, I. G. McCarthy, G. Murante, D. Nagai, K. Nelson, R. D. A. Newton, V. Perret, E. Puchwein, J. I. Read, A. Saro, J. Schaye, R. Teyssier, and R. J. Thacker, nIFTy galaxy cluster simulations - I. Dark matter and non-radiative models, *MNRAS*. **457**, 4063–4080 (Apr., 2016). doi: 10.1093/mnras/stw250.
- [114] C. Scannapieco, M. Wadepuhl, O. H. Parry, J. F. Navarro, A. Jenkins, V. Springel, R. Teyssier, E. Carlson, H. M. P. Couchman, R. A. Crain, C. Dalla Vecchia, C. S. Frenk, C. Kobayashi, P. Monaco, G. Murante, T. Okamoto, T. Quinn, J. Schaye, G. S. Stinson, T. Theuns, J. Wadsley, S. D. M. White, and R. Woods, The Aquila comparison project: the effects of feedback and numerical methods on simulations of galaxy formation, *MNRAS*. **423**, 1726–1749 (June, 2012). doi: 10.1111/j.1365-2966.2012.20993.x.
- [115] S. Roca-Fàbrega, J.-H. Kim, L. Hausammann, K. Nagamine, A. Lupi, J. W. Powell, I. Shimizu, D. Ceverino, J. R. Primack, T. R. Quinn, Y. Revaz, H. Velázquez, T. Abel, M. Buehlmann, A. Dekel, B. Dong, O. Hahn, C. Hummels, K.-W. Kim, B. D. Smith, C. Strawn, R. Teyssier, M. J. Turk, and AGORA Collaboration, The AGORA High-resolution Galaxy Simulations Comparison Project. III. Cosmological Zoom-in Simulation of a Milky Way-mass Halo, *ApJ*. 917(2):64 (Aug., 2021). doi: 10.3847/1538-4357/ac088a.
- [116] F. Sembolini, P. J. Elahi, F. R. Pearce, C. Power, A. Knebe, S. T. Kay, W. Cui, G. Yepes, A. M. Beck, S. Borgani, D. Cunnama, R. Davé, S. February, S. Huang, N. Katz, I. G. McCarthy, G. Murante, R. D. A. Newton, V. Perret, E. Puchwein, A. Saro, J. Schaye, and R. Teyssier, nIFTy galaxy cluster simulations - II. Radiative models, *MNRAS*. **459**, 2973–2991 (July, 2016). doi: 10.1093/mnras/stw800.
- [117] J.-h. Kim, T. Abel, O. Agertz, G. L. Bryan, D. Ceverino, C. Christensen, C. Conroy, A. Dekel, N. Y. Gnedin, N. J. Goldbaum, J. Guedes, O. Hahn, A. Hobbs, P. F. Hopkins, C. B. Hummels, F. Iannuzzi, D. Keres, A. Klypin, A. V. Kravtsov, M. R. Krumholz, M. Kuhlen, S. N. Leitner, P. Madau, L. Mayer, C. E. Moody, K. Nagamine, M. L. Norman, J. Onorbe, B. W. O’Shea, A. Pillepich, J. R. Primack,

- T. Quinn, J. I. Read, B. E. Robertson, M. Rocha, D. H. Rudd, S. Shen, B. D. Smith, A. S. Szalay, R. Teyssier, R. Thompson, K. Todoroki, M. J. Turk, J. W. Wadsley, J. H. Wise, A. Zolotov, and t. AGORA Collaboration<sup>29</sup>, The AGORA High-resolution Galaxy Simulations Comparison Project, *ApJS*. 210(1):14 (Jan., 2014). doi: 10.1088/0067-0049/210/1/14.
- [118] F. Haardt and P. Madau, Radiative Transfer in a Clumpy Universe. II. The Ultraviolet Extragalactic Background, *ApJ*. **461**, 20–+ (Apr., 1996). doi: 10.1086/177035.
- [119] F. Haardt and P. Madau, Radiative Transfer in a Clumpy Universe. IV. New Synthesis Models of the Cosmic UV/X-Ray Background, *ApJ*. 746(2):125 (Feb., 2012). doi: 10.1088/0004-637X/746/2/125.
- [120] E. Puchwein, F. Haardt, M. G. Haehnelt, and P. Madau, Consistent modelling of the meta-galactic UV background and the thermal/ionization history of the intergalactic medium, *MNRAS*. **485**(1), 47–68 (May, 2019). doi: 10.1093/mnras/stz222.
- [121] C.-A. Faucher-Giguère, A cosmic UV/X-ray background model update, *MNRAS*. **493**(2), 1614–1632 (Apr., 2020). doi: 10.1093/mnras/staa302.
- [122] U. Maio, K. Dolag, B. Ciardi, and L. Tornatore, Metal and molecule cooling in simulations of structure formation, *MNRAS*. **379**(3), 963–973 (Aug., 2007). doi: 10.1111/j.1365-2966.2007.12016.x.
- [123] R. S. Sutherland and M. A. Dopita, Cooling functions for low-density astrophysical plasmas, *ApJS*. **88**, 253–327 (Sept., 1993). doi: 10.1086/191823.
- [124] G. J. Ferland, K. T. Korista, D. A. Verner, J. W. Ferguson, J. B. Kingdon, and E. M. Verner, CLOUDY 90: Numerical Simulation of Plasmas and Their Spectra, *PASP*. **110**, 761–778 (July, 1998).
- [125] T. Abel, P. Anninos, Y. Zhang, and M. L. Norman, Modeling primordial gas in numerical cosmology, *New Astronomy*. **2**, 181–207 (Aug., 1997). doi: 10.1016/S1384-1076(97)00010-9.
- [126] D. Galli and F. Palla, The chemistry of the early Universe, *A&A*. **335**, 403–420 (July, 1998).
- [127] C. F. McKee and E. C. Ostriker, Theory of Star Formation, *ARA&A*. **45**(1), 565–687 (Sept., 2007). doi: 10.1146/annurev.astro.45.051806.110602.
- [128] R. C. Kennicutt and N. J. Evans, Star Formation in the Milky Way and Nearby Galaxies, *ARA&A*. **50**, 531–608 (Sept., 2012). doi: 10.1146/annurev-astro-081811-125610.
- [129] P. Madau and M. Dickinson, Cosmic Star-Formation History, *ARA&A*. **52**, 415–486 (Aug., 2014). doi: 10.1146/annurev-astro-081811-125615.
- [130] L. J. Tacconi, R. Genzel, and A. Sternberg, The Evolution of the Star-Forming Interstellar Medium Across Cosmic Time, *ARA&A*. **58**, 157–203 (Aug., 2020). doi: 10.1146/annurev-astro-082812-141034.
- [131] V. Springel and L. Hernquist, Cosmological smoothed particle hydrodynamics simulations: a hybrid multiphase model for star formation, *MNRAS*. **339**(2), 289–311 (Feb., 2003). ISSN 0035-8711. doi: 10.1046/j.1365-8711.2003.06206.x. URL <http://mnras.oxfordjournals.org/cgi/doi/10.1046/j.1365-8711.2003.06206.x>.
- [132] M. Schmidt, The Rate of Star Formation., *ApJ*. **129**, 243 (Mar., 1959). doi: 10.1086/146614.
- [133] J. Kennicutt, Robert C., The Star Formation Law in Galactic Disks, *ApJ*. **344**, 685 (Sept., 1989). doi: 10.1086/167834.
- [134] J. Schaye, Star Formation Thresholds and Galaxy Edges: Why and Where, *ApJ*. **609**(2), 667–682 (July, 2004). doi: 10.1086/421232.
- [135] M. Valentini, G. Murante, S. Borgani, P. Monaco, A. Bressan, and A. M. Beck, On the effect of galactic outflows in cosmological simulations of disc galaxies, *MNRAS*.

- 470**, 3167–3193, (2017).
- [136] F. Marinacci, L. V. Sales, M. Vogelsberger, P. Torrey, and V. Springel, Simulating the interstellar medium and stellar feedback on a moving mesh: implementation and isolated galaxies, *MNRAS*. **489**(3), 4233–4260 (Nov., 2019). doi: 10.1093/mnras/stz2391.
- [137] L. Wang, A. A. Dutton, G. S. Stinson, A. V. Macciò, C. Penzo, X. Kang, B. W. Keller, and J. Wadsley, NIHAO project - I. Reproducing the inefficiency of galaxy formation across cosmic time with a large sample of cosmological hydrodynamical simulations, *MNRAS*. **454**(1), 83–94 (Nov., 2015). doi: 10.1093/mnras/stv1937.
- [138] K. Dolag. The Magneticum Simulations, from Galaxies to Galaxy Clusters. In *IAU General Assembly*, vol. 29, p. 2250156 (Aug., 2015).
- [139] A. Pillepich, V. Springel, D. Nelson, S. Genel, J. Naiman, R. Pakmor, L. Hernquist, P. Torrey, M. Vogelsberger, R. Weinberger, and F. Marinacci, Simulating galaxy formation with the IllustrisTNG model, *MNRAS*. **473**, 4077–4106 (Jan., 2018). doi: 10.1093/mnras/stx2656.
- [140] N. A. Henden, E. Puchwein, S. Shen, and D. Sijacki, The FABLE simulations: a feedback model for galaxies, groups, and clusters, *MNRAS*. **479**(4), 5385–5412 (Oct., 2018). doi: 10.1093/mnras/sty1780.
- [141] Y. Dubois, S. Peirani, C. Pichon, J. Devriendt, R. Gavazzi, C. Welker, and M. Volonteri, The HORIZON-AGN simulation: morphological diversity of galaxies promoted by AGN feedback, *MNRAS*. **463**(4), 3948–3964 (Dec., 2016). doi: 10.1093/mnras/stw2265.
- [142] Y. Dubois, R. Beckmann, F. Bournaud, H. Choi, J. Devriendt, R. Jackson, S. Kaviraj, T. Kimm, K. Kraljic, C. Laigle, G. Martin, M.-J. Park, S. Peirani, C. Pichon, M. Volonteri, and S. K. Yi, Introducing the NEWHORIZON simulation: Galaxy properties with resolved internal dynamics across cosmic time, *A&A*. 651:A109 (July, 2021). doi: 10.1051/0004-6361/202039429.
- [143] C. Ragone-Figueroa, G. L. Granato, M. E. Ferraro, G. Murante, V. Biffi, S. Borgani, S. Planelles, and E. Rasia, BCG mass evolution in cosmological hydro-simulations, *MNRAS*. **479**(1), 1125–1136 (Sept., 2018). doi: 10.1093/mnras/sty1639.
- [144] L. Bassini, E. Rasia, S. Borgani, G. L. Granato, C. Ragone-Figueroa, V. Biffi, A. Ragagnin, K. Dolag, W. Lin, G. Murante, N. R. Napolitano, G. Taffoni, L. Tornatore, and Y. Wang, The DIANOGA simulations of galaxy clusters: characterising star formation in protoclusters, *A&A*. 642:A37 (Oct., 2020). doi: 10.1051/0004-6361/202038396.
- [145] K. Dolag, J. G. Sorce, S. Pilipenko, E. Hernández-Martínez, M. Valentini, S. Gottlöber, N. Aghanim, and I. Khabibullin, Simulating the LOcal Web (SLOW). I. Anomalies in the local density field, *A&A*. 677:A169 (Sept., 2023). doi: 10.1051/0004-6361/202346213.
- [146] M. R. Krumholz and N. Y. Gnedin, A Comparison of Methods for Determining the Molecular Content of Model Galaxies, *ApJ*. 729(1):36 (Mar., 2011). doi: 10.1088/0004-637X/729/1/36.
- [147] R. Davé, M. H. Rafieferantsoa, R. J. Thompson, and P. F. Hopkins, MUFASA: Galaxy star formation, gas, and metal properties across cosmic time, *MNRAS*. **467**(1), 115–132 (May, 2017). doi: 10.1093/mnras/stx108.
- [148] P. F. Hopkins, D. Kereš, J. Oñorbe, C.-A. Faucher-Giguère, E. Quataert, N. Murray, and J. S. Bullock, Galaxies on FIRE (Feedback In Realistic Environments): stellar feedback explains cosmologically inefficient star formation, *MNRAS*. **445**(1), 581–603 (Nov., 2014). doi: 10.1093/mnras/stu1738.

- [149] P. F. Hopkins, A. Wetzel, D. Keres, C.-A. Faucher-Giguere, E. Quataert, M. Boylan-Kolchin, N. Murray, C. C. Hayward, S. Garrison-Kimmel, C. Hummels, R. Feldmann, P. Torrey, X. Ma, D. Angles-Alcazar, K.-Y. Su, M. Orr, D. Schmitz, I. Escala, R. Sanderson, M. Y. Grudic, Z. Hafen, J.-H. Kim, A. Fitts, J. S. Bullock, C. Wheeler, T. K. Chan, O. D. Elbert, and D. Narayanan, FIRE-2 Simulations: Physics versus Numerics in Galaxy Formation, *ArXiv e-prints* (Feb. 2017).
- [150] R. Feldmann, E. Quataert, C.-A. Faucher-Giguère, P. F. Hopkins, O. Çatmabacak, D. Kereš, L. Bassini, M. Bernardini, J. S. Bullock, E. Cenci, J. Gensior, L. Liang, J. Moreno, and A. Wetzel, FIREbox: simulating galaxies at high dynamic range in a cosmological volume, *MNRAS*. **522**(3), 3831–3860 (July, 2023). doi: 10.1093/mnras/stad1205.
- [151] F. I. Pelupessy, P. P. Papadopoulos, and P. van der Werf, Incorporating the Molecular Gas Phase in Galaxy-sized Numerical Simulations: First Applications in Dwarf Galaxies, *ApJ*. **645**(2), 1024–1042 (July, 2006). doi: 10.1086/504366.
- [152] R. Feldmann, N. Y. Gnedin, and A. V. Kravtsov, How Universal is the  $\Sigma_{SFR} - \Sigma_{H_2}$  Relation?, *ApJ*. **732**(2):115 (May, 2011). doi: 10.1088/0004-637X/732/2/115.
- [153] C. Christensen, T. Quinn, F. Governato, A. Stilp, S. Shen, and J. Wadsley, Implementing molecular hydrogen in hydrodynamic simulations of galaxy formation, *MNRAS*. **425**(4), 3058–3076 (Oct., 2012). doi: 10.1111/j.1365-2966.2012.21628.x.
- [154] M. Kuhlen, M. R. Krumholz, P. Madau, B. D. Smith, and J. Wise, Dwarf Galaxy Formation with  $H_2$ -regulated Star Formation, *ApJ*. **749**(1):36 (Apr., 2012). doi: 10.1088/0004-637X/749/1/36.
- [155] G. Murante, P. Monaco, S. Borgani, L. Tornatore, K. Dolag, and D. Goz, Simulating realistic disc galaxies with a novel sub-resolution ISM model, *MNRAS*. **447**(1), 178–201 (Feb., 2015). doi: 10.1093/mnras/stu2400.
- [156] M. Tomassetti, C. Porciani, E. Romano-Díaz, and A. D. Ludlow, Simulating the  $H_2$  content of high-redshift galaxies, *MNRAS*. **446**(4), 3330–3345 (Feb., 2015). doi: 10.1093/mnras/stu2273.
- [157] A. Lupi, S. Bovino, P. R. Capelo, M. Volonteri, and J. Silk, The natural emergence of the correlation between  $H_2$  and star formation rate surface densities in galaxy simulations, *MNRAS*. **474**(3), 2884–2903 (Mar., 2018). doi: 10.1093/mnras/stx2874.
- [158] A. Pallottini, A. Ferrara, D. Decataldo, S. Gallerani, L. Vallini, S. Carniani, C. Behrens, M. Kohandel, and S. Salvadori, Deep into the structure of the first galaxies: SERRA views, *MNRAS*. **487**(2), 1689–1708 (Aug., 2019). doi: 10.1093/mnras/stz1383.
- [159] A. Schäbe, E. Romano-Díaz, C. Porciani, A. D. Ludlow, and M. Tomassetti, A comparison of  $H_2$  formation models at high redshift, *MNRAS*. **497**(4), 5008–5023 (Oct., 2020). doi: 10.1093/mnras/staa2313.
- [160] M. Valentini, K. Dolag, S. Borgani, G. Murante, U. Maio, L. Tornatore, G. L. Granato, C. Ragone-Figueroa, A. Burkert, A. Ragagnin, and E. Rasia, Impact of  $H_2$ -driven star formation and stellar feedback from low-enrichment environments on the formation of spiral galaxies, *MNRAS*. **518**(1), 1128–1147 (Jan., 2023). doi: 10.1093/mnras/stac2110.
- [161] J. Guedes, S. Callegari, P. Madau, and L. Mayer, Forming Realistic Late-type Spirals in a  $\Lambda$ CDM Universe: The Eris Simulation, *ApJ*. **742**(2):76 (Dec., 2011). doi: 10.1088/0004-637X/742/2/76.
- [162] T. Tamfal, L. Mayer, T. R. Quinn, A. Babul, P. Madau, P. R. Capelo, S. Shen, and M. Staub, The Dawn of Disk Formation in a Milky Way-sized Galaxy Halo: Thin Stellar Disks at  $z \lesssim 4$ , *ApJ*. **928**(2):106 (Apr., 2022). doi: 10.3847/1538-4357/ac558e.

- [163] G. Murante, P. Monaco, M. Giovalli, S. Borgani, and A. Diaferio, A subresolution multiphase interstellar medium model of star formation and supernova energy feedback, *MNRAS*. **405**, 1491–1512 (July, 2010). doi: 10.1111/j.1365-2966.2010.16567.x.
- [164] M. Valentini, S. Borgani, A. Bressan, G. Murante, L. Tornatore, and P. Monaco, Chemical evolution of disc galaxies from cosmological simulations, *MNRAS*. **485**(1), 1384–1404 (May, 2019). doi: 10.1093/mnras/stz492.
- [165] G. L. Granato, C. Ragone-Figueroa, A. Taverna, L. Silva, M. Valentini, S. Borgani, P. Monaco, G. Murante, and L. Tornatore, Dust evolution in zoom-in cosmological simulations of galaxy formation, *MNRAS*. **503**(1), 511–532 (May, 2021). doi: 10.1093/mnras/stab362.
- [166] M. Parente, C. Ragone-Figueroa, G. L. Granato, S. Borgani, G. Murante, M. Valentini, A. Bressan, and A. Lapi, Dust evolution with MUPPI in cosmological volumes, *MNRAS*. **515**(2), 2053–2071 (Sept., 2022). doi: 10.1093/mnras/stac1913.
- [167] L. Blitz and E. Rosolowsky, The Role of Pressure in GMC Formation II: The H<sub>2</sub>-Pressure Relation, *ApJ*. **650**(2), 933–944 (Oct., 2006). doi: 10.1086/505417.
- [168] M. R. Krumholz, C. F. McKee, and J. Tumlinson, The Star Formation Law in Atomic and Molecular Gas, *ApJ*. **699**(1), 850–856 (July, 2009). doi: 10.1088/0004-637X/699/1/850.
- [169] C. Ragone-Figueroa, G. L. Granato, M. Parente, G. Murante, M. Valentini, S. Borgani, and U. Maio, Intertwined Formation of H<sub>2</sub>, Dust, and Stars in Cosmological Simulations, *arXiv e-prints*. art. arXiv:2407.06269 (July, 2024). doi: 10.48550/arXiv.2407.06269.
- [170] P. F. Hopkins, D. Narayanan, and N. Murray, The meaning and consequences of star formation criteria in galaxy models with resolved stellar feedback, *MNRAS*. **432**(4), 2647–2653 (July, 2013). doi: 10.1093/mnras/stt723.
- [171] T. Buck, A. A. Dutton, and A. V. Macciò, An observational test for star formation prescriptions in cosmological hydrodynamical simulations, *MNRAS*. **486**(1), 1481–1487 (June, 2019). doi: 10.1093/mnras/stz969.
- [172] L. Tornatore, S. Borgani, K. Dolag, and F. Matteucci, Chemical enrichment of galaxy clusters from hydrodynamical simulations, *MNRAS*. **382**, 1050–1072 (Dec., 2007). doi: 10.1111/j.1365-2966.2007.12070.x.
- [173] B. D. Oppenheimer, J. Schaye, R. A. Crain, J. K. Werk, and A. J. Richings, The multiphase circumgalactic medium traced by low metal ions in EAGLE zoom simulations, *MNRAS*. **481**(1), 835–859 (Nov., 2018). doi: 10.1093/mnras/sty2281.
- [174] P. Torrey, M. Vogelsberger, L. Hernquist, R. McKinnon, F. Marinacci, R. A. Simcoe, V. Springel, A. Pillepich, J. Naiman, R. Pakmor, R. Weinberger, D. Nelson, and S. Genel, Similar star formation rate and metallicity variability time-scales drive the fundamental metallicity relation, *MNRAS*. **477**(1), L16–L20 (June, 2018). doi: 10.1093/mnrasl/sly031.
- [175] E. Rasia, S. Borgani, G. Murante, S. Planelles, A. M. Beck, V. Biffi, C. Ragone-Figueroa, G. L. Granato, L. K. Steinborn, and K. Dolag, Cool Core Clusters from Cosmological Simulations, *ApJL*. **813**, L17, (2015).
- [176] I. G. McCarthy, J. Schaye, S. Bird, and A. M. C. Le Brun, The BAHAMAS project: calibrated hydrodynamical simulations for large-scale structure cosmology, *MNRAS*. **465**, 2936–2965, (2017).
- [177] L. Oser, J. P. Ostriker, T. Naab, P. H. Johansson, and A. Burkert, The Two Phases of Galaxy Formation, *ApJ*. **725**, 2312–2323, (2010).
- [178] M. Aumer, S. D. M. White, T. Naab, and C. Scannapieco, Towards a more realistic population of bright spiral galaxies in cosmological simulations, *MNRAS*. **434**, 3142–3164, (2013).

- [179] G. S. Stinson, C. Brook, A. V. Macciò, J. Wadsley, T. R. Quinn, and H. M. P. Couchman, Making Galaxies In a Cosmological Context: the need for early stellar feedback, *MNRAS*. **428**(1), 129–140 (Jan., 2013). doi: 10.1093/mnras/sts028.
- [180] F. Marinacci, R. Pakmor, and V. Springel, The formation of disc galaxies in high-resolution moving-mesh cosmological simulations, *MNRAS*. **437**, 1750–1775, (2014).
- [181] P. F. Hopkins, A. Wetzel, D. Kereš, C.-A. Faucher-Giguère, E. Quataert, M. Boylan-Kolchin, N. Murray, C. C. Hayward, S. Garrison-Kimmel, C. Hummels, R. Feldmann, P. Torrey, X. Ma, D. Anglés-Alcázar, K.-Y. Su, M. Orr, D. Schmitz, I. Escala, R. Sanderson, M. Y. Grudić, Z. Hafen, J.-H. Kim, A. Fitts, J. S. Bullock, C. Wheeler, T. K. Chan, O. D. Elbert, and D. Narayanan, FIRE-2 Simulations: Physics versus Numerics in Galaxy Formation, *MNRAS*. (2018).
- [182] E. E. Salpeter, The Luminosity Function and Stellar Evolution., *ApJ*. **121**, 161, (1955).
- [183] N. Arimoto and Y. Yoshii, Chemical and photometric properties of a galactic wind model for elliptical galaxies., *A&A*. **173**, 23–38 (Feb., 1987).
- [184] P. Kroupa, C. A. Tout, and G. Gilmore, The distribution of low-mass stars in the Galactic disc, *MNRAS*. **262**, 545–587, (1993).
- [185] P. Kroupa, On the variation of the initial mass function, *MNRAS*. **322**, 231–246, (2001).
- [186] P. Kroupa, The Initial Mass Function of Stars: Evidence for Uniformity in Variable Systems, *Science*. **295**, 82–91, (2002).
- [187] G. Chabrier, Galactic Stellar and Substellar Initial Mass Function, *PASP*. **115**, 763–795, (2003).
- [188] S. Borgani, D. Fabjan, L. Tornatore, S. Schindler, K. Dolag, and A. Diaferio, The Chemical Enrichment of the ICM from Hydrodynamical Simulations, *Space Sci. Rev.* **134**, 379–403 (Feb., 2008). doi: 10.1007/s11214-008-9322-7.
- [189] C. G. Few, S. Courty, B. K. Gibson, L. Michel-Dansac, and F. Calura, Chemodynamics of a simulated disc galaxy: initial mass functions and Type Ia supernova progenitors, *MNRAS*. **444**, 3845–3862, (2014).
- [190] K. Bekki, Simulating galaxy evolution with a non-universal stellar initial mass function, *MNRAS*. **436**, 2254–2275, (2013).
- [191] T. A. Gutcke and V. Springel, Simulating a metallicity-dependent initial mass function: Consequences for feedback and chemical abundances, *ArXiv e-prints*. (2017).
- [192] C. Barber, R. A. Crain, and J. Schaye, Calibrated, cosmological hydrodynamical simulations with variable IMFs I: Method and effect on global galaxy scaling relations, *ArXiv e-prints*. (2018).
- [193] V. Biffi, F. Mernier, and P. Medvedev, Enrichment of the Hot Intracluster Medium: Numerical Simulations, *Space Sci. Rev.* 214(8):123 (Dec., 2018). doi: 10.1007/s11214-018-0557-7.
- [194] S. J. Smartt, Progenitors of Core-Collapse Supernovae, *ARA&A*. **47**, 63–106 (Sept., 2009). doi: 10.1146/annurev-astro-082708-101737.
- [195] W. Hillebrandt and J. C. Niemeyer, Type IA Supernova Explosion Models, *ARA&A*. **38**, 191–230, (2000). doi: 10.1146/annurev.astro.38.1.191.
- [196] F. Herwig, Evolution of Asymptotic Giant Branch Stars, *ARA&A*. **43**, 435–479 (Sept., 2005). doi: 10.1146/annurev.astro.43.072103.150600.
- [197] P. Padovani and F. Matteucci, Stellar Mass Loss in Elliptical Galaxies and the Fueling of Active Galactic Nuclei, *ApJ*. **416**, 26 (Oct., 1993). doi: 10.1086/173212.
- [198] A. Maeder and G. Meynet, Grids of evolutionary models from 0.85 to 120 solar masses - Observational tests and the mass limits, *A&A*. **210**, 155–173 (Feb., 1989).

- [199] C. Chiappini, F. Matteucci, and R. Gratton, The Chemical Evolution of the Galaxy: The Two-Infall Model, *ApJ*. **477**, 765–780 (Mar., 1997). doi: 10.1086/303726.
- [200] L. Greggio and A. Renzini, The binary model for type I supernovae - Theoretical rates, *A&A*. **118**, 217–222, (1983).
- [201] F.-K. Thielemann, D. Argast, F. Brachwitz, W. R. Hix, P. Höflich, M. Liebendörfer, G. Martinez-Pinedo, A. Mezzacappa, K. Nomoto, and I. Panov. Supernova Nucleosynthesis and Galactic Evolution. In eds. W. Hillebrandt and B. Leibundgut, *From Twilight to Highlight: The Physics of Supernovae*, p. 331, (2003).
- [202] A. I. Karakas, Updated stellar yields from asymptotic giant branch models, *MNRAS*. **403**, 1413–1425 (Apr., 2010).
- [203] C. L. Doherty, P. Gil-Pons, H. H. B. Lau, J. C. Lattanzio, and L. Siess, Super and massive AGB stars - II. Nucleosynthesis and yields -  $Z = 0.02, 0.008$  and  $0.004$ , *MNRAS*. **437**, 195–214, (2014).
- [204] C. L. Doherty, P. Gil-Pons, H. H. B. Lau, J. C. Lattanzio, L. Siess, and S. W. Campbell, Super and massive AGB stars - III. Nucleosynthesis in metal-poor and very metal-poor stars -  $Z = 0.001$  and  $0.0001$ , *MNRAS*. **441**, 582–598, (2014).
- [205] S. E. Woosley and T. A. Weaver, The Evolution and Explosion of Massive Stars. II. Explosive Hydrodynamics and Nucleosynthesis, *ApJS*. **101**, 181–235 (Nov., 1995).
- [206] K. Nomoto, C. Kobayashi, and N. Tominaga, Nucleosynthesis in Stars and the Chemical Enrichment of Galaxies, *ARA&A*. **51**, 457–509, (2013).
- [207] D. Romano, A. I. Karakas, M. Tosi, and F. Matteucci, Quantifying the uncertainties of chemical evolution studies. II. Stellar yields, *A&A*. 522:A32, (2010).
- [208] D. Romano, F. Matteucci, Z.-Y. Zhang, P. P. Papadopoulos, and R. J. Ivison, The evolution of CNO isotopes: a new window on cosmic star formation history and the stellar IMF in the age of ALMA, *MNRAS*. **470**, 401–415, (2017).
- [209] L. Greggio, The rates of type Ia supernovae. I. Analytical formulations, *A&A*. **441**, 1055–1078 (Oct., 2005). doi: 10.1051/0004-6361:20052926.
- [210] F. Matteucci, *The Chemical Evolution of the Galaxy*. Oct. 2003.
- [211] M. Valentini, A. Bressan, S. Borgani, G. Murante, L. Girardi, and L. Tornatore, Colour-magnitude diagram in simulations of galaxy formation, *MNRAS*. **480**(1), 722–741 (Oct., 2018). doi: 10.1093/mnras/sty1896.
- [212] R. J. J. Grand, J. Helly, A. Fattahi, M. Cautun, S. Cole, A. P. Cooper, A. J. Deason, C. Frenk, F. A. Gómez, J. A. S. Hunt, F. Marinacci, R. Pakmor, C. M. Simpson, V. Springel, and D. Xu, Aurigaia: mock Gaia DR2 stellar catalogues from the AURIGA cosmological simulations, *MNRAS*. **481**(2), 1726–1743 (Dec., 2018). doi: 10.1093/mnras/sty2403.
- [213] L. Mayer, F. Governato, and T. Kaufmann, The formation of disk galaxies in computer simulations, *Advanced Science Letters*. **1**, 7–27 (June, 2008). doi: 10.48550/arXiv.0801.3845.
- [214] T. Naab and J. P. Ostriker, Theoretical Challenges in Galaxy Formation, *ARA&A*. **55**(1), 59–109 (Aug., 2017). doi: 10.1146/annurev-astro-081913-040019.
- [215] R. A. Crain and F. van de Voort, Hydrodynamical Simulations of the Galaxy Population: Enduring Successes and Outstanding Challenges, *ARA&A*. **61**, 473–515 (Aug., 2023). doi: 10.1146/annurev-astro-041923-043618.
- [216] C. Dalla Vecchia and J. Schaye, Simulating galactic outflows with thermal supernova feedback, *MNRAS*. **426**(1), 140–158 (Oct., 2012). doi: 10.1111/j.1365-2966.2012.21704.x.
- [217] C. Dalla Vecchia and J. Schaye, Simulating galactic outflows with kinetic supernova feedback, *MNRAS*. **387**(4), 1431–1444 (July, 2008). doi: 10.1111/j.1365-2966.2008.13322.x.

- [218] J. P. E. Gerritsen and V. Icke, Star formation in N-body simulations. I. The impact of the stellar ultraviolet radiation on star formation., *A&A*. **325**, 972–986, (1997).
- [219] G. Stinson, A. Seth, N. Katz, J. Wadsley, F. Governato, and T. Quinn, Star formation and feedback in smoothed particle hydrodynamic simulations - I. Isolated galaxies, *MNRAS*. **373**, 1074–1090, (2006).
- [220] C. Clarke and B. Carswell, *Principles of Astrophysical Fluid Dynamics*. 2007.
- [221] R. J. Thacker and H. M. P. Couchman, Implementing Feedback in Simulations of Galaxy Formation: A Survey of Methods, *ApJ*. **545**, 728–752, (2000).
- [222] F. Governato, B. Willman, L. Mayer, A. Brooks, G. Stinson, O. Valenzuela, J. Wadsley, and T. Quinn, Forming disc galaxies in  $\Lambda$ CDM simulations, *MNRAS*. **374**, 1479–1494, (2007).
- [223] K. M. Fierlinger, A. Burkert, E. Ntormousi, P. Fierlinger, M. Schartmann, A. Balone, M. G. H. Krause, and R. Diehl, Stellar feedback efficiencies: supernovae versus stellar winds, *MNRAS*. **456**(1), 710–730 (Feb., 2016). doi: 10.1093/mnras/stv2699.
- [224] Y. A. Fichtner, L. Grassitelli, E. Romano-Díaz, and C. Porciani, Mechanical feedback from stellar winds with an application to galaxy formation at high redshift, *MNRAS*. **512**(3), 4573–4592 (May, 2022). doi: 10.1093/mnras/stac785.
- [225] A. Obreja, A. V. Macciò, B. Moster, S. M. Udrescu, T. Buck, R. Kannan, A. A. Dutton, and M. Blank, Local photoionization feedback effects on galaxies, *MNRAS*. **490**(2), 1518–1538 (Dec., 2019). doi: 10.1093/mnras/stz2639.
- [226] R. A. Crain, J. Schaye, R. G. Bower, M. Furlong, M. Schaller, T. Theuns, C. Dalla Vecchia, C. S. Frenk, I. G. McCarthy, J. C. Helly, A. Jenkins, Y. M. Rosas-Guevara, S. D. M. White, and J. W. Trayford, The EAGLE simulations of galaxy formation: calibration of subgrid physics and model variations, *MNRAS*. **450**, 1937–1961 (June, 2015). doi: 10.1093/mnras/stv725.
- [227] U. Maio, B. Ciardi, K. Dolag, L. Tornatore, and S. Khochfar, The transition from population III to population II-I star formation, *MNRAS*. **407**(2), 1003–1015 (Sept., 2010). doi: 10.1111/j.1365-2966.2010.17003.x.
- [228] U. Maio, M. Petkova, G. De Lucia, and S. Borgani, Radiative feedback and cosmic molecular gas: the role of different radiative sources, *MNRAS*. **460**(4), 3733–3752 (Aug., 2016). doi: 10.1093/mnras/stw1196.
- [229] V. Bromm and R. B. Larson, The First Stars, *ARA&A*. **42**(1), 79–118 (Sept., 2004). doi: 10.1146/annurev.astro.42.053102.134034.
- [230] B. Ciardi and A. Ferrara, The First Cosmic Structures and Their Effects, *Space Sci. Rev.* **116**(3-4), 625–705 (Feb., 2005). doi: 10.1007/s11214-005-3592-0.
- [231] J. Magorrian, S. Tremaine, D. Richstone, R. Bender, G. Bower, A. Dressler, S. M. Faber, K. Gebhardt, R. Green, C. Grillmair, J. Kormendy, and T. Lauer, The Demography of Massive Dark Objects in Galaxy Centers, *AJ*. **115**, 2285–2305 (June, 1998). doi: 10.1086/300353.
- [232] L. Ferrarese and D. Merritt, A Fundamental Relation between Supermassive Black Holes and Their Host Galaxies, *ApJ*. **539**, L9–L12 (Aug., 2000). doi: 10.1086/312838.
- [233] K. Gebhardt, R. Bender, G. Bower, A. Dressler, S. M. Faber, A. V. Filippenko, R. Green, C. Grillmair, L. C. Ho, J. Kormendy, T. R. Lauer, J. Magorrian, J. Pinkney, D. Richstone, and S. Tremaine, A Relationship between Nuclear Black Hole Mass and Galaxy Velocity Dispersion, *ApJ*. **539**, L13–L16 (Aug., 2000). doi: 10.1086/312840.
- [234] D. Merritt and L. Ferrarese, The  $M_{\bullet}$ - $\sigma$  Relation for Supermassive Black Holes, *ApJ*. **547**, 140–145 (Jan., 2001). doi: 10.1086/318372.
- [235] S. Tremaine, K. Gebhardt, R. Bender, G. Bower, A. Dressler, S. M. Faber, A. V. Filippenko, R. Green, C. Grillmair, L. C. Ho, J. Kormendy, T. R. Lauer, J. Magorrian,

- J. Pinkney, and D. Richstone, The Slope of the Black Hole Mass versus Velocity Dispersion Correlation, *ApJ*. **574**, 740–753 (Aug., 2002). doi: 10.1086/341002.
- [236] A. Marconi and L. K. Hunt, The Relation between Black Hole Mass, Bulge Mass, and Near-Infrared Luminosity, *ApJ*. **589**, L21–L24 (May, 2003). doi: 10.1086/375804.
- [237] N. Häring and H.-W. Rix, On the Black Hole Mass-Bulge Mass Relation, *ApJ*. **604**, L89–L92 (Apr., 2004). doi: 10.1086/383567.
- [238] J. Kormendy and L. C. Ho, Coevolution (Or Not) of Supermassive Black Holes and Host Galaxies, *Annual Review of Astronomy and Astrophysics*. **51**, 511–653 (Aug., 2013). doi: 10.1146/annurev-astro-082708-101811.
- [239] M. Gaspari, D. Eckert, S. Ettori, P. Tozzi, L. Bassini, E. Rasia, F. Brighenti, M. Sun, S. Borgani, S. D. Johnson, G. Tremblay, J. Stone, P. Temi, H.-Y. K. Yang, F. Tombesi, and M. Cappi, The X-ray Halo Scaling Relations of Supermassive Black Holes, *arXiv e-prints* (Apr. 2019).
- [240] M. Gitti, F. Brighenti, and B. R. McNamara, Evidence for AGN Feedback in Galaxy Clusters and Groups, *Advances in Astronomy*. 2012:950641 (Jan., 2012). doi: 10.1155/2012/950641.
- [241] V. Springel, T. Di Matteo, and L. Hernquist, Modelling feedback from stars and black holes in galaxy mergers, *MNRAS*. **361**, 776–794 (Aug., 2005). doi: 10.1111/j.1365-2966.2005.09238.x.
- [242] T. Di Matteo, V. Springel, and L. Hernquist, Energy input from quasars regulates the growth and activity of black holes and their host galaxies, *Nature*. **433**, 604–607 (Feb., 2005). doi: 10.1038/nature03335.
- [243] M. R. Bate, I. A. Bonnell, and N. M. Price, Modelling accretion in protobinary systems, *MNRAS*. **277**(2), 362–376 (Nov., 1995). doi: 10.1093/mnras/277.2.362.
- [244] V. Bromm and A. Loeb, Formation of the First Supermassive Black Holes, *ApJ*. **596**, 34–46 (Oct., 2003). doi: 10.1086/377529.
- [245] M. C. Begelman, M. Volonteri, and M. J. Rees, Formation of supermassive black holes by direct collapse in pre-galactic haloes, *MNRAS*. **370**, 289–298 (July, 2006). doi: 10.1111/j.1365-2966.2006.10467.x.
- [246] L. Mayer, S. Kazantzidis, A. Escala, and S. Callegari, Direct formation of supermassive black holes via multi-scale gas inflows in galaxy mergers, *Nature*. **466**, 1082–1084 (Aug., 2010). doi: 10.1038/nature09294.
- [247] M. Volonteri and J. Bellovary, Black holes in the early Universe, *Reports on Progress in Physics*. 75(12):124901 (Dec., 2012). doi: 10.1088/0034-4885/75/12/124901.
- [248] U. Maio, S. Borgani, B. Ciardi, and M. Petkova, The seeds of supermassive black holes and the role of local radiation and metal spreading, *arXiv e-prints* (Nov. 2018).
- [249] T. Di Matteo, D. Angles-Alcazar, and F. Shankar, Massive black holes in galactic nuclei: Theory and Simulations, *arXiv e-prints*. art. arXiv:2304.11541 (Apr., 2023). doi: 10.48550/arXiv.2304.11541.
- [250] M. Davis, G. Efstathiou, C. S. Frenk, and S. D. M. White, The evolution of large-scale structure in a universe dominated by cold dark matter, *ApJ*. **292**, 371–394 (May, 1985). doi: 10.1086/163168.
- [251] P. Taylor and C. Kobayashi, Seeding black holes in cosmological simulations, *MNRAS*. **442**(3), 2751–2767 (Aug., 2014). doi: 10.1093/mnras/stu983.
- [252] M. Habouzit, M. Volonteri, and Y. Dubois, Blossoms from black hole seeds: properties and early growth regulated by supernova feedback, *MNRAS*. **468**(4), 3935–3948 (July, 2017). doi: 10.1093/mnras/stx666.
- [253] E. X. Wang, P. Taylor, C. Federrath, and C. Kobayashi, The impact of black hole seeding in cosmological simulations, *MNRAS*. **483**(4), 4640–4648 (Mar., 2019). doi: 10.1093/mnras/sty3491.

- [254] T. Di Matteo, J. Colberg, V. Springel, L. Hernquist, and D. Sijacki, Direct Cosmological Simulations of the Growth of Black Holes and Galaxies, *ApJ*. **676**(1), 33–53 (Mar., 2008). doi: 10.1086/524921.
- [255] J. Wurster and R. J. Thacker, A comparative study of AGN feedback algorithms, *MNRAS*. **431**, 2513–2534 (May, 2013). doi: 10.1093/mnras/stt346.
- [256] J. Debuhr, E. Quataert, and C.-P. Ma, The growth of massive black holes in galaxy merger simulations with feedback by radiation pressure, *MNRAS*. **412**(2), 1341–1360 (Apr., 2011). doi: 10.1111/j.1365-2966.2010.17992.x.
- [257] M. Tremmel, F. Governato, M. Volonteri, and T. R. Quinn, Off the beaten path: a new approach to realistically model the orbital decay of supermassive black holes in galaxy formation simulations, *MNRAS*. **451**(2), 1868–1874 (Aug., 2015). doi: 10.1093/mnras/stv1060.
- [258] N. Chen, Y. Ni, A. M. Holgado, T. Di Matteo, M. Tremmel, C. DeGraf, S. Bird, R. Croft, and Y. Feng, Massive black hole mergers with orbital information: predictions from the ASTRID simulation, *MNRAS*. **514**(2), 2220–2238 (Aug., 2022). doi: 10.1093/mnras/stac1432.
- [259] A. Damiano, M. Valentini, S. Borgani, L. Tornatore, G. Murante, A. Ragagnin, C. Ragone-Figueroa, and K. Dolag, Dynamical friction and evolution of black holes in cosmological simulations: a new implementation in OpenGadget3, *arXiv e-prints*. art. arXiv:2403.12600 (Mar., 2024). doi: 10.48550/arXiv.2403.12600.
- [260] A. Genina, V. Springel, and A. Rantala, A calibrated model for N-body dynamical friction acting on supermassive black holes, *arXiv e-prints*. art. arXiv:2405.08870 (May, 2024). doi: 10.48550/arXiv.2405.08870.
- [261] F. Hoyle and R. A. Lyttleton, The effect of interstellar matter on climatic variation, *Proceedings of the Cambridge Philosophical Society*. **35**, 405, (1939). doi: 10.1017/S0305004100021150.
- [262] H. Bondi, On spherically symmetrical accretion, *MNRAS*. **112**, 195, (1952).
- [263] H. Bondi and F. Hoyle, On the mechanism of accretion by stars, *MNRAS*. **104**, 273, (1944).
- [264] J. A. Regan, T. P. Downes, M. Volonteri, R. Beckmann, A. Lupi, M. Trebitsch, and Y. Dubois, Super-Eddington accretion and feedback from the first massive seed black holes, *MNRAS*. **486**(3), 3892–3906 (July, 2019). doi: 10.1093/mnras/stz1045.
- [265] E. Choi, J. P. Ostriker, T. Naab, and P. H. Johansson, Radiative and Momentum-based Mechanical Active Galactic Nucleus Feedback in a Three-dimensional Galaxy Evolution Code, *ApJ*. 754:125 (Aug., 2012). doi: 10.1088/0004-637X/754/2/125.
- [266] E. Choi, T. Naab, J. P. Ostriker, P. H. Johansson, and B. P. Moster, Consequences of mechanical and radiative feedback from black holes in disc galaxy mergers, *MNRAS*. **442**, 440–453 (July, 2014). doi: 10.1093/mnras/stu874.
- [267] C. M. Booth and J. Schaye, Cosmological simulations of the growth of supermassive black holes and feedback from active galactic nuclei: method and tests, *MNRAS*. **398**, 53–74 (Sept., 2009). doi: 10.1111/j.1365-2966.2009.15043.x.
- [268] M. Vogelsberger, S. Genel, D. Sijacki, P. Torrey, V. Springel, and L. Hernquist, A model for cosmological simulations of galaxy formation physics, *MNRAS*. **436**, 3031–3067 (Dec., 2013). doi: 10.1093/mnras/stt1789.
- [269] Y. M. Rosas-Guevara, R. G. Bower, J. Schaye, M. Furlong, C. S. Frenk, C. M. Booth, R. Crain, C. Dalla Vecchia, M. Schaller, and T. Theuns, The impact of angular momentum on black hole accretion rates in simulations of galaxy formation, *ArXiv e-prints* (Dec. 2013).
- [270] M. Valentini, G. Murante, S. Borgani, G. L. Granato, P. Monaco, F. Brighenti, L. Tornatore, A. Bressan, and A. Lapi, Impact of AGN feedback on galaxies and

- their multiphase ISM across cosmic time, *MNRAS*. **491**(2), 2779–2807 (Jan., 2020). doi: 10.1093/mnras/stz3131.
- [271] M. Gaspari, M. Ruszkowski, and S. P. Oh, Chaotic cold accretion on to black holes, *MNRAS*. **432**, 3401–3422 (July, 2013). doi: 10.1093/mnras/stt692.
- [272] L. K. Steinborn, K. Dolag, M. Hirschmann, M. A. Prieto, and R.-S. Remus, A refined sub-grid model for black hole accretion and AGN feedback in large cosmological simulations, *MNRAS*. **448**, 1504–1525 (Apr., 2015). doi: 10.1093/mnras/stv072.
- [273] E. Churazov, S. Sazonov, R. Sunyaev, W. Forman, C. Jones, and H. Böhringer, Supermassive black holes in elliptical galaxies: switching from very bright to very dim, *MNRAS*. **363**(1), L91–L95 (Oct., 2005). doi: 10.1111/j.1745-3933.2005.00093.x.
- [274] V. Biffi, K. Dolag, and A. Merloni, AGN contamination of galaxy-cluster thermal X-ray emission: predictions for eRosita from cosmological simulations, *MNRAS*. **481**(2), 2213–2227 (Dec., 2018). doi: 10.1093/mnras/sty2436.
- [275] M. Habouzit, R. S. Somerville, Y. Li, S. Genel, J. Aird, D. Anglés-Alcázar, R. Davé, I. Y. Georgiev, S. McAlpine, Y. Rosas-Guevara, Y. Dubois, D. Nelson, E. Banados, L. Hernquist, S. Peirani, and M. Vogelsberger, Supermassive black holes in cosmological simulations - II: the AGN population and predictions for upcoming X-ray missions, *MNRAS*. **509**(2), 3015–3042 (Jan., 2022). doi: 10.1093/mnras/stab3147.
- [276] H. R. Russell, B. R. McNamara, A. C. Edge, M. T. Hogan, R. A. Main, and A. N. Vantyghem, Radiative efficiency, variability and Bondi accretion on to massive black holes: the transition from radio AGN to quasars in brightest cluster galaxies, *MNRAS*. **432**, 530–553 (June, 2013). doi: 10.1093/mnras/stt490.
- [277] M. Mezcua and M. A. Prieto, Evidence of Parsec-scale Jets in Low-luminosity Active Galactic Nuclei, *ApJ*. **787**:62 (May, 2014). doi: 10.1088/0004-637X/787/1/62.
- [278] A. C. Fabian, Observational Evidence of Active Galactic Nuclei Feedback, *ARA&A*. **50**, 455–489 (Sept., 2012). doi: 10.1146/annurev-astro-081811-125521.
- [279] A. Merloni and S. Heinz, A synthesis model for AGN evolution: supermassive black holes growth and feedback modes, *MNRAS*. **388**(3), 1011–1030 (Aug., 2008). doi: 10.1111/j.1365-2966.2008.13472.x.
- [280] F. Yuan and R. Narayan, Hot Accretion Flows Around Black Holes, *ARA&A*. **52**, 529–588 (Aug., 2014). doi: 10.1146/annurev-astro-082812-141003.
- [281] S. W. Davis and A. Laor, The Radiative Efficiency of Accretion Flows in Individual Active Galactic Nuclei, *ApJ*. **728**:98 (Feb., 2011). doi: 10.1088/0004-637X/728/2/98.
- [282] D. Chelouche, The Case for Standard Irradiated Accretion Disks in Active Galactic Nuclei, *ApJ*. **772**:9 (July, 2013). doi: 10.1088/0004-637X/772/1/9.
- [283] T. M. Heckman and P. N. Best, The Coevolution of Galaxies and Supermassive Black Holes: Insights from Surveys of the Contemporary Universe, *ARA&A*. **52**, 589–660 (Aug., 2014). doi: 10.1146/annurev-astro-081913-035722.
- [284] R. P. Fender, T. M. Belloni, and E. Gallo, Towards a unified model for black hole X-ray binary jets, *MNRAS*. **355**(4), 1105–1118 (Dec., 2004). doi: 10.1111/j.1365-2966.2004.08384.x.
- [285] A. Tchekhovskoy, J. C. McKinney, and R. Narayan. General Relativistic Modeling of Magnetized Jets from Accreting Black Holes. In *Journal of Physics Conference Series*, vol. 372, *Journal of Physics Conference Series*, p. 012040. IOP (July, 2012). doi: 10.1088/1742-6596/372/1/012040.
- [286] A. Sadowski and R. Narayan, Three-dimensional simulations of supercritical black hole accretion discs - luminosities, photon trapping and variability, *MNRAS*. **456**(4), 3929–3947 (Mar., 2016). doi: 10.1093/mnras/stv2941.
- [287] C. M. Harrison and C. Ramos Almeida, Observational Tests of Active Galactic Nuclei Feedback: An Overview of Approaches and Interpretation, *Galaxies*. **12**(2):

- 17 (Apr., 2024). doi: 10.3390/galaxies12020017.
- [288] N. I. Shakura and R. A. Sunyaev, Black holes in binary systems. Observational appearance., *A&A*. **24**, 337–355, (1973).
- [289] I. D. Novikov and K. S. Thorne. Astrophysics of black holes. In *Black Holes (Les Astres Occlus)*, pp. 343–450 (Jan., 1973).
- [290] Q. Yu and S. Tremaine, Observational constraints on growth of massive black holes, *MNRAS*. **335**(4), 965–976 (Oct., 2002). doi: 10.1046/j.1365-8711.2002.05532.x.
- [291] L. Sala, M. Valentini, V. Biffi, and K. Dolag, Supermassive black hole spin evolution in cosmological simulations with OPENGADGET3, *A&A*. 685:A92 (May, 2024). doi: 10.1051/0004-6361/202348925.
- [292] J. P. Ostriker, E. Choi, L. Ciotti, G. S. Novak, and D. Proga, Momentum Driving: Which Physical Processes Dominate Active Galactic Nucleus Feedback?, *ApJ*. **722** (1), 642–652 (Oct., 2010). doi: 10.1088/0004-637X/722/1/642.
- [293] Y. Dubois, C. Pichon, M. Haehnelt, T. Kimm, A. Slyz, J. Devriendt, and D. Pogosyan, Feeding compact bulges and supermassive black holes with low angular momentum cosmic gas at high redshift, *MNRAS*. **423**(4), 3616–3630 (July, 2012). doi: 10.1111/j.1365-2966.2012.21160.x.
- [294] T. Costa, D. Sijacki, M. Trenti, and M. G. Haehnelt, The environment of bright QSOs at  $z \sim 6$ : star-forming galaxies and X-ray emission, *MNRAS*. **439**(2), 2146–2174 (Apr., 2014). doi: 10.1093/mnras/stu101.
- [295] A. Lupi, M. Volonteri, R. Decarli, S. Bovino, J. Silk, and J. Bergeron, High-redshift quasars and their host galaxies - I. Kinematical and dynamical properties and their tracers, *MNRAS*. **488**(3), 4004–4022 (Sept., 2019). doi: 10.1093/mnras/stz1959.
- [296] M. Trebitsch, M. Volonteri, and Y. Dubois, Modelling a bright  $z = 6$  galaxy at the faint end of the AGN luminosity function, *MNRAS*. **494**(3), 3453–3463 (Apr., 2020). doi: 10.1093/mnras/staa1012.
- [297] P. N. Best and T. M. Heckman, On the fundamental dichotomy in the local radio-AGN population: accretion, evolution and host galaxy properties, *MNRAS*. **421**(2), 1569–1582 (Apr., 2012). doi: 10.1111/j.1365-2966.2012.20414.x.
- [298] D. Sijacki, V. Springel, T. Di Matteo, and L. Hernquist, A unified model for AGN feedback in cosmological simulations of structure formation, *MNRAS*. **380**, 877–900 (Sept., 2007). doi: 10.1111/j.1365-2966.2007.12153.x.
- [299] D. Fabjan, S. Borgani, L. Tornatore, A. Saro, G. Murante, and K. Dolag, Simulating the effect of active galactic nuclei feedback on the metal enrichment of galaxy clusters, *MNRAS*. **401**, 1670–1690 (Jan., 2010). doi: 10.1111/j.1365-2966.2009.15794.x.
- [300] Y. Dubois, J. Devriendt, A. Slyz, and R. Teyssier, Self-regulated growth of supermassive black holes by a dual jet-heating active galactic nucleus feedback mechanism: methods, tests and implications for cosmological simulations, *MNRAS*. **420**(3), 2662–2683 (Mar., 2012). doi: 10.1111/j.1365-2966.2011.20236.x.
- [301] R. Weinberger, K. Ehlert, C. Pfrommer, R. Pakmor, and V. Springel, Simulating the interaction of jets with the intracluster medium, *MNRAS*. **470**(4), 4530–4546 (Oct., 2017). doi: 10.1093/mnras/stx1409.
- [302] D. Sijacki, V. Springel, T. di Matteo, and L. Hernquist, A unified model for AGN feedback in cosmological simulations of structure formation, *MNRAS*. **380**, 877–900 (Sept., 2007). doi: 10.1111/j.1365-2966.2007.12153.x.
- [303] D. Anglés-Alcázar, R. Davé, C.-A. Faucher-Giguère, F. Özel, and P. F. Hopkins, Gravitational torque-driven black hole growth and feedback in cosmological simulations, *MNRAS*. **464**(3), 2840–2853 (Jan., 2017). doi: 10.1093/mnras/stw2565.
- [304] L. Scharré, D. Sorini, and R. Davé, The Effects of Stellar and AGN Feedback on the Cosmic Star Formation History in the Simba Simulations, *arXiv e-prints*. art.

- arXiv:2404.07252 (Apr., 2024). doi: 10.48550/arXiv.2404.07252.
- [305] Y. Dubois, M. Volonteri, J. Silk, J. Devriendt, and A. Slyz, Black hole evolution - II. Spinning black holes in a supernova-driven turbulent interstellar medium, *MNRAS*. **440**(3), 2333–2346 (May, 2014). doi: 10.1093/mnras/stu425.
- [306] D. Anglés-Alcázar, C.-A. Faucher-Giguère, E. Quataert, P. F. Hopkins, R. Feldmann, P. Torrey, A. Wetzel, and D. Kereš, Black holes on FIRE: stellar feedback limits early feeding of galactic nuclei, *MNRAS*. **472**(1), L109–L114 (Nov., 2017). doi: 10.1093/mnrasl/slx161.
- [307] M. Tremmel, T. R. Quinn, A. Ricarte, A. Babul, U. Chadayammuri, P. Natarajan, D. Nagai, A. Pontzen, and M. Volonteri, Introducing ROMULUSC: a cosmological simulation of a galaxy cluster with an unprecedented resolution, *MNRAS*. **483**(3), 3336–3362 (Mar., 2019). doi: 10.1093/mnras/sty3336.
- [308] M. Blank, A. V. Macciò, A. A. Dutton, and A. Obreja, NIHAO - XXII. Introducing black hole formation, accretion, and feedback into the NIHAO simulation suite, *MNRAS*. **487**(4), 5476–5489 (Aug., 2019). doi: 10.1093/mnras/stz1688.
- [309] Y. Ni, T. Di Matteo, S. Bird, R. Croft, Y. Feng, N. Chen, M. Tremmel, C. DeGraf, and Y. Li, The ASTRID simulation: the evolution of supermassive black holes, *MNRAS*. **513**(1), 670–692 (June, 2022). doi: 10.1093/mnras/stac351.
- [310] I. K. Baldry, S. P. Driver, J. Loveday, E. N. Taylor, L. S. Kelvin, J. Liske, P. Norberg, A. S. G. Robotham, S. Brough, A. M. Hopkins, S. P. Bamford, J. A. Peacock, J. Bland-Hawthorn, C. J. Conselice, S. M. Croom, D. H. Jones, H. R. Parkinson, C. C. Popescu, M. Prescott, R. G. Sharp, and R. J. Tuffs, Galaxy And Mass Assembly (GAMA): the galaxy stellar mass function at  $z \leq 0.06$ , *MNRAS*. **421**(1), 621–634 (Mar., 2012). doi: 10.1111/j.1365-2966.2012.20340.x.
- [311] Y. E. Bahar, E. Bulbul, V. Ghirardini, J. S. Sanders, X. Zhang, A. Liu, N. Clerc, E. Artis, F. Balzer, V. Biffi, S. Bose, J. Comparat, K. Dolag, C. Garrel, B. Hadzhiyska, C. Hernández-Aguayo, L. Hernquist, M. Kluge, S. Krippendorff, A. Merloni, K. Nandra, R. Pakmor, P. Popesso, M. Ramos-Ceja, R. Seppi, V. Springel, J. Weller, and S. Zelmer, The SRG/eROSITA All-Sky Survey: Constraints on AGN Feedback in Galaxy Groups, *arXiv e-prints*. art. arXiv:2401.17276 (Jan., 2024). doi: 10.48550/arXiv.2401.17276.
- [312] M. Habouzit, Y. Li, R. S. Somerville, S. Genel, A. Pillepich, M. Volonteri, R. Davé, Y. Rosas-Guevara, S. McAlpine, S. Peirani, L. Hernquist, D. Anglés-Alcázar, A. Reines, R. Bower, Y. Dubois, D. Nelson, C. Pichon, and M. Vogelsberger, Supermassive black holes in cosmological simulations I:  $M_{BH} - M_*$  relation and black hole mass function, *MNRAS*. **503**(2), 1940–1975 (May, 2021). doi: 10.1093/mnras/stab496.
- [313] F. Villaescusa-Navarro, D. Anglés-Alcázar, S. Genel, D. N. Spergel, R. S. Somerville, R. Dave, A. Pillepich, L. Hernquist, D. Nelson, P. Torrey, D. Narayanan, Y. Li, O. Philcox, V. La Torre, A. Maria Delgado, S. Ho, S. Hassan, B. Burkhart, D. Wadekar, N. Battaglia, G. Contardo, and G. L. Bryan, The CAMELS Project: Cosmology and Astrophysics with Machine-learning Simulations, *ApJ*. **915**(1):71 (July, 2021). doi: 10.3847/1538-4357/abf7ba.
- [314] M. Hirschmann, G. De Lucia, and F. Fontanot, Galaxy assembly, stellar feedback and metal enrichment: the view from the GAEA model, *MNRAS*. **461**(2), 1760–1785 (Sept., 2016). doi: 10.1093/mnras/stw1318.
- [315] V. Biffi, K. Dolag, H. Böhringer, and G. Lemson, Observing simulated galaxy clusters with PHOX: a novel X-ray photon simulator, *MNRAS*. **420**(4), 3545–3556 (Mar., 2012). doi: 10.1111/j.1365-2966.2011.20278.x.

- [316] M. Curtis and D. Sijacki, Resolving flows around black holes: numerical technique and applications, *MNRAS*. **454**(4), 3445–3463 (Dec., 2015). doi: 10.1093/mnras/stv2246.
- [317] S. Koudmani, D. Sijacki, M. A. Bourne, and M. C. Smith, Fast and energetic AGN-driven outflows in simulated dwarf galaxies, *MNRAS*. **484**(2), 2047–2066 (Apr., 2019). doi: 10.1093/mnras/stz097.
- [318] D. Anglés-Alcázar, E. Quataert, P. F. Hopkins, R. S. Somerville, C. C. Hayward, C.-A. Faucher-Giguère, G. L. Bryan, D. Kereš, L. Hernquist, and J. M. Stone, Cosmological Simulations of Quasar Fueling to Subparsec Scales Using Lagrangian Hyper-refinement, *ApJ*. **917**(2):53 (Aug., 2021). doi: 10.3847/1538-4357/ac09e8.
- [319] F. van de Voort, V. Springel, N. Mandelker, F. C. van den Bosch, and R. Pakmor, Cosmological simulations of the circumgalactic medium with 1 kpc resolution: enhanced H I column densities, *MNRAS*. **482**(1), L85–L89 (Jan., 2019). doi: 10.1093/mnras/sly190.
- [320] D. Fiacconi, D. Sijacki, and J. E. Pringle, Galactic nuclei evolution with spinning black holes: method and implementation, *MNRAS*. **477**(3), 3807–3835 (July, 2018). doi: 10.1093/mnras/sty893.
- [321] S. Bustamante and V. Springel, Spin evolution and feedback of supermassive black holes in cosmological simulations, *MNRAS*. **490**(3), 4133–4153 (Dec., 2019). doi: 10.1093/mnras/stz2836.
- [322] F. Huško, C. G. Lacey, J. Schaye, M. Schaller, and F. S. J. Nobels, Spin-driven jet feedback in idealized simulations of galaxy groups and clusters, *MNRAS*. **516**(3), 3750–3772 (Nov., 2022). doi: 10.1093/mnras/stac2278.
- [323] M. A. Bourne and D. Sijacki, AGN jet feedback on a moving mesh: cocoon inflation, gas flows and turbulence, *MNRAS*. **472**(4), 4707–4735 (Dec., 2017). doi: 10.1093/mnras/stx2269.
- [324] S. Cielo, A. Babul, V. Antonuccio-Delogu, J. Silk, and M. Volonteri, Feedback from reorienting AGN jets. I. Jet-ICM coupling, cavity properties and global energetics, *A&A*. **617**:A58 (Sept., 2018). doi: 10.1051/0004-6361/201832582.
- [325] R. Y. Talbot, D. Sijacki, and M. A. Bourne, Blandford-Znajek jets in galaxy formation simulations: exploring the diversity of outflows produced by spin-driven AGN jets in Seyfert galaxies, *MNRAS*. **514**(3), 4535–4559 (Aug., 2022). doi: 10.1093/mnras/stac1566.
- [326] R. Y. Talbot, D. Sijacki, and M. A. Bourne, Simulations of spin-driven AGN jets in gas-rich galaxy mergers, *MNRAS*. **528**(3), 5432–5451 (Mar., 2024). doi: 10.1093/mnras/stae392.